USING DRELL-YAN TO PROBE THE UNDERLYING EVENT IN RUN II AT COLLIDER DETECTOR AT FERMILAB (CDF)

By

DEEPAK KAR

A DISSERTATION PRESENTED TO THE GRADUATE SCHOOL
OF THE UNIVERSITY OF FLORIDA IN PARTIAL FULFILLMENT
OF THE REQUIREMENTS FOR THE DEGREE OF
DOCTOR OF PHILOSOPHY

UNIVERSITY OF FLORIDA

2008

To everyone who kept asking when I would be done

ACKNOWLEDGMENTS

This dissertation is the result of my five years of work in the department of physics at the University of Florida. I would like to take this opportunity to acknowledge the direct and indirect contributions of many people on this work.

It is difficult to overstate my gratitude to my Ph.D. supervisor, Prof. Richard D. Field. When I first came here, I had little idea of how exciting experimental particle physics can be, and I leave determined to have a career in the field. He has been a wonderful teacher, a great motivator, and above all a great source of support in everything I did, while allowing me enough freedom. Although as a Ph.D. thesis, this work is necessarily authored by me alone, most of it has benefited from his remarkable insights and tireless effort to understand the physics and explain what is 'goofy'. I have been incredibly fortunate to have had him as my supervisor and I do not know where I would be without him.

He had provided financial support from his research grants, so that I could concentrate full time on research or do the required service work for the CDF collaboration. He also funded my travels to different conferences and schools over these years, and those helped me immensely and gave valuable experience.

I would like to thank Prof. Konstantin Matchev who was available whenever I needed his advice. His insistence that I give as many talks as possible definitely helped me to conquer my fear of public speaking. His QFT course was a great foundation for starting my work in this area.

I would also like to thank the other members of my PhD committee who monitored my work and took effort in reading and providing me with valuable comments on earlier versions of this thesis: Prof Darin Acosta, Prof James Fry and Prof Sanjay Ranka.

I am greatly indebted to Dr. Robert Craig Group, formerly a Ph.D student of Prof. Field, now a research associate at Fermilab. He not only helped me to get started, but

was there at every step. No question was stupid for him and he had a solution to every problem. A big thanks go out to him.

There are many people in CDF collaboration who helped me at different stages of my analysis. The comments and suggestions from the conveners of the QCD group, Dr. Kenichi Hatakeyama and Dr. Sasha Pronko have been extremely beneficial. I also have to appreciate their incredible patience. Dr. Regis Lefevre was the convener when I started this analysis, and he made important comments in early stage. I would also like to thank Dr. Raymond Culbertson, who helped me many a times when I got stuck. Without the generous help of all these and many other people, it would have been very difficult to finish this analysis without actually being at Fermilab.

Once I left my passport in the department, the day before going on a month long India trip. Darlene Latimer and Chris Scanlon came all the way from their home on a Friday night to retrieve it, so that I did not have to miss the trip. As helpful has been all the staff in the department, and that includes Yvonne Dixon and Nathan Williams too. The computer support staff, notably David Hansen, Brent Nelson and Yu Fu worked hard so that we could work on physics uninterrupted.

I must mention my excellent and motivating teachers at Jadavpur University department of physics, my undergraduate and masters institution, specifically Dr. Soumitra Sengupta, Dr. Subhankar Ray and Dr. Narayan Banerjee. I learnt a lot of my physics from them.

I would also like to thank many of my colleagues at the department of Physics for their help with my everything. Whether working on assignments till late night or celebrating all those national championships we won, it has been a wonderfully fun journey. I wish all of you the very best.

Many friends, not all of them physicists, have been a constant source of support. From helping me with my code or to go over a presentation or by just simply being there. I thank them all so very much.

Last, but not the least, nothing would have been possible without my family. They have always put education as a first priority in my life, and raised me to set high goals for myself. No words of gratitude are enough for that, and I would not try.

TABLE OF CONTENTS

page

ACKNOWLEDGMENTS 4

LIST OF TABLES 9

LIST OF FIGURES 10

ABSTRACT 14

CHAPTER

1 INTRODUCTION: THE STANDARD MODEL AND THE QCD 15

1.1 Overview 15
1.2 Standard Model of Particle Physics 15

2 THE EXPERIMENT: TEVATRON 19

2.1 Introduction 19
2.2 The Tevatron 20
2.3 Collider Coordinates 22
2.4 The CDF Detector 24
2.4.1 Overview 24
2.4.2 Tracking Systems 25
2.4.3 Calorimeters 26
2.4.4 Muon Chambers 28
2.4.5 Luminosity Counter 29
2.4.6 Trigger System 31
2.4.7 Run II Upgrade 32

3 COLLIDER PHENOMENOLOGY 34

3.1 Overview of Hadronic Collisions 34
3.2 Typical Collider Event 35
3.3 The Underlying Event 37
3.4 Minimum Bias Collisions and the Underlying Event 39
3.5 Dividing Into Regions 40

4 THE DRELL-YAN PROCESS 43

4.1 Historical Perspective 43
4.2 Cross Section Calculations for the Drell-Yan Process 44
4.3 Experimental Studies with the Drell-Yan 48
4.4 Drell-Yan Process and the Underlying Event 50

5 MONTE CARLO EVENT GENERATORS . . . 52
5.1 Overview . . . 52
5.2 Event Generation . . . 53
5.3 Examples of Event Generators: PYTHIA and HERWIG . . . 54
5.4 Tuning PYTHIA . . . 57
6 ANALYSIS STRATEGY . . . 62
6.1 Introduction: Goal . . . 62
6.2 Data Selection . . . 62
6.3 Event Selection . . . 63
6.4 Electron Selection . . . 63
6.5 Muon Selection . . . 65
6.6 Lepton Pair Formation . . . 68
6.7 Charged Track Selection . . . 70
6.8 Observables . . . 71
7 RESULTS . . . 73
7.1 Earlier Work . . . 73
7.2 Correcting Data Back to Particle Level . . . 73
7.3 Systematic Errors . . . 74
7.4 Drell-Yan Results . . . 76
7.4.1 Underlying Event Observables . . . 76
7.4.2 Comparing Different Regions . . . 79
7.4.3 Comparison with the Leading Jet Underlying Event Results . . . 80
7.4.4 Correlation Between Mean Transverse Momentum and Multiplicity . . . 81
8 SUMMARY AND CONCLUSION . . . 104
8.1 Conclusions . . . 104
8.2 Looking Ahead to the LHC . . . 106
8.3 Final Words . . . 108
APPENDIX
A ALL THE NUMBERS . . . 109
REFERENCES . . . 121
BIOGRAPHICAL SKETCH . . . 127

LIST OF TABLES

Table page

2-1 CDF 3 level trigger . . . 32

4-1 Drell-Yan cross sections . . . 49

5-1 PYTHIA parameters . . . 58

5-2 Parameters for several PYTHIA 6.2 tunes . . . 60

5-3 Multiple parton scattering cross section . . . 60

6-1 Data and Monte-Carlo samples used in this analysis . . . 63

6-2 Electron selection . . . 65

6-3 Muon selection . . . 68

6-4 Mass ranges . . . 69

6-5 Charged track selection . . . 71

6-6 Observables . . . 72

7-1 Systematic uncertainties . . . 76

A-1 Charged multiplicity density, PYTHIA tune AW . . . 109

A-2 Charged multiplicity density, data . . . 110

A-3 Charged transverse momentum sum density, PYTHIA tune AW . . . 111

A-4 Charged transverse momentum sum density, data . . . 112

A-5 TransMAX and MIN, PYTHIA tune AW . . . 113

A-6 TransMax and MIN, data . . . 114

A-7 Charged transverse momentum average, PYTHIA tune AW . . . 115

A-8 Charged transverse momentum average, data . . . 116

A-9 Charged transverse momentum maximum, PYTHIA tune AW . . . 117

A-10 Charged transverse momentum maximum, data . . . 118

A-11 Correlations, PYTHIA tune AW . . . 119

A-12 Correlations, data . . . 120

LIST OF FIGURES

Figure page

1-1 Standard Model of particle physics . . . 17
2-1 Collider modes . . . 20
2-2 Tevatron . . . 21
2-3 Collider coordinates, z-axis and polar angle . . . 23
2-4 Collider coordinates, transverse momentum and psuedorapidity . . . 23
2-5 Collider coordinates, psuedorapidity . . . 24
2-6 Collider Detector at Fermilab . . . 25
2-7 Electromagnetic shower . . . 27
2-8 Particle detection at CDF . . . 29
2-9 Luminosity obtained at CDF . . . 30
2-10 Trigger system at CDF . . . 32
3-1 Hadronic collision cross section . . . 35
3-2 Hadronic collision . . . 35
3-3 Feynman diagrams for hadronic collision . . . 36
3-4 Parton shower . . . 38
3-5 The underlying event . . . 39
3-6 Dividing the central region . . . 41
3-7 Regions for a Z-boson event . . . 41
3-8 Transverse regions . . . 42
4-1 Drell-Yan process . . . 43
4-2 Drell-Yan cross section . . . 44
4-3 Drell-Yan Feynman diagram . . . 45
4-4 Drell-Yan QCD effects . . . 47
4-5 Z-boson recoil with Drell-Yan production . . . 48
4-6 Underlying event in Drell-Yan process . . . 50

4-7 High transverse momentum Drell-Yan process . . . 50
4-8 Drell-Yan event . . . 51
5-1 Event generation . . . 54
5-2 String fragmentation . . . 56
5-3 Run 1 tunes . . . 59
6-1 Pair production . . . 66
6-2 Background for Z-boson production . . . 70
7-1 Detector and particle level . . . 74
7-2 Correcting data Back to particle Level . . . 75
7-3 Systematic error, data uncorrected . . . 76
7-4 Systematic error, data corrected . . . 77
7-5 Drell-Yan transverse region charged multiplicity density . . . 83
7-6 Drell-Yan toward region charged multiplicity density . . . 83
7-7 Drell-Yan away region charged multiplicity density . . . 84
7-8 Drell-Yan transMAX and transMIN regions charged multiplicity density . . . 84
7-9 Drell-Yan transDIF region charged multiplicity density . . . 85
7-10 Drell-Yan transverse region charged transverse momentum sum density . . . 85
7-11 Drell-Yan toward region charged transverse momentum sum density . . . 86
7-12 Drell-Yan away region charged transverse momentum sum density . . . 86
7-13 Drell-Yan transMAX and transMIN region charged transverse momentum sum density . . . 87
7-14 Drell-Yan transDIF region charged transverse momentum sum density . . . 87
7-15 Drell-Yan transverse region charged average transverse momentum . . . 88
7-16 Drell-Yan toward region charged average transverse momentum . . . 88
7-17 Drell-Yan away region charged average transverse momentum . . . 89
7-18 Drell-Yan transverse region charged maximum transverse momentum . . . 89
7-19 Drell-Yan toward region charged maximum transverse momentum . . . 90

7-20 Drell-Yan away region charged maximum transverse momentum 90
7-21 Drell-Yan transverse and toward regions charged multiplicity density 91
7-22 Drell-Yan transMAX, transMIN and toward regions charged multiplicity density 91
7-23 Drell-Yan all regions charged multiplicity density 92
7-24 Drell-Yan transverse and toward regions charged transverse momentum sum density 92
7-25 Drell-Yan transMAX, transMIN and toward regions charged transverse momentum sum density 93
7-26 Drell-Yan all regions charged transverse momentum sum density 93
7-27 Drell-Yan transverse and toward region charged average transverse momentum . 94
7-28 Drell-Yan all regions charged average transverse momentum 94
7-29 Drell-Yan transverse and toward charged maximum transverse momentum . . . 95
7-30 Drell-Yan all regions charged maximum transverse momentum 95
7-31 Drell-Yan all regions charged multiplicity density combined 96
7-32 Drell-Yan all regions charged transverse momentum sum density combined . . . 96
7-33 Drell-Yan and leading jet transverse region charged multiplicity density 97
7-34 Drell-Yan and leading jet transverse region charged transverse momentum sum density 97
7-35 Drell-Yan and leading jet transverse region charged average transverse momentum 98
7-36 Drell-Yan and leading jet transverse region charged maximum transverse momentum 98
7-37 Drell-Yan and leading jet transMAX and transMIN regions charged multiplicity density 99
7-38 Drell-Yan and leading jet transMAX and transMIN regions charged transverse momentum sum density 99
7-39 Drell-Yan and leading jet transDIF region charged multiplicity density 100
7-40 Drell-Yan and leading jet transDIF region charged transverse momentum sum density 100
7-41 Drell-Yan and leading jet away region charged multiplicity density 101
7-42 Drell-Yan and leading jet away charged transverse momentum sum density . . . 101

7-43 Drell-Yan mean charged transverse momentum against charged multiplicity . . . 102

7-44 Drell-Yan pair transverse momentum vs charged multiplicity 102

7-45 Drell-Yan mean charged transverse momentum against charged multiplicity, (pair $p_T < 10$ GeV/c) 103

8-1 Charged multiplicity density at LHC 107

Abstract of Dissertation Presented to the Graduate School
of the University of Florida in Partial Fulfillment of the
Requirements for the Degree of Doctor of Philosophy

USING DRELL-YAN TO PROBE THE UNDERLYING EVENT IN RUN II AT COLLIDER DETECTOR AT FERMILAB (CDF)

By

Deepak Kar

December 2008

Chair: Richard D. Field
Major: Physics

We study the behavior of charged particles produced in association with Drell-Yan lepton-pairs in the region of the Z-boson in proton-antiproton collisions at 1.96 TeV. We use the direction of the Z-boson in each event to define 'toward', 'away', and 'transverse' regions. For Drell-Yan production (excluding the leptons) both the 'toward' and 'transverse' regions are very sensitive to the 'underlying event', which is defined as everything except the two hard scattered components. The data are corrected to the particle level and are then compared with several PYTHIA models (with multiple parton interactions) and HERWIG (without multiple parton interactions) at the particle level (*i.e.* generator level). The data are also compared with a previous analysis on the behavior of the 'underlying event' in high transverse momentum jet production. The goal is to produce data that can be used by the theorists to tune and improve the QCD Monte-Carlo models of the 'underlying event' that are used to simulate hadron-hadron collisions.

CHAPTER 1
INTRODUCTION: THE STANDARD MODEL AND THE QCD

1.1 Overview

The focus of particle physics[1] is on our basic understanding of nature, leading to a more fundamental knowledge of matter, energy, time and space. The standard model of particle physics, summarized very briefly in the next section, provides a remarkably accurate description of elementary particles and their interactions. However it is incomplete in many respects, and experimental observations point to the possibilities of major discoveries in current and future high energy high energy particle colliders. In order to find new physics in these colliders, it is essential to have a very good understanding of the current physics, and that has been the motivation for this work. This is especially important now in view the large amount of good quality data we are getting from the Tevatron, currently the world's highest energy particle collider, and the new Large Hadron collider (LHC) starting up in Geneva, Switzerland.

1.2 Standard Model of Particle Physics

Four fundamental forces had been recognized to exist in nature. Gravity was first described accurately by Issac Newton but later underwent a profound reformulation in Albert Einstein's theory of general relativity, where it is understood to arise from the curvature of dynamical spacetime. Electromagnetic force is well described by Maxwell's equations and is responsible for interactions among the charged particles. The weak force, the third of the fundamental forces, is the mediator of processes involving neutrinos - nuclear beta decay is an example. Finally the strong force is describes the interactions between the so called 'colored' (*color* is essentially another quantum number, analogous

[1] Often called high-energy physics. It is not the high-energy which is studied, but high-energy is used as a tool.

to electric charge) components, the quarks, which do not exist freely in nature but are the constituents of neutrons, protons, pions and many other subnuclear particles.

In mid 1960's, the Weinberg-Salam model of electroweak interactions [1] put together electromagnetic interactions and the weak force into an unified framework. The theory is initially formulated with four massless particles that carry the forces. A process of symmetry breaking gives mass to three of these four particles - the W^+, the W^- and the Z^0, which particles are the carriers of the weak force. The particle that remains massless is the photon, which is the carrier of the electromagnetic force. This theory is termed as Quantum Electrodynamics (QED), as this a quantum version of the classical electrodynamics. We extend the theory to describe the strong color force and that is termed Quantum Chromodynamics (QCD) [2]. It is analogous to Quantum Electrodynamics, but contains color charges except electrical charges. Asymptotic freedom guarantees that perturbative expansions mostly fail - so deriving analytic results from the theory is extremely difficult. The carriers are the color force are eight massless colored gluons, and just like the quarks, they can not be observed in isolation.

The electroweak theory, together with QCD form the standard model [3] of particle physics. So far, we have mentioned the twelve force carriers, which are all spin zero or spin one bosons. The matter particles are spin half fermions, and are of two types, leptons and quarks. The leptons include the electron, the muon and the tau and the associated neutrinos for each of those. Since we must include their antiparticles, they add up to a total of twelve leptons. There are six different types of quarks, called flavors for historical reasons and the flavors are up, down, charm, strange, top and bottom. Each of these six quark flavors comes in three different colors, so including the colors and associated antiquark for each of them we end up with a total of thirty-six quarks - they in different combinations constitutes the hadrons. Figure 1-1 depicts the components of the standard model as described above. The quarks and gluons constituting the hadrons are often termed as partons.

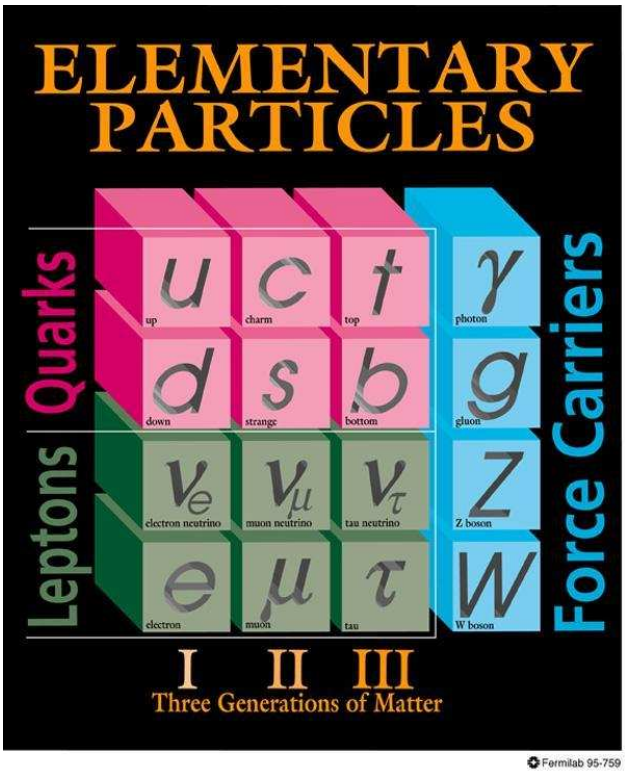

Figure 1-1. Components of The Standard Model of particle physics (Figure credit: DOE/Fermi National Accelerator Laboratory)

Standard Model summarizes current knowledge and is very much consistent with the available data. However it has significant shortcomings. It does not include gravity and that prevents any unified theory of all the forces. Standard Model admits only massless particles and we need spontaneous electroweak symmetry breaking to produce masses. This is the so called Higgs Mechanism [4], implementing which results in yet undetected Higgs Boson(s). The Higgs mechanism not only provides symmetry breaking and particle masses but also controls the high energy behavior of weak interactions. Apart from this, we do not know why the typical energy scale associated with the electroweak symmetry breaking (roughly, the typical size of all masses of elementary particles) is so much (10^{15} times) smaller than the Planck energy - which is known as the hierarchy problem. In fact there are about twenty parameters in standard model, such as masses and the couplings and mixing angles, that need to be put in by hand.

One of the popular alternatives is a more complete version of the Standard Model including Supersymmetry [5] - where every fundamental fermion has a superpartner which is a boson and vice versa. Since all matter particles are fermions and all force carriers are bosons, this symmetry unifies matter and force. Another alternative is String theory [6], which tries to unify gravity with the Standard Model. However, neither of these have been experimentally verified.

CHAPTER 2
THE EXPERIMENT: TEVATRON

2.1 Introduction

Rutherford's alpha particle scattering experiment was the the first demonstration that we need high energy particle scattering to probe deeper. To achieve good space resolution, *i.e.* to probe small distances, we need high center of mass energy of the particles scattering. Another reason for needing high energy is new particle production - a heavy particle would only be created if there is at least equivalent energy available. Very high energy collisions occur naturally in cosmic ray interactions and they also occurred in the early moments of our universe according to big bang cosmology. Both of these sources provide useful information, but systematic experimentation at high energy particle accelerators has proven to be much more useful. The particle accelerator experiments are of two types. In fixed target mode, accelerated particles hit set targets and we end up with fast moving light particles. Later came the collider mode experiments, in which counterrotating beams of particles produce head-on collisions, producing comparatively slowly moving, but heavier particles, since there is more center of mass energy available. The main advantage of colliding beams is that the total energy of the two beams is available for producing new particles, while in fixed-target experiments, much of the energy goes toward moving forward the particles those result from the impact with the target.

The hadronic colliders, where a proton is collided with either an antiproton (as in Tevatron in Fermilab) or with a proton (as in Large Hadron Collider in CERN) provide a convenient way to probe high energy domains and QCD predictions. The advantages of colliding hadrons are that, being heavier than leptons, lose much less fraction of energy by synchrotron radiation and the effective cross section is higher because of color degrees of freedom. However, leptonic colliders (LEP in CERN, proposed International Linear Collider) are much more 'cleaner', as all the processes are just QED processes, resulting

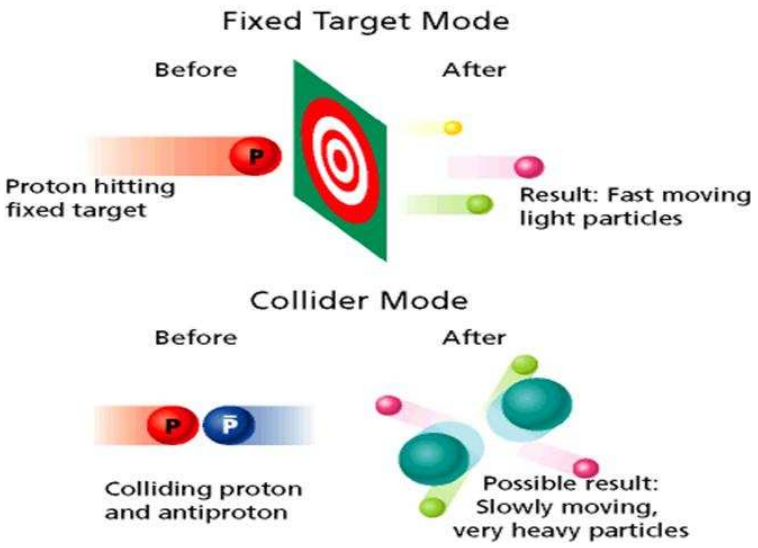

Figure 2-1. Fixed target and collider mode (Figure credit: Fermilab public webpage)

in smaller backgrounds and lesser multiplicities. However, we would be discussing hadron collisions in this dissertation, since the data we would be looking at came from proton antiproton collision at Tevatron in Fermi National Accelerator Laboratory near Chicago in Illinois.

2.2 The Tevatron

Tevatron is the highest energy particle collider in the world, colliding protons (sometimes would be referred as, p) and antiprotons (sometimes would be referred as, $\overline{p}$) at a center of mass energy of 1.96 TeV[1] . Fermilab uses a series of accelerators [7] to separately accelerate the protons and antiprotons to 980 GeV. The paths taken by p and $\overline{p}$ from initial acceleration to collision in the Tevatron is shown in the schematic diagram in Figure 2-1.

In the first stage, hydrogen gas is ionized to H^- ions and accelerated electrostatically to a kinetic energy of 750 KeV in the Cockcroft-Walton pre-accelerator [8], which is effectively a giant capacitor. Next, the H^- ions enter a linear accelerator (Linac) [9],

[1] Stands for Tera electronVolt, equivalent to 10^{12} times the energy gained by a single unbound electron when it is accelerated through an electrostatic potential difference of one volt, in vacuum.

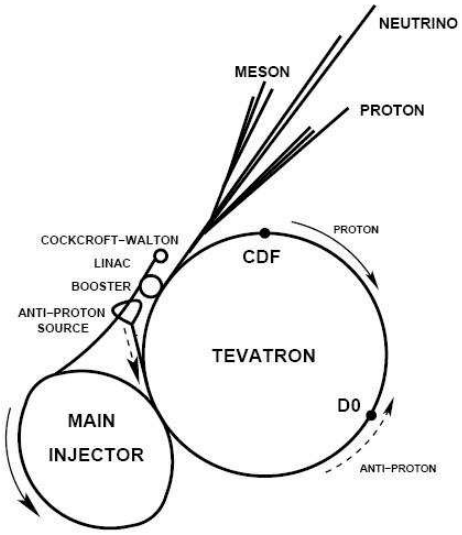

Figure 2-2. Schematic layout of the Fermilab accelerator complex. Protons (solid arrow) are accelerated at the Cockcroft-Walton, Linac, Booster, Main Injector and finally at the Tevatron. The antiprotons (dashed arrow) from the antiproton source are first accelerated at the Main Injector and then at the Tevatron (Figure Credit: Fermilab public webpage).

approximately 150 m long, where they are accelerated to 400 MeV. An oscillating electric field in the Linac's Radio Frequency (RF) cavities accelerates the ions and groups them into bunches. The force of the field acting on the ions accelerates them while they are in the cavities. The force of the field decelerates the ions they move through the RF-shielded drift tubes. Before entering the next stage, a carbon foil is used to remove the electrons from the H^- ions, leaving only the bare protons. The 400 MeV protons are then injected into the Booster, a circular rapid-cycling synchrotron of 74.5 m in diameter [9], with conventional magnets to focus and steer the beam. The protons travel around the Booster to be accelerated to a final energy of 8 GeV by another series of of RF cavities.

To produce antiprotons, protons from the Booster are accelerated to 120 GeV by the Main Injector [10] and collided with a nickel target [7]. This produces a wide spectrum of secondary particles, including antiprotons. About 20 antiprotons are produced per one million protons, with a mean kinetic energy of 8 GeV. The antiprotons are focused by a lithium lens and separated from other particle species by a pulsed magnet. The

collider requires narrow beams, so the transverse motion of the antiprotons are reduced in the Debuncher synchrotron. Since this process reduces the kinetic energy spread, it is referred to as 'cooling' the beam. They are collected and further cooled using stochastic cooling [11] in the 8 GeV Accumulator ring. It takes between 10 and 20 hours to build up a 'stack' of antiprotons which is then used for collisions in the Tevatron. Antiproton availability is most often the limiting factor for attaining high luminosities.

Once a sufficient number of $\overline{p}$ are collected, the stacks of protons and antiprotons are transferred to the Main Injector [10] for acceleration to 150 GeV and injection into the Tevatron [7]. The Main Ring is a 1 km in radius, rapid-cycling synchrotron ring with 3.5 kGauss conventional dipole magnets for steering the beam, quadrupole magnets for focusing, and an RF cavity that accelerates the p to 150 GeV before they are injected into the Tevatron. The stacks contain 36 bunches, with a proton bunch containing around 3×10^{11} protons and antiproton bunch containing around 3×10^{10} antiprotons. The same magnetic field in the Main Ring and Tevatron bends the p and $\overline{p}$ beam in the opposite direction, since they are oppositely charged. The Tevatron is the last stage of Fermilabs accelerator chain and it is 6.28 km in circumference. It receives 150 GeV p and $\overline{p}$ from the Main Injector and accelerates them to 980 GeV using superconducting magnets producing a magnetic field of 4.2 T. Quadrupole magnets focus the p and $\overline{p}$ bunches so that they collide at two points, termed B0 and D0. The two collider detectors, the Collider Detector at Fermilab (CDF) and DØ are built around the collision points, which observe the collisions, recognize the particles that are coming out and record the data for later analysis. This analysis uses data collected by the CDF experiment, and hence we would be describing in detail the CDF detector. CDF is international collaboration of 635 physicists from across 15 countries, spanning 63 institutions.

2.3 Collider Coordinates

Before describing the CDF detector in detail, we will need to know the coordinate system employed. In CDF the positive z-axis lies along the incident proton beam

direction, ϕ is the azimuthal angle, θ_{cm} is the polar angle, and p_T is the component of momentum in the transverse plane, as shown in Figs. 2-2 and 2-3.

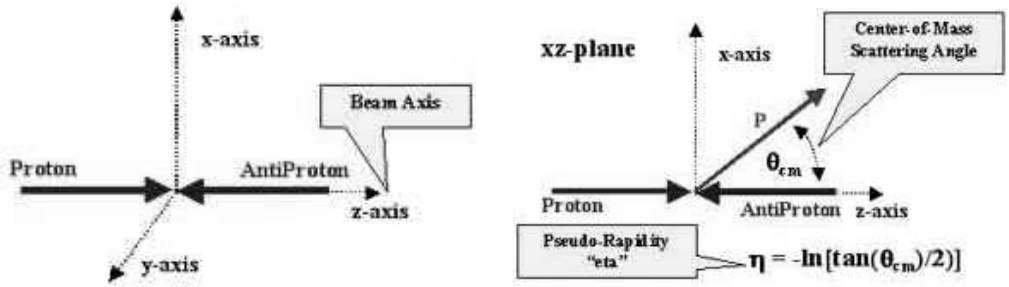

Figure 2-3. Defining collider coordinates: z-axis and polar angle θ

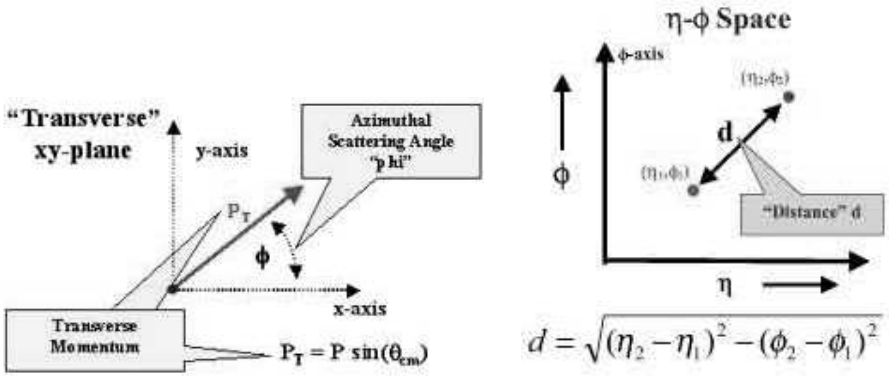

Figure 2-4. Defining collider coordinates: transverse momentum and $\eta - \phi$ space

The rapidity is defined as $y = \frac{1}{2}\ln(\frac{E+p_z}{E-p_z})$. For massless particles (which are a good approximation for the decay products of almost anything in a collider), the rapidity y reduces to the pseudorapidity,

$$\eta = -\ln\tan\theta_{cm}/2 \tag{2–1}$$

$\eta - \phi$ space corresponds to a rectangular coordinate system in which η is plotted on one axis and ϕ is plotted on the other. The direction of an outgoing particle is represented by a point in $\eta - \phi$ space. Particles traveling in the same direction lie near each other in $\eta - \phi$ space (*i.e.* small distance d). Collider detectors are designed so that each detector element covers the same area in $\eta - \phi$ space. The primary reason for using the rapidity, as shown in

Figure 2-4, in place of the polar angle is that differences of rapidity are Lorentz invariant for boosts along the z (or the rapidity) axis. In Figure 2-4, the sphere has lines drawn at pseudo-rapidity intervals. The cylinder is after the transformation to pseudo-rapidity space. We can clearly see that $\eta - \phi$ coordinates exploit the cylindrical symmetry better. The table in Figure 2-4 shows how the polar angle is mapped into pseudorapidity.

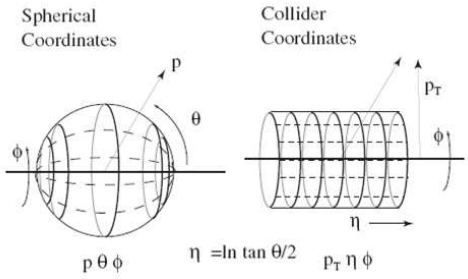

η	θ_{cm}
0	90°
1	40°
2	15°
3	6°
4	2°

Figure 2-5. Advantage of using η-ϕ coordinates and mapping of polar angle to psuedorapidity

2.4 The CDF Detector

2.4.1 Overview

The CDF Run II detector [12], in operation since 2001, is an azimuthally and forward-backward symmetric solenoidal particle detector designed to study $p\overline{p}$ collisions at the Tevatron. It is a multipurpose detector, meaning the design is not aimed at one particular physics measurement, but rather at extracting generally useful information about the created particles. It combines precision charged particle tracking with fast projective calorimetry and fine grained muon detection. The CDF detector is shown in Figure 2-5 with a quadrant cut out to reveal the different sub-detectors, arranged coaxially around the beam-pipe, which are described next.

The momentum component of all hadrons, electrons, muons and photons transverse to the beam axis are measured (particles that escape along the beam pipe have negligible transverse momentum) and any significance imbalance in transverse momentum, termed as

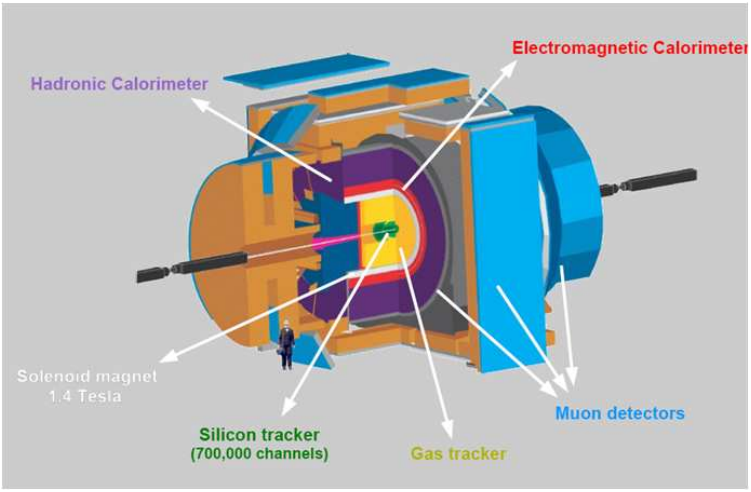

Figure 2-6. Schematic diagram of the CDF Run II detector (Figure credit: CDF public webpage)

missing energy can be attributed to penetrating neutral particles (mostly neutrinos) which have passed undetected.

We will describe how electrons, muons and charged tracks, which are used in this analysis are identified and reconstructed in the relevant detector components in greater detail in Chapter 6.

2.4.2 Tracking Systems

Tracking systems are the innermost component and are contained in a superconducting solenoid, 1.5 m in radius and 4.8 m in length, which generates a 1.4 T magnetic field parallel to the beam axis. It is designed to detect charged particles and measure their momenta (curvature gives the momentum and sign of charge) and displacements from the point of collision, termed the the primary interaction vertex. The inner, high resolution section built of silicon detects the decays of short lived particles and the outer tracker is optimized for momentum measurement. The tracking system consists of a silicon microstrip system [13] and of an open-cell wire drift chamber [14] that surrounds the silicon. The silicon microstrip detector consists of seven layers (eight layers for $1.0 < |\eta| < 2.0$) in a barrel geometry that extends from a radius of $r = 1.5$ cm from the beam line to $r = 28$ cm. A silicon tracking detector is a effectively a reverse biased p-n

junction. A charged particle passing through the detector causes ionization producing electron-hole pairs in the semiconductor material. Electrons drift toward the anode, and holes drift toward the cathode, where the charge is gathered. By segmenting the p or n side of the junction into 'strips' and reading out the charge deposition separately on every strip, the position of the charged particle is measured. The layer closest to the beam pipe is a radiation-hard, single sided detector called Layer 00 (L00). The remaining seven layers are radiation-hard, double sided detectors. The first five layers after Layer 00 comprise the silicon sensors (SVXII) and the two outer layers comprise the Intermediate Silicon Layers (ISL) system. This entire system allows track reconstruction in three dimensions.

Surrounding the silicon detector is the Central Outer Tracker (COT) [14], a 3.1-m-long long cylindrical drift chamber covering the radial range from 40 to 137 cm. It is filled with with fast gas (50% argon, 50% ethane) to make drift times small enough so that the hits can be read out between each Tevatron bunch crossing. It is organized into 8 alternating superlayers of 4 stereo ($\sim 2^\circ$) and 4 axial wire planes, providing 96 mesaurements layers. A COT cell has 12 sense wires oriented in a plane, at $\sim 35^\circ$ with respect to radial direction for Lorentz drift, a group of such cells at given radius forms a superlayer (SL). The COT provides coverage for $|\eta| \leq 1$.

A Time-of-Flight (TOF) detector [15], based on plastic scintillators and fine-mesh photomultipliers is installed in a few centimeters clearance just outside the COT. The TOF resolution is $\pm$ 100 ps and the timing information from the TOF can be combined with the momentum measurement from the COT to deduce a particle's mass. The default COT tracking algorithm first reconstructs track segments in each of eight superlayers. It checks for hits loosely consistent with a straight line, using a tolerance of 20 ns. The identified hits in each segment are then fit to a circular trajectory.

2.4.3 Calorimeters

Segmented electromagnetic and hadronic sampling calorimeters [16] surround the tracking system and measure the energy of interacting particles. Particles make showers

which deposit energy and are sampled via their ionization. A high energy jet is seen as a localized peak of hadron energy in a small group of adjoining calorimeter cells , interpreted as originating in one or several nearly collinear quarks or gluons with corresponding energy and direction.

The major mode of energy loss of electrons or positrons interacting with matter at high energies is through radiation of photons (*i.e.* bremsstrahlung: $e^- \rightarrow \gamma + e^-$). For high energy photons the dominant interaction process is pair production (*i.e.* $\gamma \rightarrow e^+e^-$). An electron or photon through these two processes to produces a shower of photons and electrons in the calorimeter. This phenomena, termed as an electromagnetic (EM) shower [17, 18] is shown in Figure 2.6. The shower develops until the energy reaches a critical energy (approx 600 MeV) and ionization losses equal those of bremsstrahlung. A similar phenomena occurs when hadron interact with matter, which is referred to as a hadronic shower. An incident hadron undergoes an inelastic collision with nuclear matter in the detector resulting in secondary hadrons. These hadrons also undergo inelastic collisions. As many different processes contribute to the development of a hadronic shower, the modeling of the shower is much more complex than an EM shower.

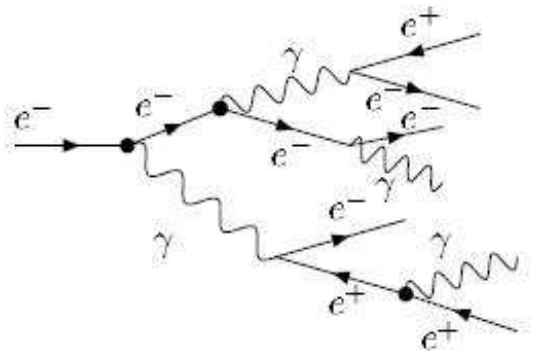

Figure 2-7. Development of an electromagnetic shower

The calorimeter has a projective tower geometry; it is segmented in η and ϕ towers that point to the interaction region. The coverage of the calorimetry system is 2π in ϕ and $|\eta| < 4.2$ in pseudo-rapidity. The calorimeter system is divided into three regions

from smallest η to largest: central, plug and forward. Each calorimeter tower consists of an electromagnetic shower counter followed by a hadron calorimeter. This allows for comparison of the electromagnetic and hadronic energies deposited in each tower, and therefore separation of electrons and photons from hadrons. The central electromagnetic calorimeter (CEM) uses lead sheets interspersed with polystyrene scintillator as the active medium and employs phototube readout. The central hadronic calorimeter (CHA) uses steel absorber interspersed with acrylic scintillator as the active medium. The central calorimeters (and the endwall hadronic calorimeter) cover the pseudorapidity range $|\eta| < 1.1(1.3)$. The plug calorimeters cover the pseudorapidity region $1.1 < |\eta| < 3.64$. They are sampling scintillator calorimeters with gas proportional chambers which are read out with plastic fibers and phototubes.

2.4.4 Muon Chambers

The muon system [19] resides beyond the calorimeters. When interacting with matter, muons act as minimally ionizing particles (low bremsstrahlung radiation due to their relatively large mass); they only deposit small amounts of ionization energy in the material. They are the only particles likely to penetrate both the tracking and five absorption lengths of calorimeter steel, and leave tracks in the muon detection system. The CDF detector has four muon systems: the Central Muon Detector (CMU), Central Muon Upgrade Detector (CMP), Central Muon Extension Detector (CMX), and the Intermediate Muon Detector (IMU). CMU consists of four layers of planar drift chambers and detects muons with $p_T > 1.4$ GeV/c. The CMP's are additional four layers of planar drift chambers instrument and detects muons with $p_T > 2.0$ GeV/c. CMX detector is made of drift cells and scintillation counters, which are used to reject background based on timing information. Using the timing information from the drift cells of the muon systems, short tracks (called 'stubs') are reconstructed. Tracks reconstructed in the COT are extrapolated to the muon systems. For good quality muons, an upper limit is placed on the χ^2 fit value of track-stub match. The CMU, CMP and CMX chambers each provide

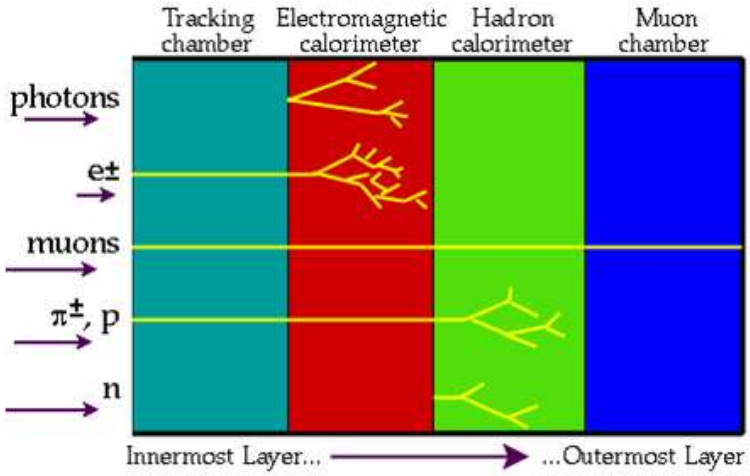

Figure 2-8. Different particles are being detected at the CDF detector (Figure credit: CDF public webpage)

coverage in the pseudo-rapidity range $|\eta| < 0.6$. The IMU covers the region $1.0 < |\eta| < 1.5$. The uninstrumented regions have been filled with so called miniskirt and keystones.

2.4.5 Luminosity Counter

The beam luminosity is determined by using gas Cherenkov counters [20] located in the $3.7 < |\eta| < 4.7$ region which measure the average number of inelastic $p\overline{p}$ collisions per bunch crossing. This was built by the University of Florida group in CDF. When charge particles travel faster than the speed of light in a medium they emit Cherenkov radiation. This effect is used to measure the average number of inelastic $p\overline{p}$ collisions per bunch crossing in order to calculate the instantaneous luminosity delivered by the Tevatron. The instantaneous luminosity provided by the CLC must be integrated with respect to time to calculate the integrated luminosity.

Luminosity measures the flux of particles capable of creating a reaction of interest. The number $N_{observed}$ of events observed in an experiment is given by,

$$N_{observed} = [\sigma_{observed} \times \epsilon_{detection} \times \int Ldt] + N_{background}, \tag{2–2}$$

where the observable $\sigma_{process}$ is the cross section for the process and should not depend on the experimental details, $\epsilon_{detection}$ is the probability that a signal event will be observed in

a given detector, $\int Ldt$ is the Integrated Luminosity and $N_{background}$ are events from other processes that got counted incorrectly. At colliders, the luminosity depends on both the beam intensities and the beam densities and is given by,

$$L = f\frac{N_p N_{\bar{p}}}{4\pi\sigma_x\sigma_y}, \tag{2–3}$$

where f is the frequency with which beam bunches cross, N_p is the number of protons/bunch, $N_{\bar{p}}$ is the number of anti-protons/bunch and σ_x and σ_y are the gaussian sizes of the beam. For integrated luminosities, we normally use inverse picobarns (1 picobarn^{-1} = 10^{36} cm^{-2}) as a unit.

The delivered integrated luminosity per week is about 25 pb^{-1} and CDF has more that 3.0 fb^{-1} of data collected on tape (More than 20 times the Run I integrated luminosity). At the Tevatron we are beginning to measure cross-sections that are at the 1 pb level or smaller, which is very exciting. We are getting large amount of high quality data from CDF, with potential for many good physics analysis. We expect 6 - 8 fb^{-1} of data by end of 2009.

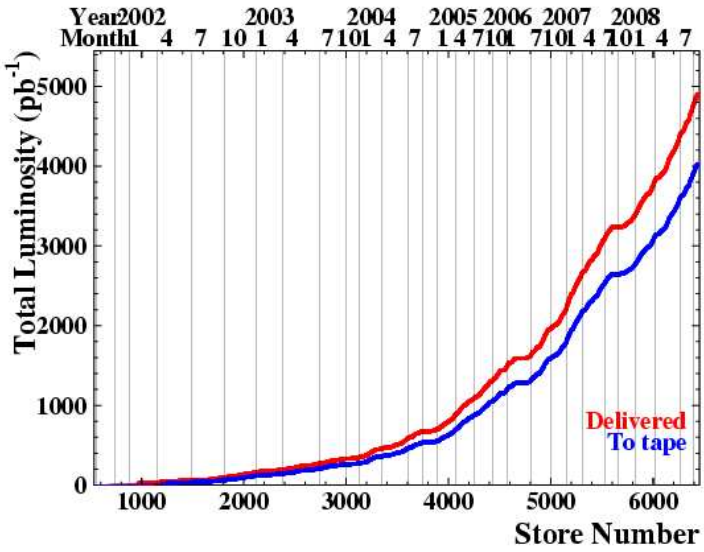

Figure 2-9. A graph of CDF luminosity with time, showing the remarkable improvement over the years (Figure credit: CDF public webpage)

2.4.6 Trigger System

The trigger plays an important role in hadron collider experiments because the collision rate is much higher than the rate at which data can be stored at tape. At the Tevatron, $p\bar{p}$ collisions happen at a rate of 2.5 MHz, and the readout of the full detector produces 250 kB of data. There is no medium available which is capable of recording data this quickly, nor would it be practical to analyze all of this data later on.The CDF trigger system [22] has a three level architecture with each level providing a rate reduction sufficient to allow for processing in the next level with minimal deadtime[2] .

Level-1 uses custom designed hardware to find physics objects based on a subset of detector information and makes a decision based on simple counting of these objects. Based on preliminary information from tracking (track p_T), calorimetry (jet object, em object, missing E_T, sum E_T) and muon tracks, the output of the first level of the trigger is used to limit the rate. It is a synchronous 40 stage pipeline. Level-1 decision always occurs 5.5 μs after the collision (*i.e.* every 14 collisions). The 14 events are stored in a pipelined buffer whilst the Level-1 decisions are made. When an event is accepted by the Level-1 trigger, all data is moved to one of four Level-2 buffers in the front-end electronics, where with better granularity and additional tracking information from the silicon detector, the rate is reduced further. Decision takes ≈ 30 μs per event. The third and final level of the trigger, with access to the complete event information and full detector resolution, uses software algorithms and a computing farm, and reduces the output rate to $\approx$ 100 Hz, which is written to the permanent storage.

Different triggers are required to select events with different signatures. To measure a particular type of interaction, it must be selected and separated from all other possible interactions and triggers are used for that - only interactions that satisfy some specific

[2] If it is not possible for the system to accept an otherwise good event because buffers are full, we refer to this as deadtime.

Table 2-1. Rate reductions at CDF 3 level trigger system

Trigger level	Rate reduction	Ratio
Level 1	1.7 $MHz \rightarrow 25\ kHz$	1:70
Level 2	25 $kHz \rightarrow 600\ Hz$	1:40
Level 3	600 $Hz \rightarrow 100\ Hz$	1:6
Net		1:17000

preselected criteria are selected and recorded. Often further selection cuts in different variables are made to refine the event. Sometimes the rates of some triggers are too high to sustain at high luminosity, the trigger is prescaled by a constant factor - that fraction of the events satisfying the trigger criteria are randomly rejected.

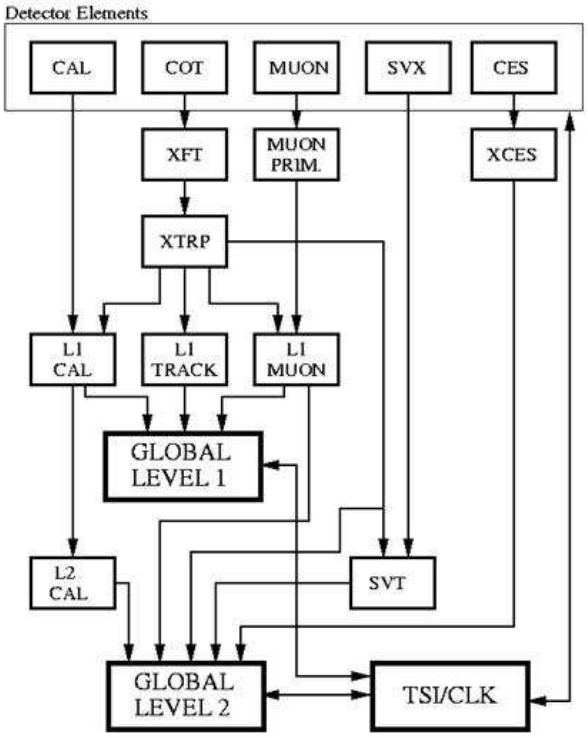

Figure 2-10. A flowchart showing the CDF trigger system (Figure credit: CDF public webpage)

2.4.7 Run II Upgrade

Between 1997 and 2001, the accelerator complex underwent major upgrades aimed at increasing the luminosity of the accelerator to provide 2 fb^{-1} of integrated luminosity or more. The upgraded machine accelerates 36 bunches of protons and antiprotons,

whereas the original machine accelerated 6 bunches. Consequently, the time between bunch crossings has been decreased to 396 ns. Major differences for Run II, from Run 0 and Run 1 [21] include, the replacement of the central tracking system; the replacement of a gas sampling calorimeter in the plug-forward region with a scintillating tile calorimeter; preshower detectors; extension of the muon coverage, a TOF detector and upgrades of trigger, readout electronics, and data acquisition systems. The upgraded CDF II Detector provides us better solid angle coverage and particle identification.

CHAPTER 3
COLLIDER PHENOMENOLOGY

3.1 Overview of Hadronic Collisions

The total proton-antiproton cross section is the sum of the elastic and inelastic components, $\sigma_{Total} = \sigma_{EL} + \sigma_{IN}$ [23], as shown in Figure 3-1. 25% of the time, after the collision, the proton and the antiproton scatter elastically through a small angle, exchanging momentum but there are no new particles or energy loss, which is not very interesting from our perspective. The rest of the time we have inelastic collision, where one or both hadrons have a change in energy and direction. The inelastic cross section consists of three terms; single diffraction (SD), double-diffraction (DD), and everything else (referred to as the 'hard core'), $\sigma_{IN} = \sigma_{SD} + \sigma_{DD} + +\sigma_{DD}$. In SD (12%), one of the incident particle splits up into other particles and the other particle leave at a small angle on the other side. In DD (8%) both the proton and the antiproton dissociates into a bundle of hadrons and and travel at relatively small angles on either side. We are mostly interested in the (non diffractive) hard core part - part of it is the soft collision, where the beam hadrons 'ooze' through each other producing lots of soft particles with a uniform distribution in rapidity and many particles flying down the beam pipe. Occasionally there is a hard scattering among constituent partons, producing outgoing particles with large p_T in the transverse region. By soft we mean low transverse momenta transfer from initial to final state and very few or no particles produced with significant p_T. In contrast, interactions involving the creation of at least one one particle with appreciable p_T is termed hard scattering. Hard interactions can be calculated reliably using perturbative QCD while soft interactions are not easily calculable within QCD and rely on ad-hoc models which are taken from data (with some theory).

Experimentally it is difficult to separate σ_{HC} from σ_{DD}. At 1.8 TeV (CDF Run 1) the total proton-antiproton cross section is about 78 mb and the elastic cross section is about

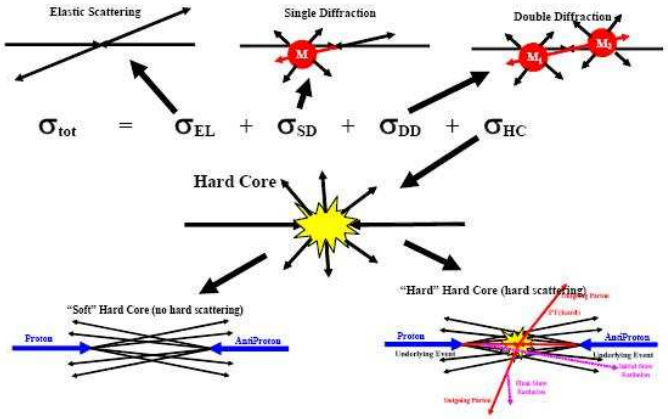

Figure 3-1. Shows the various components of the proton-antiproton total cross section

18 mb [24]. Single diffraction makes up about 9 mb of the 60 mb inelastic cross section and $\sigma_H C + \sigma_D D$ =51 mb, with double diffraction in the range $4 < \sigma_{DD} < 7$ mb.

3.2 Typical Collider Event

A typical 2-to-2 hard scattering event is a proton-antiproton collision at the hadron colliders as shown in the Figure 2-2, all happening inside the radius of a proton [25]. The incoming fundamental particles are the quarks and gluons inside the hadrons and the strong force is the dominant interaction.

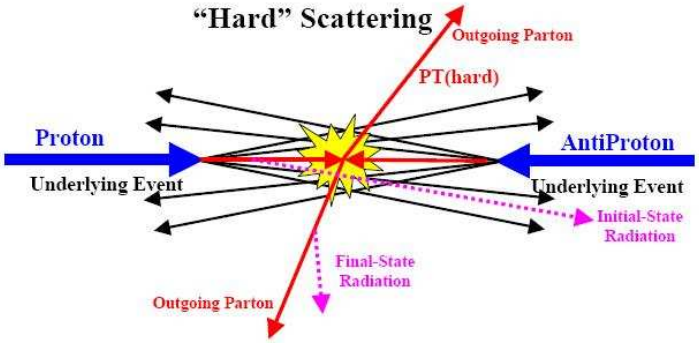

Figure 3-2. Shows the various components of a hard scattering process

Since the longitudinal momentum fraction $x = p_{parton}/p_{proton}$ of the proton momentum carried by the parton is given by by Parton Distribution Functions or PDFs ($f_i(x;\mu)$, where i is the parton flavor and μ is an appropriate hard scattering scale for the

interaction), at a particular collision we we do not know the longitudinal momentum of the initial state partons. The hard collision of interest hence occurs only with a certain probability, termed the branching fraction. We can say that hard collision of interest only occurs when partons with the right quantum numbers happen to have the right center of mass energy to make the desired final state - which is not the case most of the times [25]. Figure 3-3 shows the the first order hard scattering diagrams for proton antiproton scattering. By looking at the at the typical parton distribution functions [26], we can see that gluons are the most probable partons, except at the highest momentum fractions. The cross section at very low p_T is dominated by gluon-gluon and quark-gluon scattering via the t channel.

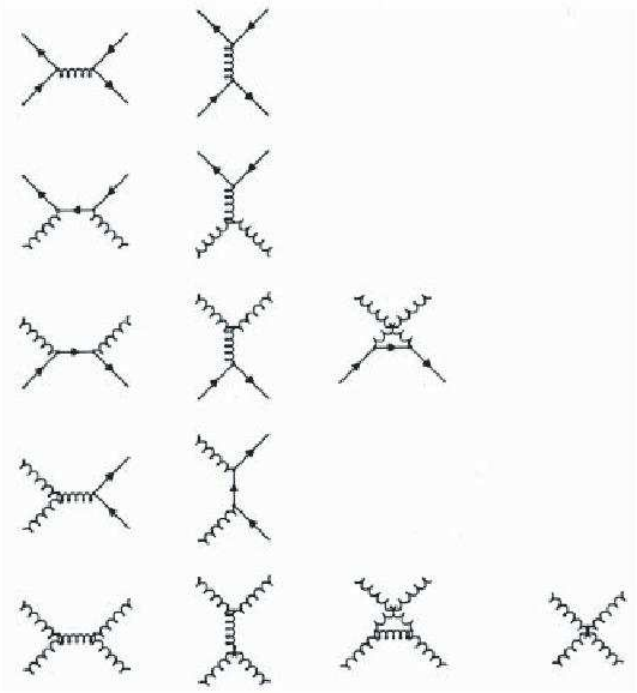

Figure 3-3. First order diagrams for proton-anti-proton scattering. If one assumes that time runs bottom to top (the theorists convention), the first column indicate exchange in the t channel, the second s channel exchange, the third the u channel and the 4th is a special QCD diagram.

We can not see free quarks and gluons appearing at final stage because of color confinement and strong interaction. For example when a quark is knocked out of the

proton it remains connected to the proton by its color charge and at some point the energy in the color field becomes so high that it is energetically favorable to produce a quark anti-quark pair to neutralize some of the color field. This process goes on till the color neutral objects have 'hadronized' (wherein the colored partons are transformed into jets of colorless hadrons, photons and leptons) to form reasonably long lived observable hadronic particles such as π^+, π^-, π^0, K^+, K^-, K_L, K_S, η, $\eta\prime$, p, n etc. The π^0, η decay quickly into photons. Naively this bunch of collimated hadrons, produced by the hadronization of partons and following the path of the original quark or gluon, is referred to as a jet [27], although technically we need an algorithm to properly define a jet.

There can be corrections to this simple picture from various effects. Firstly, there are QED and QCD bremsstrahlung-type modifications, and because of the largeness of the strong coupling constant α_s and the presence of the triple gluon vertex, QCD emission off quarks and gluons is especially prolific. We therefore speak about parton showers, shown in Figure 3-4 [28] wherein a single initial parton may give rise to a whole bunch of partons in the final state. Also photon emission may give sizable effects in QED processes. The bulk of the bremsstrahlung corrections are universal, *i.e.* do not depend on the details of the process studied, but only on one or a few key numbers, such as the momentum transfer scale of the process. Secondly, we have true higher-order corrections, which involve a combination of loop graphs and the soft parts of the bremsstrahlung graphs above, a combination needed to cancel some divergences.

3.3 The Underlying Event

In addition to the the two hard scattered outgoing parton, which fragment into jets - there is initial and final state radiation (caused by bremsstrahlung and gluon emission), resonance decays, multiple parton interaction (additional 2-to-2 scattering within the same event), hadronization, 'beam beam remnants' (particles that come from the breakup of the proton and antiproton, from the partons not participating in hard scatter). We define the 'underlying event' [29] as everything except the hard scattered components and it includes

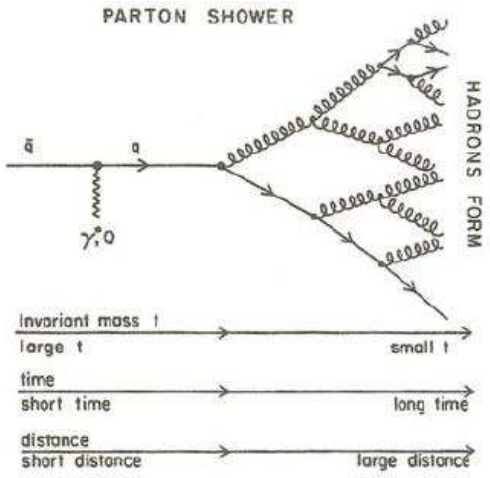

Figure 3-4. A parton shower in which a quark initially produced, radiates gluons which in turn radiate additional gluons and quark-antiquark pairs. As time increases the shower progresses to larger distances from the point where in initial quark was produced and hadrons are formed.

the 'beam-beam remnants' plus the multiple parton interaction. The 'hard scattering' component consists of the outgoing two jets plus the initial and final-state radiation. The 'beam-beam remnants' are what is left over after a parton is knocked out of each of the initial two beam hadrons as in Fig 3-5. It is the reason hadron-hadron collisions are more 'messy' than electron-positron annihilations and no one really knows how it should be calculated. Also, multiple parton scattering contributes to the 'underlying event'. In addition to the hard 2-to-2 parton-parton scattering and the 'beam-beam remnants', sometimes there is a second 'semi-hard' 2-to-2 parton-parton scattering that contributes particles to the underlying event as in Figure 3-5. However, from an experimental point of view, it is impossible to uniquely separate the hard scatter from the underlying event cleanly on an event by event basis. For example, soft gluons (QCD radiation) emitted from the hard scatter quarks would typically be part of the underlying event but where soft gluons become hard gluons and since not part of the underlying event is not an exact definition. If it is of high enough p_T to hadronize into a jet then it is generally considered hard, but that also depends on the chosen jet algorithm.

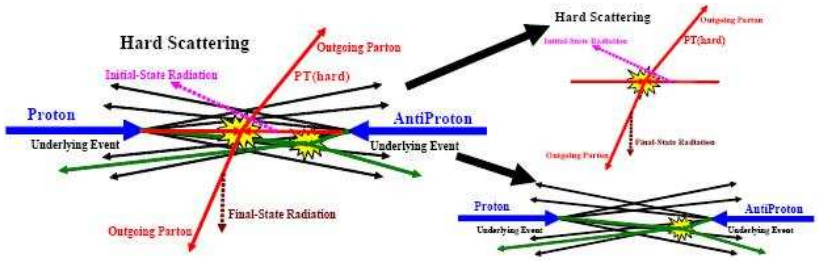

Figure 3-5. The underlying event consists of everything except the hard scattered components, beam-beam remnants and multiple parton interactions.

The environment at hadron colliders are dominated by hard scattering events and these hard scattering events are contaminated by underlying events. They are unavoidable background to all collider observables. For example, at the Tevatron both the inclusive jet cross section and the b-jet cross section, as well as isolation cuts, measurement of missing energy depend sensitively on the underlying event. In all precision measurements of hard interactions where soft effects need to be subtracted, higher the precision of the underlying event modeling, higher the accuracy of physics measurements. In fact, as we discussed before it is not possible on an event-by-event basis to be certain what particles came from the underlying event and, which particles originated from the hard scattering. Increasing luminosity implies more hadronic collisions resulting in more underlying events (which is technically know as the pileup[1]). They are generally not well understood since non perturbative physics is involved. However we do need to understand the underlying events to eliminate them and look at the desired physical processes cleanly.

3.4 Minimum Bias Collisions and the Underlying Event

We have already defined underlying event as everything except the two outgoing hard scattered components. 'Minimum bias event' [23], although different from the underlying event, is another excellent place to look at the theoretically poorly understood softer

[1] In high-luminosity colliders, there is a non-negligible probability that one single bunch crossing may produce several separate events.

physics. As discussed in Section 2.5, One selects (*i.e.* 'triggers' on) certain events to store onto tape. Minimum bias (or 'min-bias') is a generic term which refers to events that are selected with a 'loose' trigger that accepts a large fraction of the inelastic cross section (ideally with totally inclusive trigger). In principle it contains all types of interactions proportionally to their natural production rate.

All triggers produce some bias and the term min-bias is meaningless until one specifies the precise trigger used to collect the data. The CDF 'min-bias' trigger consists of requiring at least one charged particle in the forward region $3.2 < \eta < 5.9$ and simultaneously at least one charged particle in the backward region $-5.9 < \eta < -3.2$. Monte-Carlo studies show that the CDF 'min-bias' collects most of the σ_{HC} contribution plus small amounts of single and double diffraction. It is characterized by having no high p_T objects (jets, leptons, photons) and being isotropic (low p_T tracks at all ϕ in a tracking detector and uniform energy deposits in calorimeter as function of rapidity). The underlying event in a hard scattering process is evidently not the same as min bias event. The underlying event produces tracks in the detector and energy in the calorimeter, thus affecting the measurement of the hard scattering component. There are presence of initial and final state radiation in underlying event as well as color interactions with hard scattering. At the Tevatron about 1% of min-bias events contain a jet with 10 GeV transverse energy. At the LHC we expect this fraction increase by more than a factor of 10. The CDF underlying event analysis showed [76] that the density of particles in the underlying event in jet events is about a factor of two larger than the density of particles in a typical min-bias collision. At the LHC the difference might be even greater.

3.5 Dividing Into Regions

Experimentally it is possible to take advantage of the topological structure of hadron-hadron collisions to study the underlying event [30]. The direction of the leading calorimeter jet is used to isolate regions of $\eta - \phi$ space that are sensitive to the underlying event. The angle $\Delta\phi = \phi - \phi_{leading\ jet}$ is the relative azimuthal angle between charged

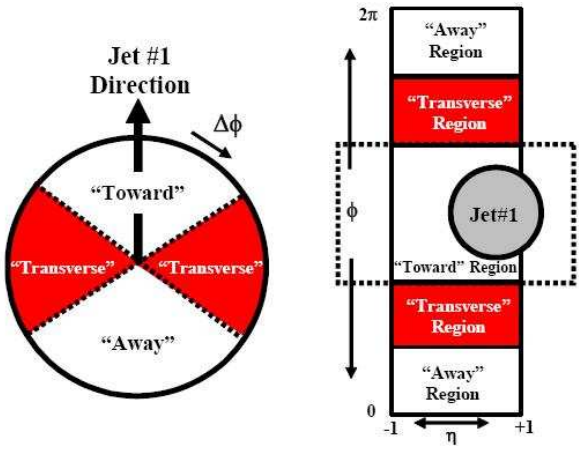

Figure 3-6. Different regions in $\eta - \phi$ space, with relative to the leading jet

particles coming from the underlying event and the direction of hard scattered leading jet, as in Figure 3-6. Later we would be looking at lepton pair production from the decay of a Z boson, then $\Delta\phi$ would be determined relative to the direction of the Z boson, as in Figure 3-7. We split the central region defined between $|\eta| < 1$ as follows,

- $|\Delta\phi| < 60^\circ$ as the toward region.
- $60^\circ < |\Delta\phi| < 120^\circ$ as the transverse region. And,
- $|\Delta\phi| > 120^\circ$ as the away region.

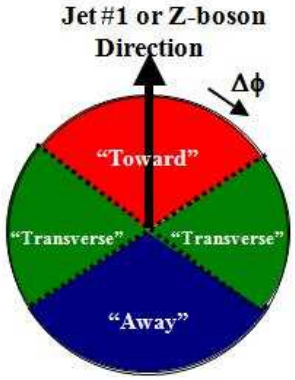

Figure 3-7. Different regions in $\eta - \phi$ space, with relative to the Z-boson

For hard scattered jets the transverse regions are most sensitive to underlying events, since they are perpendicular to the plane of 2-to-2 hard scattering. For them we

have outgoing jets in toward regions, almost impossible to separate them out from the background.

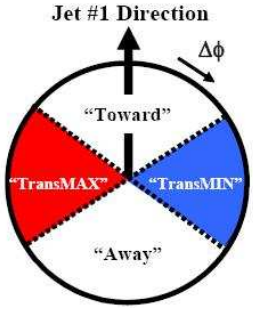

Figure 3-8. The transMAX and transMIN regions

As illustrated in Figure 3-8, we define MAX and MIN transverse regions which help to separate the hard component (initial and final-state radiation) from the beam-beam remnant component. MAX (MIN) refer to the transverse region containing largest (smallest) number of charged particles or to the region containing the largest (smallest) scalar $p_T$sum of charged particles, on an event by event basis. For events with large initial or final-state radiation the 'transMAX' region would contain the third jet in high p_T jet production or the second jet in Drell-Yan production while both the 'transMAX' and 'transMIN' regions receive contributions from the beam-beam remnants. Hence one expects that the transMAX region will pick up the hardest initial or final-state radiation while both the transMAX and transMIN regions should receive beam-beam remnant contributions. Hence one expects the transMIN region to be more sensitive to the beam-beam remnant component of the underlying event, while the transMAX minus the transMIN (*i.e.*, transDIF) is very sensitive to hard initial and final-state radiation. This idea, was first suggested by Bryan Webber and Pino Marchesini [31], and implemented in a paper by Jon Pumplin [32].

CHAPTER 4
THE DRELL-YAN PROCESS

4.1 Historical Perspective

The Drell-Yan process is where quarks and antiquarks from the incoming hadron beams annihilate to produce a virtual photon or Z^0, which decays to a lepton pair, as shown in Figure 4-1.

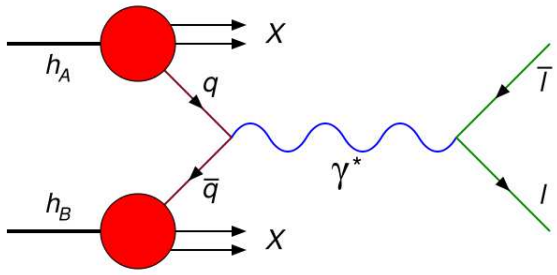

Figure 4-1. Schematic representation of the Drell-Yan lepton pair production

The initial studies on muon pair production in hadron hadron collisions was first done at BNL (Brookhaven National Laboratory) by Christenson *et al.* and their results are shown in Figure 4-2 [33]. A couple of interesting features were observed. The shoulder like structure near the muon pair mass of 3 GeV/c^2, which was later [34] discovered to be the J/ψ particle. The rapid fall in in cross section with increasing dilepton mass was not consistent with the point like cross sections observed in deep inelastic electron scattering. Calculations of Drell and Yan (1970, 1971) [35] explained most features of the process by extending the the parton model [36] developed to explain deep inelastic lepton scattering and this process came to be known as the Drell-Yan process. However the overall rate was underestimated by a factor of around 2, which was later predicted by the QCD calculations, taking into effect the gluon emission and absorption. Also resulting large average transverse momenta of dileptons was initially not well understood - QCD effects of gluon emission and gluon scattering provided the explanation. We will us now describe the process in detail, following [37].

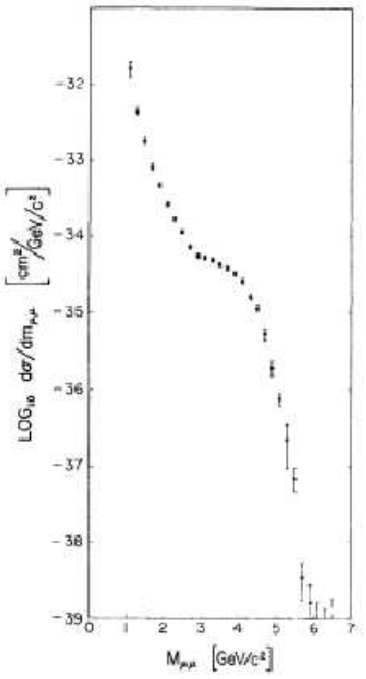

Figure 4-2. Dimuon spectrum from the BNL (Brookhaven National Laboratory) experiment

4.2 Cross Section Calculations for the Drell-Yan Process

In the first step a single antiquark from one hadron on a single quark from the other hadron annihilate to produce a virtual photon. The virtual photon subsequently converts to a pair of oppositely charged leptons, as depicted in Figure 4-3.

If the invariant mass M of the dilepton is large compared to the nucleon mass, then according to Heisenberg uncertainty principle, the time of interaction is short on the nuclear scale and the annihilating quark-antiquark pair does not interact with other components of the parent hadrons. The cross section in this approximation[1] is the

[1] Formally called impulse approximation, if the time duration for external current probe τ_{probe} is much shorter than the lifetimes of the relevant intermediate states $\tau_{intermediate.states}$ then the constituents can be treated as free. Lepton pair production by bremsstrahlung does not does not satisfy this approximation. In more modern language, the impulse approximation is replaced by the more precise concept of factorization which separates the the long distance and the short distance physics.

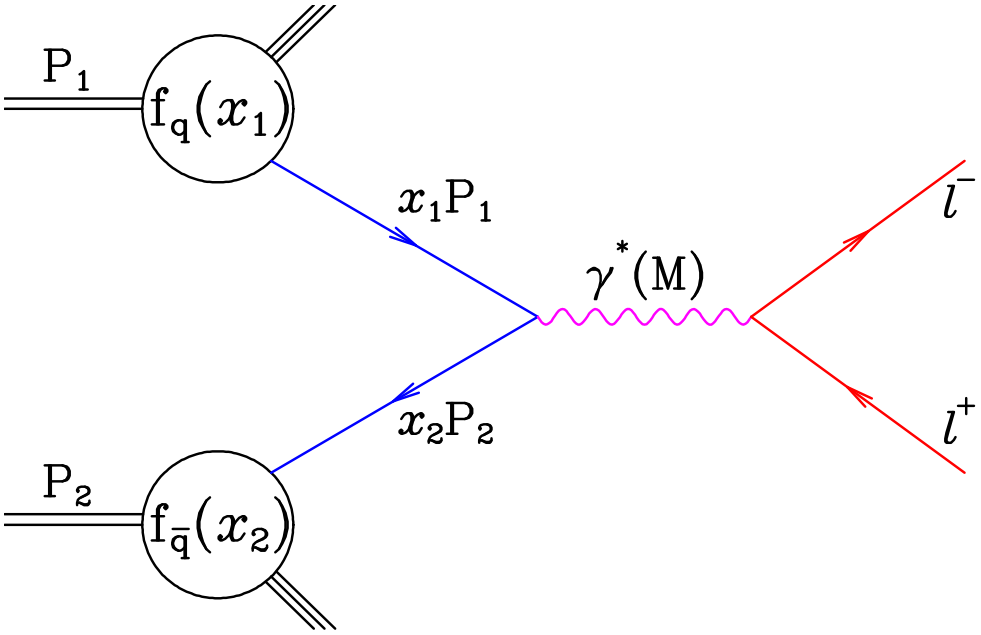

Figure 4-3. Feynman diagram for the Drell-Yan process

product of probability to find the particular parton configuration and the cross section for free partons.

So for the Drell-Yan process,

$$A(P_1) + B(P_2) \rightarrow l^+ + l^- + X \tag{4–1}$$

where the incoming hadrons A and B have momenta P_1 and P_2 respectively and X denotes any additional final state particle, we would write the total cross section as a convolution of the hard partonic scattering cross section with the parton densities of the hadrons A and B, and summing over all quark-antiquark combination,

$$\sigma = \sum_{q,\bar{q}} \int dx_1 dx_2 f_q(x_1) f_{\bar{q}}(x_2) \hat{\sigma}_{q\bar{q}\rightarrow l^+l^-} \tag{4–2}$$

where $f_q(x_1)dx_1$ is the probability of finding a quark with $p_1 = x_1P_1$ and $f_{\bar{q}(x_2)dx_2}$ is the probability of finding an antiquark with $p_2 = x_2P_2$. The parton densities are not calculable within perturbative QCD and must be determined by experiments such as deep inelastic

scattering. The masses of partons are neglected since they are much smaller than the lepton pair invariant mass.

Now we would need to calculate the $q\bar{q} \rightarrow l^+l^-$ cross section. The partonic cross section for the Born process $d\sigma$ is given by the squared matrix element, summed over all incoming and outgoing spins, polarization and colors, multiplied by the phase space of the final state particles and divided by the flux factor. Integrating over the phase space and calculating the matrix element from relevant Feynman diagrams, the final result would be [38],

$$\frac{d\hat{\sigma}}{dM^2} = \frac{4\pi\alpha^2}{9M^2s} M_f^2 \delta(1 - M^2/s), \tag{4–3}$$

where the delta function comes from phase space and M^2 and s are respectively the pair mass squared and the square of the center of mass of the initial hadrons. It can be shown that,

$$M^2 = x_1 x_2 s \tag{4–4}$$

and hence it is convenient to define,

$$\tau = x_1 x_2 = \frac{M^2}{s} \tag{4–5}$$

The rapidity of the lepton pair in terms of parton momentum fraction is given by,

$$y = \frac{1}{2} \ln(\frac{x_1}{x_2}) \tag{4–6}$$

Putting everything together, the double differential cross section becomes,

$$\frac{d^2\sigma}{dM^2 dy} = \frac{4\pi\alpha^2}{9M^4} [\sum_q M_q^2 x_1 f_q(x_1) x_2 f_{\bar{q}}(x_2)] \tag{4–7}$$

summing over all quark distributions and flavors, which only depends upon the parton and antiparton distributions. Integrating over y, we can see that right hand side is only a function of τ [2, 39],

$$M^4 \frac{d^2\sigma}{dM^2 dy} = F(\tau) \tag{4–8}$$

So in the parton model, the cross section depends only on the scaling variable $\tau = \frac{Q^2}{s}$. The rapid fall of cross section as seen in Figure 4-2 is due to the propagator of the virtual photon in the amplitude, which leads to a factor M^4 in the cross section. and also due to the rapid fall of distribution functions $f_q(x)$ as $x \to 1$.

After the advent of QCD, this basic physical picture of Drell-Yan process in terms of parton model has been confirmed theoretically and the details have been greatly improved. At high energies, the $q\bar{q} \to \gamma^* \to l^+l^-$ contribution in Figure DY must be supplemented the additional contribution from $q\bar{q} \to \gamma^* g$ and $qg \to \gamma^* q$ as in Figure 4-4 [40, 41].

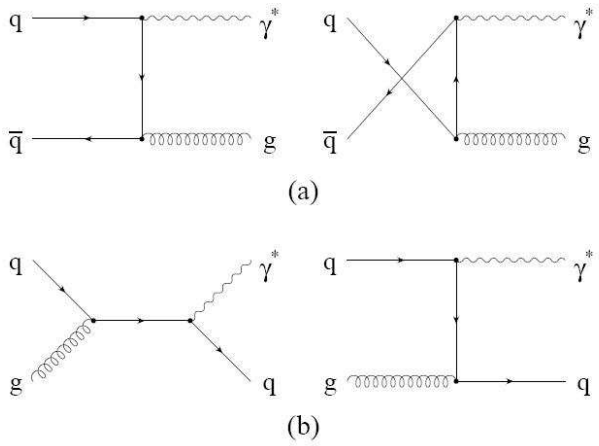

Figure 4-4. QCD diagrams for the Drell-Yan (a) Leading order diagrams for quark-antiquark annihilation subprocess (b) Leading order diagrams for Compton subprocess

The QCD corrections [2] result in logarithmic corrections in Q^2 which can be absorbed in Q^2-dependent quark and antiquark distribution function of the hadrons. Analytic continuation from space-like q^2 (deep inelastic scattering) to time-like q^2 (lepton pair production) and the difference in kinematics between the two processes produce a non

leading finite correction with a very large coefficient, termed the K factor. Also the recoil of quarks or gluons can produce a large transverse momenta of the lepton pair.

At $M \sim M_Z$ additional contribution from s channel Z exchange must be taken into consideration. Data from CDF collaboration for lepton pair production in $p\bar{p}$ production at $\sqrt{s} = 1.8$ TeV has shown appearance of a Z peak at $M \sim M_Z$ [42]. In practice, lepton pair production with $M \sim M_Z$ is analyzed in terms of the production cross section for Z bosons ($q\bar{q} \rightarrow Z$), multiplied by the branching ratio for decay into leptonic final states ($Z \rightarrow l^+l^-$). Single Z bosons are produced with large p_T via the ordinary QCD subprocesses $qg \rightarrow Zq$, $q\bar{q} \rightarrow Zg$, $q\bar{g} \rightarrow Z\bar{q}$. They generate additional gluons via bremsstrahlung resulting in multiparton final states fragmenting into hadrons and forming away-side jets. as in Fig 4-5.

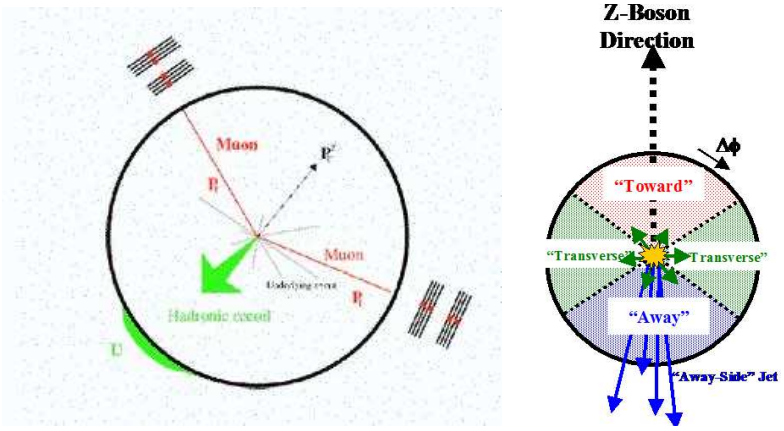

Figure 4-5. Illustration of the recoil from the Z-boson production and formation of awayside jet

4.3 Experimental Studies with the Drell-Yan

The simple Drell-Yan model predictions are about the lepton pairs produced in hadronic collisions and not about the accompanying hadrons, so it has been sufficient to detect solely leptons in order to make many tests of the model. It was the first time that a hadron-hadron cross section could be calculated from first principles. The simplest test of the theory was the verification of the scaling behavior of the cross section only on

the variable, $\tau = \frac{Q^2}{s}$, which was shown by both proton and pion data [37]. These data also showed that logarithmic violation of scaling data was not very significant. The good agreement between the theoretical predictions and measured Drell-Yan cross sections, as seen in Table 4-1 provided confirmation of this parton model approach. The QCD improved version of the parton model has been confirmed by the experiments carried over the years.

Table 4-1. Drell-Yan cross sections

CDF (pb)[43]	NNLO theory (pb)[44]
$254.9 \pm 3.3(stat) \pm 4.6(sys) \pm 15.2(lum)$	252.3 ± 5.0

Most of the important hard scattering processes have been calculated to next to leading order (NLO) in perturbation theory - while the Drell-Yan process itself has been calculated to next to next leading order (NNLO). As a result it has been an important theoretical tool to explore different aspects such as infrared divergences and collinear divergences leading to the factorization theorem in QCD. The process is so well understood theoretically that it has become a tool for precision measurements, as exemplified by discovery and measurement of W and Z. By measuring the distribution in rapidity and mass of the lepton pair one can in principle directly measure the quark and antiquark distribution function of colliding hadrons. For lepton pair production above the Z mass the electroweak interference is important and the forward backward asymmetries can be an effective tool to find Z' bosons if they exist [45].

However, there are a few sources of background which come to dominate the dilepton continuum at low dilepton mass such as dilepton decays of the closely spaced (neutral) vector mesons and Bethe-Heitler pairs [46]. Also the accidental coincidences of leptonic decays such as $\pi^+ \rightarrow \mu^+ + \nu_{mu}$ between two hadrons produced in any hadronic interaction can act as a background. At low mass it is therefore difficult to extract the Drell-Yan signal from background and generally data on dileptons with masses above at least 2 GeV/c^2 are used.

4.4 Drell-Yan Process and the Underlying Event

Let us compare the underlying events in a hard scattering as described in Section 3.3 with underlying events in Drell-Yan process. We can see that we have the outgoing lepton antilepton pair in the final state and there would be no colored final state radiation. The underlying event is defined analogously, as everything except the hard scattered components.

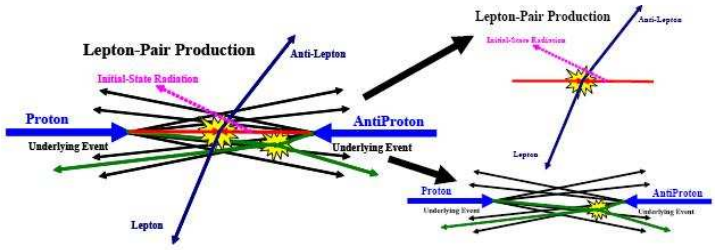

Figure 4-6. Underlying event in Drell-Yan production - everything except the final state lepton-antilepton pair and initial state radiation

By looking at the diagram we can see that essentially everything other than the final lepton antilepton pair is the underlying event. In high p_T Drell-Yan, we can have two leptons on the same side, balanced by a jet on the other side, as in Figure 4-5.

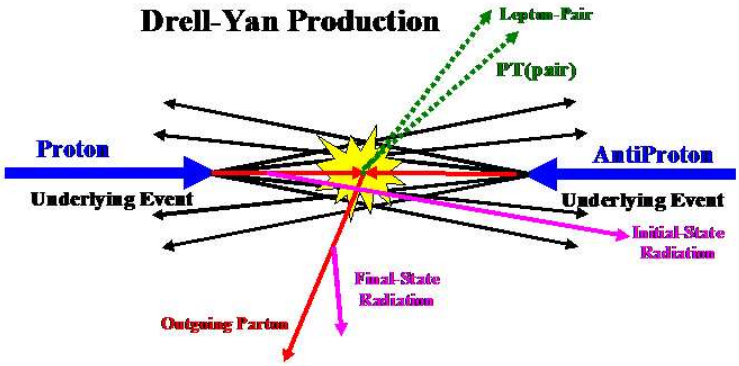

Figure 4-7. Drell-Yan production with high transverse momentum, with two leptons are on the same side

For Drell-Yan its easy to identify and remove leptons (since they are the colorless components) from the transverse and toward (which can not be done for dijet events, as the leading jet is itself in toward region) regions and use them to study the underlying

event. So we can see not only Drell-Yan events are a clean probe of the underlying events but also we can study the underlying event as a function of lepton pair transverse momentum or invariant mass. Comparing them with high p_T jet production would help us to learn more about underlying events in general. And at the same time we would be able to look at Z boson p_T distribution, which would an extra way to constrain our underlying event model. We conclude this chapter by showing a CDF detector view of a Drell-Yan event happening at real time.

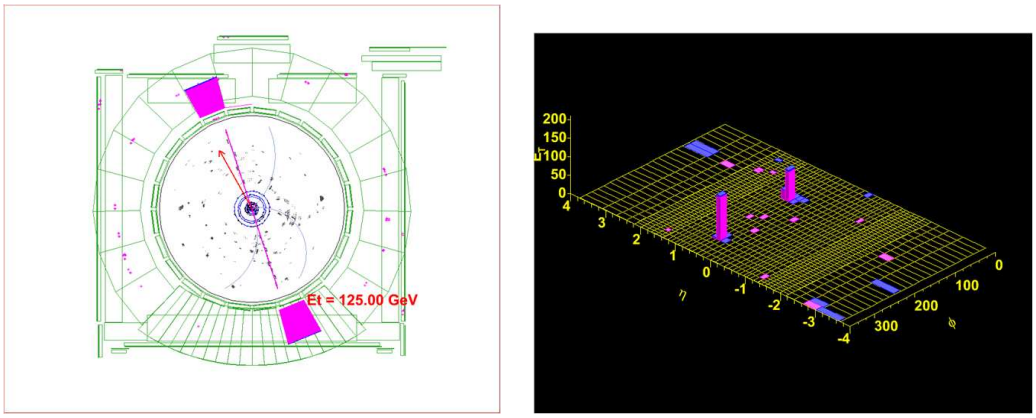

Figure 4-8. Event display of a Drell-Yan process. COT view on left, while EM calorimeter view on right. Figures courtesy CDF.

CHAPTER 5
MONTE CARLO EVENT GENERATORS

5.1 Overview

Monte Carlo methods are a class of computational algorithms used to simulate the behavior of different physical and mathematical systems [47]. As opposed to deterministic simulation methods, they use random numbers (pseudo-random numbers, in practice) and hence are stochastic. It is useful in many interesting calculations, such as determining the cross section for a scattering process have too many degrees of freedom for direct numerical integration. Monte Carlo calculates these integrals by generating a random sample of configurations and averaging the integrand, *i.e.*, by generating a random sample of 'real' events and averaging their weights. As the method is based on random chance, it was named after a gambling resort.

In order to find new physics at a hadron hadron collider it is essential to understand and model the ordinary QCD events well. To do this one must not only have a good model of the hard scattering part of the process, but also of underlying event. However many aspects of nonperturbative QCD physics, like hadronization and multiple interactions, cannot be derived from first principles. The only tool that we have in our disposal for these studies is a cross-comparison of the data and various Monte Carlo generators. By adjusting many parameters that represent a true uncertainty in our understanding of nature in these Monte Carlo generators, we try to match the simulation to the data in the best possible way in order to gain deeper insights into the relative importance if the various contributing sub-processes.

An event generator is also helpful in giving a feel for expected real data, leading to improvement detector design and analysis strategies. Also Monte Carlo can be used as a method for estimating detector acceptance corrections that have to be applied to raw data, in order to extract the true physics signal.

5.2 Event Generation

These programs are intended to generate complete events in as much detail as experimentally observable ones, by subdividing the task into simpler steps. Following is the evolution of a high energy collider event in physical time order, shown also in Figure 5-1 [53].

1. Starts off by two particles coming toward each other and one radiated particle from each of the incoming particle starts off a sequence of branchings, which build up an initial-state shower.

2. One incoming parton from each of the two showers participate in the hard process, which determines the main characteristics of the event where a number of outgoing partons are produced, usually two.

3. The hard process may produce a set of short-lived resonances, like the Z^0 or W gauge bosons, whose decay to normal partons has to be considered in close association with the hard process itself.

4. The outgoing partons usually branch, analogously to the incoming ones, to build up final-state showers.

5. In addition to the hard process considered above, there can be further semihard interactions between the other partons of two incoming hadrons, termed multiple parton-parton interaction.

6. After the particle participating in the hard scattering process is taken out of a beam particle, a beam remnant is left behind. This remnant may have a net color charge that relates it to the rest of the final state.

(5) and (6) mostly constitute the underlying event.

7. The QCD confinement mechanism ensures that the outgoing quarks and gluons are not observable, but instead hadronize to color neutral hadrons.

8. Many of the produced hadrons are unstable and can decay further.

However the data coming from a real experiment also interacts with a complex detector system. The behavior of the detectors how particles produced by the event generator traverse the detector, spiral in magnetic fields, shower in calorimeters, or sneak out through cracks, etc., which all affect the distributions produced, is simulated in

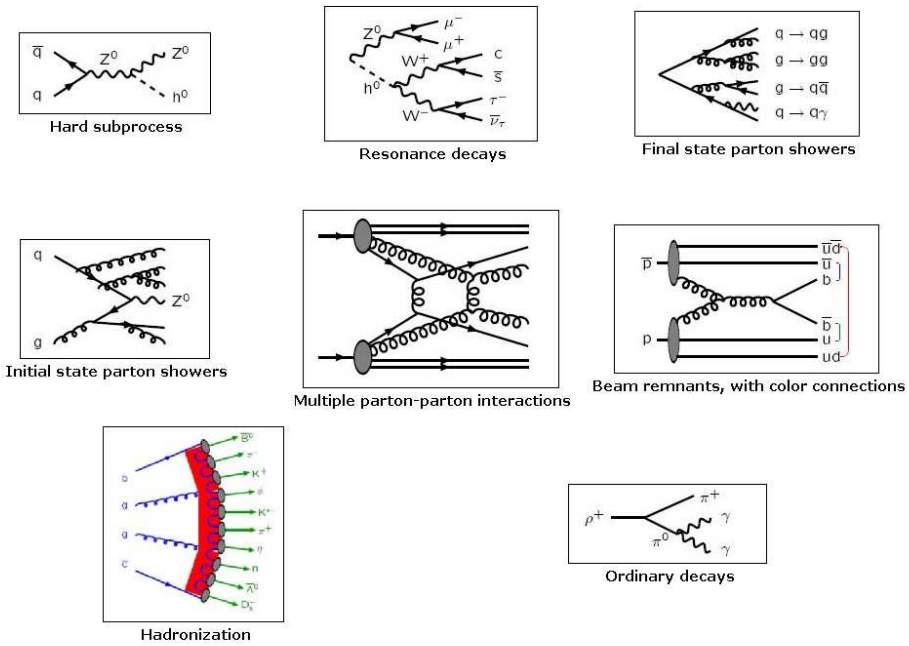

Figure 5-1. Structure of the basic event generation process

programs such as Geant [48]. The CDF detector simulation package, CDFSIM is based on similar programs.

5.3 Examples of Event Generators: PYTHIA and HERWIG

PYTHIA [49] and HERWIG [50] are two of the most popular Monte Carlo event generators for high energy physics. They contain theory and models for all the steps described above. They are largely based on original research, but also borrow many formulae and other knowledge from the literature.

Since this analysis mainly uses PYTHIA, we will focus mostly on it. PYTHIA contains rich selection of around 240 different hard processes, classified according to the number of final-state objects. The bulk of the processes are of the 2-to-2 type, which is not a major limitation, since showers add the required extra activity. In every process that contains colored and/or charged objects in the initial or final state, gluon and/or photon radiation may give large corrections to the overall event. Two traditional approaches

exist to the modeling of perturbative corrections. One is the matrix-element method, in which Feynman diagrams are calculated, order by order. In principle, this is the correct approach, which takes into account exact kinematics, and the full interference and helicity structure, however, these calculations become increasingly difficult in higher orders, in particular for the loop graphs. The second possible approach is the parton-shower one. Here an arbitrary number of branchings of one parton into two (or more) may be combined, to yield a description of the events, with no explicit upper limit on the number of partons involved. In practice, shower programs may be matched to first-order matrix elements to describe the hard-gluon emission region reasonably well, and the two approaches are complementary in many respects. However, because of its simplicity and flexibility, the parton-shower option is generally the first choice.

Hadronization process has yet to be understood from first principles, starting from the QCD Lagrangian. This has left the way clear for the development of a number of different phenomenological models. The 'Lund String Fragmentation Model' [51] is implemented in PYTHIA. The assumption of linear confinement provides the starting point for the string model. As the q and $\overline{q}$ partons move apart from their common production vertex, the physical picture is that of a color flux tube, of the transverse dimensions of the tube are of typical hadronic sizes, being stretched between the q and the $\overline{q}$. To preserve Lorentz covariant, this can be represented by a massless relativistic string with no transverse degrees of freedom. As the q and $\overline{q}$ move apart, the potential energy stored in the string increases, and the string may break by the production of a new $q'\overline{q}'$ pair, so that the system splits into two color-singlet systems $q\overline{q}'$ and $q'\overline{q}$. If the invariant mass of either of these string pieces is large enough, further breaks may occur and this continues until only on-mass-shell hadrons remain, each hadron corresponding to a small piece of string with a quark in one end and an antiquark in the other. HERWIG employs 'Cluster Hadronization Model' [52].

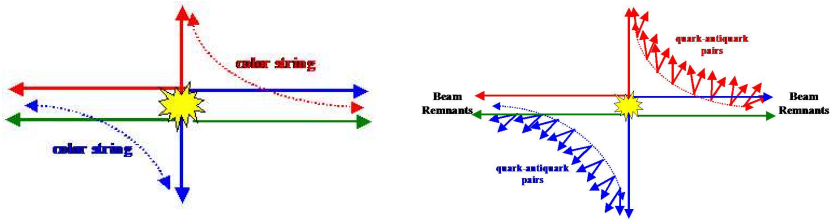

Figure 5-2. At small distances the color forces are weak and the outgoing partons move away from the beam-beam remnants and at large distances the color forces become strong and quark-antiquark pairs are pulled out of the vacuum and hadrons are formed.

In a hadronic collision, the colliding parton only takes some fraction of the total beam energy, leaving behind a beam remnant which takes the rest. For a proton beam, a u quark colliding would leave behind a ud diquark beam remnant, with an antitriplet color charge. The remnant is therefore color-connected to the hard interaction, and forms part of the same fragmenting system. Often the remnant is more complicated, *e.g.* a gluon participating in the hard scattering would leave behind a uud proton remnant system in a color octet state, which can conveniently be subdivided into a color triplet quark and a color antitriplet diquark, each of which are color-connected to the hard interaction. The energy sharing between these two remnant objects, and their relative transverse momentum, introduces additional degrees of freedom, which are not understood from first principles. Also to take into account the motion of quarks inside the original hadron, as required by the uncertainty principle by the proton size a primordial transverse momentum is assigned to the colliding parton. This primordial k_T is selected according to some suitable distribution, and the recoil is assumed to be taken up by the beam remnant.

Each of the beam particles contains a number of partons, and so the probability for several interactions in one and the same event is not be negligible. In principle these additional interactions could arise because one single parton from one beam scatters against several different partons from the other beam, or because several partons from each beam take place in separate 2-to-2 scatterings. Both are expected, but combinatorics

favors the latter, which is the mechanism considered in PYTHIA. The understanding of multiple interaction is still very primitive. PYTHIA therefore contains several different options of adjusting the multiple parton interaction.

PYTHIA models the soft component of the underlying event with color string fragmentation, but in addition includes a contribution arising from multiple parton interactions (MPI). HERWIG by itself does not have multiple parton interaction.

5.4 Tuning PYTHIA

PYTHIA contains parameters to control each of the subprocesses described above. A complete list of them can be found in PYTHIA manual [53] - here we would point out the some of the relevant ones describing the underlying event in Table 5-1. Technically, PYTHIA parameters can be varied independently of each other, but the physical requirement of a sensible description of a set of data leads to correlations and anticorrelations between the parameters. Hence we need to produce tunes, not of one parameter at a time, but simultaneously for a group of them. Given the many PYTHIA parameters to be tuned, it is convenient to divide the task into subtasks. Firstly, if we assume jet universality, hadronization and final-state parton showers should be tuned to e^+e^- annihilation data, notably from LEP1 (The Large Electron-Positron collider, formerly at CERN) since this offers the cleanest environment. Secondly, with such parameters fixed, hadron collider data should be studied to pin down multiple interactions and other further aspects, such as initial-state radiation. We will focus on PYTHIA tunes which are relevant to underlying event studies.

PYTHIA tune A was determined by fitting the CDF Run 1 underlying event data [54], by mostly adjusting multiple parton interaction. Figure 5-3 shows that PYTHIA tune A does not fit the CDF Run 1 Z-boson p_T distribution [55], since at that time the Z boson data was not considered. PYTHIA tune AW, mostly by adjusting the initial state radiation fits the Z-boson p_T distribution as well as the underlying event at the Tevatron.

Table 5-1. Some of the PYTHIA parameters describing the underlying event

Parameter	Definition
MSTP(81)	MPI on/off
MSTP(82)	3 / 4: respectively - denoting single or double gaussian hadronic matter distribution in the p / $\overline{p}$
PARP(62)	Effective Q cut-off, below which space-like showers are not evolved
PARP(67)	ISR maximum scale factor
PARP(82)	MPI p_T cut-off
PARP(83)	Warm-Core: parp(83)% of matter in radius parp(84)
PARP(84)	Warm-Core: parp(83)% of matter in radius parp(84)
PARP(85)	Probability that an additional interaction in the MPI formalism gives two gluons, with color connections to nearest-neighbor in momentum space
PARP(86)	Probability that an additional interaction in the MPI formalism gives two gluons, either as described in PARP(85) or as a closed gluon loop. Remaining fraction is supposed to consist of q$\overline{q}$ pairs.
PARP(89)	Reference energy scale
PARP(90)	Energy rescaling term for PARP(81-82) $\sim E_{CM} \wedge PARP(90)$

The values of the relevant parameters[1] for tune AW was determined by CDF Electroweak Group (the 'W' stands for Willis Sakumoto, one of the main contributors) [56]. Both plots in Figure 5-3 reveal a remarkably good agreement of the data and PYTHIA, which, however, was achieved only after tuning a number of Monte Carlo generator parameters, as follows.

- The initial state radiation had to be significantly intensified.
- The dependence of the probability of multi-parton (secondary) interactions on the impact parameter had to be smoothed out.
- The probability of di-gluon production in multi-parton secondary interactions had to be substantially enhanced over di-quark production.
- The probability of color connections of products of secondary interactions with pp-remnants had to be increased.

[1] PARP(62), PARP(64), and PARP(91).

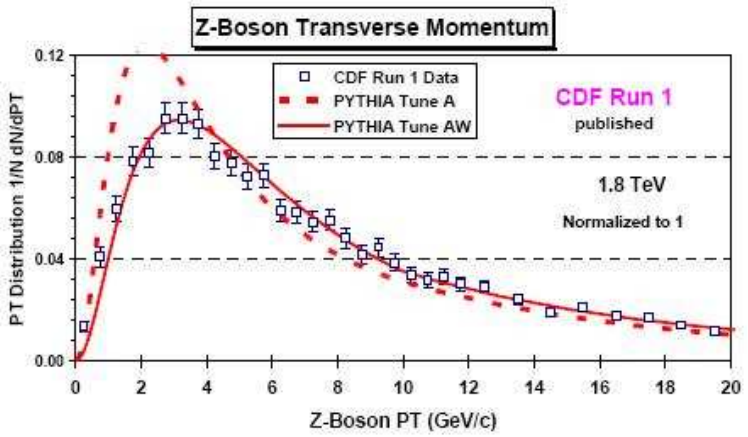

Figure 5-3. Z-boson p_T distribution from Run 1 and PYTHIA tune A and AW predictions

This exercise shows that PYTHIA can be brought into a good agreement with data, with proper tuning [57]. For 'leading jet' production Tune A and Tune AW are nearly identical.

We will conclude this section by briefly mentioning some of the PYTHIA Run 2 tunes [58]. Table 5.1 shows the parameters for several PYTHIA 6.2 tunes. PYTHIA Tune DW is very similar to tune A except that it also fits the CDF Run 1 Z-boson p_T distribution which tune A does not fit. Tune DW has the DØ preferred value of the parameter[2] setting the high p_T scale for initial-state radiation, determined by fitting their dijet $\Delta\phi$ distribution [59]. Tune DW and tune DWT are identical at 1.96 TeV, but tune DW and DWT extrapolate differently to the LHC. Tune DWT uses the ATLAS energy dependence, while tune DW uses the tune A value [3] . All the tunes use the CTEQ5L structure functions [60]. The first 9 parameters in Table 3.1 tune the multiple parton interactions (MPI). PARP(62), PARP(62), and PARP(62) tune the initial-state radiation

[2] PARP(67) = 2.5, PARP(67) sets the high p_T scale for initial-state radiation in PYTHIA. It determines the maximal parton virtuality allowed in time-like showers.

[3] Tune DWT uses the ATLAS energy dependence, PARP(90) = 0.16, while tune DW uses the tune A value of PARP(90) =0.25.

and the last three parameters set the intrinsic k_T of the partons within the incoming proton and antiproton.

Table 5-2. Parameters for several PYTHIA 6.2 tunes. Tune A is a CDF Run 1 'underlying event' tune. Tune AW and DW are CDF Run 2 tunes which fit the existing Run 2 'underlying event' data and fit the Run 1 Z-boson p_T distribution. The ATLAS tune is the default tune currently used by ATLAS at the LHC. Tune DWT use the ATLAS energy dependence for the MPI, PARP(90). The first 9 parameters tune the multiple parton interactions. PARP(62), PARP(62), and PARP(62) tune the initial-state radiation and the last three parameters set the intrinsic k_T of the partons within the incoming proton and antiproton.

Parameter	Tune A	Tune AW	Tune DW	Tune DWT	ATLAS
PDF	CTEQ5L	CTEQ5L	CTEQ5L	CTEQ5L	CTEQ5L
MSTP(81)	1	1	1	1	1
MSTP(82)	4	4	4	4	4
PARP(82)	2.0	2.0	1.9	1.9409	1.8
PARP(83)	0.5	0.5	0.5	0.5	0.5
PARP(84)	0.4	0.4	0.4	0.4	0.5
PARP(85)	0.9	0.9	1.0	1.0	0.33
PARP(86)	0.95	0.95	1.0	1.0	0.66
PARP(89)	1800	1800	1800	1960	1000
PARP(90)	0.25	0.25	0.25	0.16	0.16
PARP(62)	1.0	1.25	1.25	1.25	1.0
PARP(64)	1.0	0.2	0.2	0.2	1.0
PARP(67)	4.0	4.0	2.5	2.5	1.0
MSTP(91)	1	1	1	1	1
PARP(91)	1.0	2.1	2.1	2.1	1.0
PARP(93)	5.0	15.0	15.0	15.0	5.0

Table 5-3. Computed value of the multiple parton scattering cross section for the various PYTHIA 6.2 tunes

Tune	σ(MPI) at 1.96 TeV	σ(MPI) at 14 TeV
A, AW	309.7 mb	484.0 mb
DW	351.7 mb	549.2 mb
DWT	351.7 mb	829.1 mb
ATLAS	324.5 mb	768.0 mb

Table 5.2 shows the computed value of the multiple parton scattering cross section for the various tunes. The multiple parton scattering cross section (divided by the total inelastic cross section) determines the average number of multiple parton collisions per event.

JIMMY is a multiple parton interaction model which can be added to HERWIG to improve agreement with the underlying event observables. To compare with the Z-boson data, a HERWIG (with JIMMY MPI) tune with have been constructed with $JMUEO = 1$, $PTJIM = 3.6$ GeV/c, $JMRAD(73) = 1.8$, and $JMRAD(91) = 1.8$.

PYTHIA tune A, tune DW, and the ATLAS PYTHIA tune predict about the same density of charged particles in the transverse region for leading jet events at the Tevatron. However, the ATLAS tune has a much softer p_T distribution of charged particles resulting in a much smaller average p_T per particles, not agreeing with CDF data [61]. HERWIG does a fairly good job fitting the Z-boson p_T distribution without additional tuning, but does not fit the CDF underlying event data.

Minimum bias collisions are a mixture of hard processes (perturbative QCD) and soft processes (non-perturbative QCD) and are, hence, very difficult to simulate. Min-bias collisions contain soft 'beam-beam remnants', hard QCD 2-to-2 parton-parton scattering, and multiple parton interactions (soft and hard). To correctly simulate min-bias collisions one must have the correct mixture of hard and soft processes together with a good model of the multiple-parton interactions. The first model that even came close to correctly modeling min-bias collisions at CDF is PYTHIA tune A. Tune A was not tuned to fit min-bias collisions. It was tuned to fit the activity in the 'underlying event' in high transverse momentum jet production. However, PYTHIA uses the same p_T cut-off for the primary hard 2-to-2 parton-parton scattering and for additional multiply parton interactions. Hence, fixing the amount of multiple parton interactions (*i.e.* setting the p_T cut-off) allows one to run the hard 2-to-2 parton-parton scattering all the way down to $p_T(\text{hard}) = 0$ without hitting a divergence. For PYTHIA the amount of hard scattering in min-bias is, therefore, related to the activity of the 'underlying event' in hard scattering processes. Neither HERWIG (without MPI) or HERWIG (with JIMMY MPI) can be used to describe min-bias events since they diverge as $p_T(\text{hard})$ goes to zero.

CHAPTER 6
ANALYSIS STRATEGY

6.1 Introduction: Goal

We have seen how the underlying event is an important element of the hadronic collider environment. The goal of this analysis is to study the behavior of the charged particle ($p_T > 0.5$ GeV/c, $|\eta| < 1$) components of the underlying event associated with Drell-Yan production in hard scattering proton-antiproton collisions at 1.96 TeV at CDF and produce data on the underlying event that is corrected to the particle level[1] so that it can be used to tune the QCD Monte Carlo models without requiring a simulation of the CDF detector. We would be able to compare our results with similar analyses done with the Tevatron jet data and at the LHC by the Florida group [62]. Also by looking at the measurements sensitive to the underlying event, we would be able to better constrain our underlying event models.

6.2 Data Selection

Z-bosons are mainly identified through their leptonic decays. These decays are characterized by two high transverse energy leptons (we look at electrons and muons, since τ decays into charged particles traveling in same direction, similar to jets).

We analyzed the high p_T electron and muon data, corresponding to the luminosity[2] of approximately 2.7 fb^{-1} and corresponding PYTHIA tune AW [56] samples, taken between February 2002 and April 2008, as shown in Table 1[3] .

[1] The final state stable particles in Monte Carlo generators refer to colorless particles having a lifetime greater than approximately 10^{-11} s.

[2] Corresponding to run period 17, with events are required to be on the goodrun list, version 23.

[3] CDF Drell-Yan PYTHIA tune AW samples: ze0s, ze1s, CDF high-p_T central electrons: bhel, CDF high-p_T CMUP and CMX muons: bhmu.

Table 6-1. Data and Monte-Carlo samples used in this analysis

Lepton	Monte Carlo	Data
Electron	Drell-Yan Z/gamma* $\rightarrow ee$ sample	High-p_T central electrons
Muon	Drell-Yan Z/gamma* $\rightarrow \mu\mu$ sample	High-p_T CMUP and CMX muons

6.3 Event Selection

We pick only those events having one and only quality 12 vertex[4] within $|z_0| < 60$ cm. It measures the distance of the $p\overline{p}$ collision event vertex from the center of the detector in z direction. To ensure that a track for each charged particle is well measured by the tracking system, we need this requirement.

6.4 Electron Selection

Electrons are identified by matching high momentum tracks to high energy clusters in central electromagnetic calorimeter (CEM), with further requirements as described next. The following variables are used to reconstruct the electron accurately.

- **Track z_0** . Distance of where the electron track extrapolates to beamline from the center of the detector in z direction. To ensure that track for each electron is well extrapolated to the calorimeter and drift chamber, we need $|z_{vertex}|$ to be less than 60 cm. This requirement helps to ensure that the particle passes through a significant portion of the detector so that we can obtain enough information about the event.

- $\boldsymbol{E_T}$. Value of electromagnetic transverse energy, (transverse to the beamline).

- **Track p_T** . Specifies the value of the transverse momentum of the associated track, (transverse to the beamline).

- **Track d_0** . The transverse impact parameter, defined as the minimum distance between the electron track and the primary vertex in the plane transverse to the beam direction - small value means the particle originates from near the interaction region.

- $\boldsymbol{\Delta z = |z - z_{Q12}|}$. The measured longitudinal distance between the measured track or particle and the primary quality 12 vertex.

[4] The vertex quality is quantified by the fit χ^2. In general, the higher the vertex quality, the larger the number of tracks composing that vertex. Quality 12 offers a good trade off between between fake rate and efficiency.

- $\boldsymbol{L_{Shr}}$. This is the maximum value of the transverse shower profile of the cluster. It compares the lateral sharing of energy in the calorimeter towers of an electron cluster to electron shower shapes from a test beam data.

- **CES strip** $\boldsymbol{\chi^2}$. This is the average scaled χ squared of the best matching strip clusters. It quantifies the comparison of the calorimeter pulse height to the test beam data for each of the 11 strips per CEM chamber in z.

- **Charge**. Specifies the charge - it is calculated using the curvature of he associated track. A negative curvature indicates a negative charge, which would be expected for an electron and a positive curvature an positive value of the charge, for a positron.

- $\boldsymbol{E_{HAD}/E_{EM}}$. Calculated as a ratio of the total Hadronic energy in the cluster and the total EM energy. Three hadronic towers means using the whole cluster. The good electrons are expected to deposit most of its energy in EM calorimeter. The CEM shower characteristics should be consistent with that of a single charged particle, not a jet faking an electron.

- **Isolation**. This is the total transverse isolation energy in cone of $\Delta R = \sqrt{\Delta\phi^2 + \Delta\eta^2} = 0.4$ as taken from the EM cluster, divided by EM transverse energy of the cluster. It is used for distinguishing between an isolated particle and a particle in a jet.

- **CES** $\boldsymbol{\Delta Z}$. Absolute value of the difference between the z coordinate of the cluster at the CES plane and the z coordinate of the track extrapolated to the CES.

- **CES** $\boldsymbol{\Delta X}$. Difference between the x coordinate of the cluster at the CES plane and the x coordinate of the track.

- $\boldsymbol{E/p}$. Ratio of the electromagnetic energy and p is the momentum of the associated track. A small E/p distinguishes electrons from heavier mesons such as pions depositing energy in the calorimeter. In order that the momentum resolution does not make for inefficiencies for very high-energy electrons, for $E_T > 100$ GeV the E/p cut is not applied.

- **CES fiducial**. Fiduciality is a variable, which can have values corresponding to which part of the detector is being used. A value of 1 corresponds to central and plug region, where the calorimeter is known to function well.

- **COT axial and stereo hits**. As described in Chapter 2.4.2, COT consists of 8 alternating superlayers of 4 stereo and 4 axial wire planes, with 12 measurements per SL. we fit the tracks by linking segments with hits, and a minimum number of segments (satisfying minimum number of hits) are required to properly fit the track.

The electron selections are based on the standard CDF high p_T electron selection criteria [63, 64], with tight and loose cuts described in Table 6-2. The tight and loose cuts are similar till the last four variables in the table, *i.e.* loose electrons are tight electrons without the L_{Shr}, E/p, signed CES ΔX, CES ΔZ and CES strip χ^2 cuts.

Table 6-2. Electron selection

Variable	Loose	Tight
Region	CEM	CEM
CES fiducial	1	1
E_T	$\geq$ 20 GeV	$\geq$ 20 GeV
Track z_0	$\leq$ 60 cm	$\leq$ 60 cm
Track p_T	$\geq$ 10 GeV/c	$\geq$ 10 GeV/c
COT axial	3 Axial SLs with 5 hits/SL	3 Axial SLs with 5 hits/SL
COT stereo	2 Stereo SLs with 5 hits/SL	2 Stereo SLs with 5 hits/SL
Isolation(R=0.4)/E_T (with leakage correction)	≤ 0.1	≤ 0.1
E_{Had}/E_{EM} (3 towers)	$\leq (0.055 + (0.00045 \times E))$	$\leq (0.055 + (0.00045 \times E))$
L_{Shr} (3 towers, track)	...	≤ 0.2
E/p	...	$\leq$ 2.0 (unless $p_T \geq$ 50 GeV/c)
CES ΔZ	...	$\leq$ 3.0 cm
Signed CES ΔX	...	$-3.0 \leq q \times \Delta X \leq 1.5$
CES strip χ^2 (scaled with E)	...	$\leq$ 10.0

Photon conversions, via pair production occur throughout the detector material and are a major source of electrons and positrons that pass the above selection criteria. They are identified by the characteristic small opening angle between two oppositely charged tracks that are parallel at their distance of closest approach to each other [66]. Electron candidates with an oppositely charged partner track meeting these requirements are rejected.

6.5 Muon Selection

Muons are easily distinguished from other particles produced, since they deposit their energy in muon chambers. Good central muons are identified by extrapolating tracks in the COT through the calorimeters, and the extrapolation is required to match to a 'stub' (which is created when the CMU, CMP or CMX matches several hits in their drift

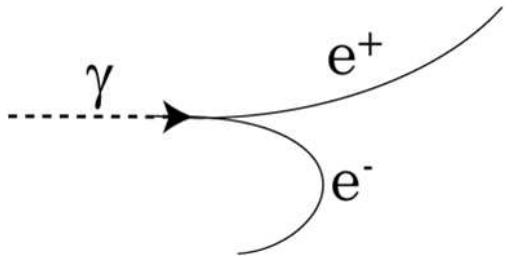

Figure 6-1. Photon conversion into an electron positron pair

chambers) either in both the CMU (Central Muon system) and CMP (Central Muon Upgrade) muon detectors ('CMUP' muon) or in the CMX (Central Muon Extension) system ('CMX' muon). Good central muons are required to have a track-stub matching distance less than 3 cm for CMU, less than 5 cm for CMP, and less than 6 cm for CMX. The variables needed for reconstructing a muon are as follows.

- **Track z_0** . Distance of where the muon track extrapolates to beamline from the center of the detector in z direction. To ensure that track for each muon is well extrapolated to the calorimeter and drift chamber, we need $|z_{vertex}|$ to be less than 60 cm. This requirement helps to insure that the particle passes through a significant portion of the detector so that we can obtain enough information about the event.

- **Track p_T** . Specifies the value of the transverse momentum of the associated track (transverse to the beamline). We place a minimum 20 GeV/c cut on muon momentum in order to remove low energy background muons coming from decays other than Z-bosons [5] .

- **Track d_0** . The transverse impact parameter, defined as the minimum distance between the muon track and the primary vertex in the plane transverse to the beam direction - small value means the particle originates from near the interaction region. It is corrected for the beam position.

- $\Delta z = |z - z_{Q12}|$. This is the measured longitudinal distance between the measured muon track and the primary quality 12 vertex.

[5] Because Z-bosons have a rest energy of approximately 90 GeV we expect the average momentum of muons from this decay to be 45 GeV. Of course, the muons from the decays do not need to carry equal momentum because the Z might have some transverse or longitudinal momentum associated with its own motion, however it is unlikely that unless the Z-boson is produced with a large momentum that one muon of the decay muons would have less than 20 GeV/c.

- **Charge**. Specifies the charge - it is calculated using the curvature of he associated track. A negative curvature indicates a negative charge, which would be expected for a muon and a positive curvature an positive value of the charge for an antimuon.

- $\boldsymbol{E_{HAD}}$ **and** $\boldsymbol{E_{EM}}$. These are the total Hadronic energy in the cluster and the total EM energy. Three hadronic towers means using the whole cluster. Since muons do not interact often when passing through materials, they do not deposit much energy in the calorimeters. This is an energy dependent phenomenon and for muons with $p_T \geq 100$ GeV radiation becomes more prominent and hence they deposit more energy.

- **Isolation fraction**. This is the total transverse isolation energy in cone of radius $\Delta R = \sqrt{\Delta\phi^2 + \Delta\eta^2} = 0.4$ around the track, excluding the energy matched to the track itself. It is a measure of how much a particle pair produces and radiates. Muons should have small values for isolation because they are penetrating particles. It is scaled by the p_T of the track to account for energy dependent radiation and interaction. It is used for distinguishing between an isolated particle and a particle in a jet.

- $\boldsymbol{\rho_{COT}}$. This is the radius of the track at the point where it crosses the z planes at the end of the COT. $\rho_{COT} = z_{COT} - z_0/\lambda$, where z_0 is the track z coordinate at the point of its closest approach to z axis, $\lambda = \cot\theta$, $z_{COT} = 155$ cm if $\lambda > 0$ and $z_{COT} = -155$ cm if $\lambda < 0$. Requiring $\rho_{COT} > 140$ cm is approximately equivalent to requiring that the track pass through all 8 SL's of COT and well measured.

- **Track** $\boldsymbol{\chi^2}$. The track χ^2 cut is based on the COT of the parent track and it is assumed that the number of degrees of the freedom is 5 less than the number of COT hits.

The muon selections are based on the standard CDF high p_T muon selection criteria [63, 65]. We look at the CMUP and CMX muons, with fiducial cuts[6] in addition to the standard cuts. The selection criteria are given in Table 6-3.

The only extra cut we make is on χ^2/DoF (the track χ^2 cut is based on the COT of the parent track and it is assumed that the number of degrees of the freedom is 5 less than the number of COT hits) - which helps to eliminate cosmic muons. Apart from that, to

[6] Fiducial cuts are applied to avoid cracks between the calorimeter modules.

Table 6-3. Muon selection

Variable	Muon
For all muon types,	
Region	CMUP and CMX
p_T	$\geq$ 20 GeV/c
E_{EM}	$\leq$ 2 GeV + Max(0,(0.0115 $\times$(p-100))
E_{Had}	$\leq$ 6 GeV + Max(0,(0.028 $\times$(p-100))
Isolation (total E_T in R=0.4 around muon)/p_T	$\leq$ 0.1
COT axial	3 Axial SLs with 5 hits/SL
COT stereo	2 Stereo SLs with 5 hits/SL
Track $\lvert z_0 \rvert$	$\leq$ 60 cm
Track $\lvert d_0 \rvert$ (beam corrected)	$\leq$ 0.2 cm
Additionally for CMUP muons,	
$\lvert \Delta X_{CMU} \rvert$	$\leq$ 7 cm
$\lvert \Delta X_{CMP} \rvert$	$\leq$ 5 cm
$X - FID_{CMU}$	$\leq$ 0 cm
$X - FID_{CMP}$	$\leq$ 0 cm
$Z - FID_{CMU}$	≤ -3 cm
$Z - FID_{CMP}$	$\leq$ 0 cm
Additionally for CMX muons,	
$\lvert \Delta X_{CMX} \rvert$	$<$ 6 cm
For run number $>$ 150144,	
$X - FID_{CMX}$	$<$ 0 cm
$Z - FID_{CMX}$	< -3 cm
To remove cosmic muons,	
$\lvert \Delta z \rvert$	$\leq$ 3 cm

get rid of cosmic muons, we also use a 'time of flight' (ToF) cosmic filter [67], which will be described in detail in the next section.

6.6 Lepton Pair Formation

The lepton pairs are formed by oppositely charged leptons, with the requirement that z_0 of the two leptons must pass $|z_0^1 - z_0^2| < 4$ cm, to ensure that both leptons came from the same primary collision. For electrons, we form pairs with at least one tight electron, as defined earlier. For Muons, there is no such distinction. Additionally for rejecting cosmic muons, we implement ToF timing cuts. If both muons have ToF timing, we require the difference of the ToF times between the upper and the lower muon to be less than 5 ns. Timing is a good way to distinguish if two muons came from the interaction point, or one

single muon from a cosmic ray appear to be as two muons. The time difference between the muons recorded in the upper and lower half of the detector, as measured by the 'time of flight' detector is given as,

$$\begin{aligned}\Delta_T &= T_{upper} - T_{lower} \\ &= (L_1 + L_2)/c \\ &\approx 2L_1/c \approx 2L_2/c\end{aligned}$$

where L_1 and L_2 are the distances traveled by the cosmic ray in the upper and the lower half of the detector. For two muons originating at the center of the detector,

$$\begin{aligned}\Delta_T &= T_{upper} - T_{lower} \\ &= (L_1 - L_2)/c \\ &\approx 0\end{aligned}$$

So ideally the muons not coming from the cosmic rays would have very little time difference, and this principle is used to eliminate cosmic ray muons.

The mass range of the lepton pair is divided into 3 regions for this analysis, as shown in Table 6-4. The region of lepton invariant mass between 70 and 110 GeV/c^2, termed the Z-region, is used for this analysis.

Table 6-4. Mass ranges

Mass region	Mass range
Low	Less than 70 GeV/c^2
Z	$70 - 110$ GeV/c^2
High	Above 110 GeV/c^2

One of the other advantages of using Drell-Yan data is that isolated leptons can be identified cleanly over the backgrounds. The $Z \rightarrow e^+e^-$ data samples contains backgrounds mainly from QCD jets, W+jets. Studies [68] have shown that these backgrounds are negligible at the region of Z-boson.

Approximately 65,000 electron and muon pairs each passed our selection criteria and are used in the analysis. We use the same kinematic cuts on both the particle level Monte Carlo and the detector level Monte Carlo and data - we require that,

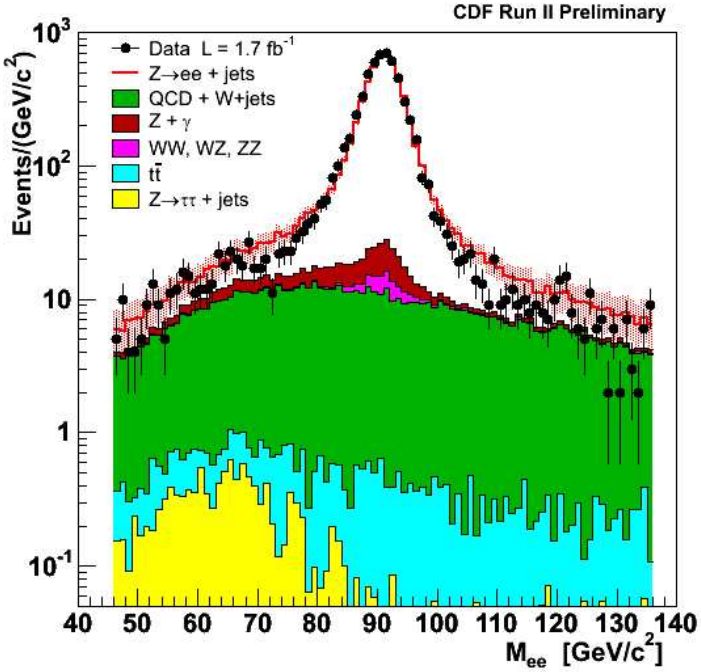

Figure 6-2. Shows that the background at the region of Z-boson is very low

Individual lepton $p_T > 20$ GeV/c,

Individual lepton $|\eta| < 1$, and

Lepton pair $|\eta| < 6$.

6.7 Charged Track Selection

A track is identified by multiple hits in tracking system, by using the following parameters.

- **Track z_0** . Distance of where the track extrapolates to beamline from the center of the detector in z direction. To ensure that each track is well extrapolated to the calorimeter and drift chamber, we need $|z_{vertex}|$ to be less than 60 cm.

- **Track p_T** . Specifies the value of the transverse momentum of the associated track. (transverse to the beamline)

- **Track d_0** . The transverse impact parameter, defined as the minimum distance between the muon track and the primary vertex in the plane transverse to the beam direction - small value means the particle originates from near the interaction region. The tracks are defined to be loose and tight according to this parameter. It is corrected for the beam position.

- $\boldsymbol{\Delta z = |z - z_{Q12}|}$. It is the measured longitudinal distance between the measured muon track and the primary quality 12 vertex.

- **Charge**. Specifies the charge - it is calculated using the curvature of he associated track. A negative curvature indicates a negative charge and positive curvature an positive value of the charge.

Only charged tracks in the region $0.5 < p_T < 150$ GeV/c and $|\eta| < 1$, where efficiency is high are considered. The upper limit of p_T max cut is chosen as 150 GeV/c to prevent mismeasured tracks with very high p_T from contributing to the observables. We also remove conversions from photon by finding the partner track [66], to make sure none of the charged particles are electrons coming from pair production from photon . The track selection criteria is given in Table 6-5.

Table 6-5. Charged track selection

Variable	Loose	Tight
Track region	COT	COT
Track $p_T$min	≥ 0.5 GeV/c	≥ 0.5 GeV/c
Track $p_T$max	≤ 150 GeV/c	≤ 150 GeV/c
Track $\|\eta\|$	≤ 1	≤ 1
Track z_0	< 60 cm	< 60 cm
Track $\|d_0\|$ (beam corrected)	≤ 1 cm	≤ 0.5 cm
Track $\|\Delta z\|$	≤ 3 cm	≤ 2 cm
COT axial	2 Axial SLs with 10 hits/SL	2 Axial SLs with 10 hits/SL
COT stereo	2 Stereo SLs with 10 hits/SL	2 Stereo SLs with 10 hits/SL
Track fit χ^2/DoF	≤ 10	≤ 10

6.8 Observables

The observables that are studied in this analysis are described in table 6-6. Since we will be studying regions in $\eta - \phi$ space with different areas, we will construct densities by dividing by the area. For example, the number density, $dN_{Chg}/d\eta d\phi$ corresponds to the number of charged particles ($p_T > 0.5$ GeV/c) per unit $\eta - \phi$. The $p_T$sum density, dp_Tsum/d$\eta d\phi$, corresponds to the amount of charged particle ($p_T > 0.5$ GeV/c) scalar $p_T$sum per unit $\eta - \phi$.

Table 6-6. Observables examined in this analysis as they are defined at the particle level and the detector level. Charged tracks are considered 'good' if they pass the selection criterion given in Table 6-5. The mean charged particle $\angle p_T\rangle$ is constructed on an event-by-event basis and then averaged over the events. For the average p_T and the $p_T$max we require that there is at least one charge particle present. The $p_T$sum density is taken to be zero if there are no charged particles present.

Observable	Particle level	Detector level
Lepton p_T	p_T of the lepton pair	p_T of the lepton pair, formed by at least one tight lepton
Charged density	Number of charged particles per unit $\eta - \phi$	Number of 'good' charged tracks per unit $\eta - \phi$
p_T sum density	Scalar p_T sum of charged particles per unit $\eta - \phi$	Scalar p_T sum of 'good' charged tracks per unit $\eta - \phi$
$\langle p_T\rangle$	Average p_T of charged particles	Average p_T of 'good' charged tracks
$p_T$max	Maximum p_T of charged particles	Maximum p_T of good charged tracks

The mean charged particle $\langle p_T\rangle$ and the $p_T$max are constructed on an event by event basis. For the average p_T and $p_T$max, we require that there is at least one charged particle present. The $p_T$sum (hence the $p_T$sum density) us taken to be zero if there are no charged particle present.

CHAPTER 7
RESULTS

7.1 Earlier Work

A previous Run 2 underlying event analysis used the MidPoint jet algorithm ($R = 0.7$, $f_{merge} = 0.75$) [69] to define jets and compared the observables corrected back to the particle level with the QCD Monte Carlo models [70]. The the behavior of charged particles ($p_T > 0.5$ GeV/c, $|\eta| < 1$) produced in association with large transverse momentum jets were studied. The models includes PYTHIA tune A and HERWIG.

The events in which there is a leading calorimeter jet (MidPoint $R = 0.7$) in the region $|\eta| < 2$ and there are no restrictions placed on the second and third highest p_T jets (jet#2 and jet#3) are referred to as leading jet events.

The conclusion was that PYTHIA tune A does not have quite enough activity in the transverse region. It however does a much better job than HERWIG, which produces a p_T distribution of charged particles that is too 'soft'. For all the densities (number, p_T sum) PYTHIA tune A is low, but in all the cases it agrees, if we take the transDIF (*i.e.* transMAX−transMIN). This indicates that the excess activity seen in the data over PYTHIA tune A arises from the soft component of the underlying event (*i.e.* beam-beam remnants and/or multiple parton interactions) that contributes equally to both transMAX and transMIN. We would compare our results with the leading jet underlying event results.

7.2 Correcting Data Back to Particle Level

We use the ratio of the generator level Monte Carlo result and the detector Level Monte Carlo result as our correction factor for correcting the data back to the particle level, as that is the effect of the detector.

Our generator level results are formed by adding both electron and muon results together, since in theory level, they are expected to and indeed found to be consistent. We would not show all the correction factors here, but would elucidate our method by showing

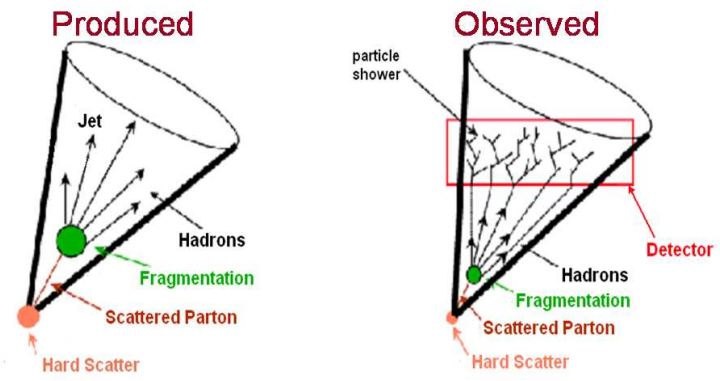

Figure 7-1. Illustration of data at the particle level and at the detector level.

an example for charged particle density in transverse region in Figure 7-2. The rest of the plots are arrived at similarly.

7.3 Systematic Errors

We correct the data back to particle level in three different ways for electrons, and in two different ways for muons. We take the differences at particle level between (1) loose-tight and tight-tight electron selection and (2) loose and tight track cuts for charged particles as systematic uncertainties for electron data. For muon data, the differences between loose and tight track cuts are taken as systematic uncertainties. We add the different systematic errors in quadrature, and add the statistical error with that in quadrature with that to draw one combined error bar. We observed that the differences between different cuts do not produce a significant systematic uncertainty and the dominant contribution to our total uncertainties are statistical. When comparing with the dijet underlying event data later, we would see that they have much smaller statistical (hence overall) uncertainties, as dijet events have more statistics. In Figures 7-3 and 7-4, we show all the systematic differences coming from the different lepton and charged particle selections. We can clearly see that the differences between different cuts do not produce a significant systematic error.

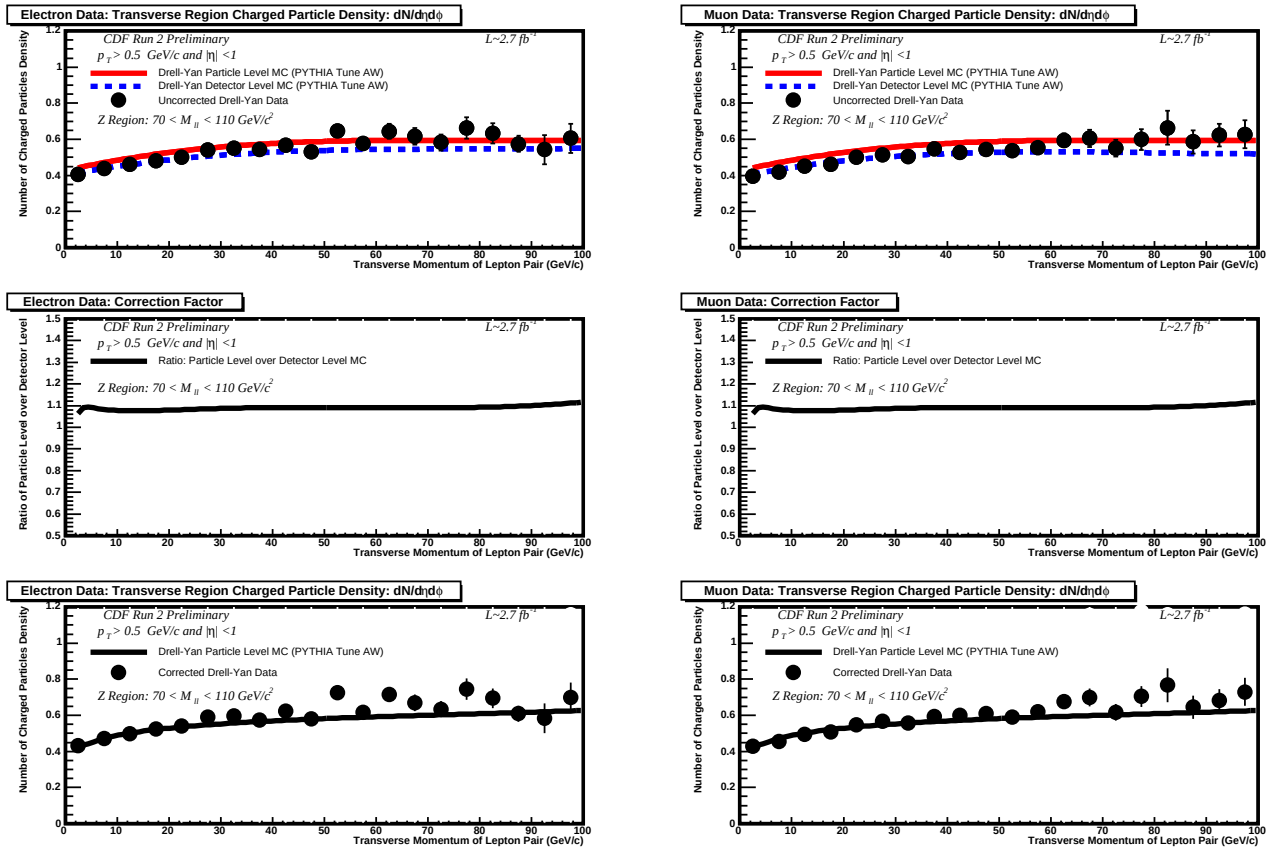

Figure 7-2. Step by step description of how the data are corrected back to particle level, for transverse region charged particle density, as an example. The first row shows uncorrected data, detector level Monte Carlo and particle level Monte Carlo. The second row shows the correction factor obtained by dividing the particle level Monte Carlo by detector level Monte Carlo. The third row shows the data corrected back to particle level by multiplying the correction factor obtained in the previous step. The left side is for electron data and right side is for muon data.

Table 7-1. Systematic uncertainties

Electron data	Muon data
Bin by bin difference between the corrected data for tight-loose electron pair with tight track cut and the corrected data for tight-loose electron pair with loose track cut	Bin by bin difference between the corrected data with tight track cut and the corrected data with loose track cut
Bin by bin difference between the corrected data for tight-loose electron pair with tight track cut and the corrected data with tight-tight electron pair and tight track cut	

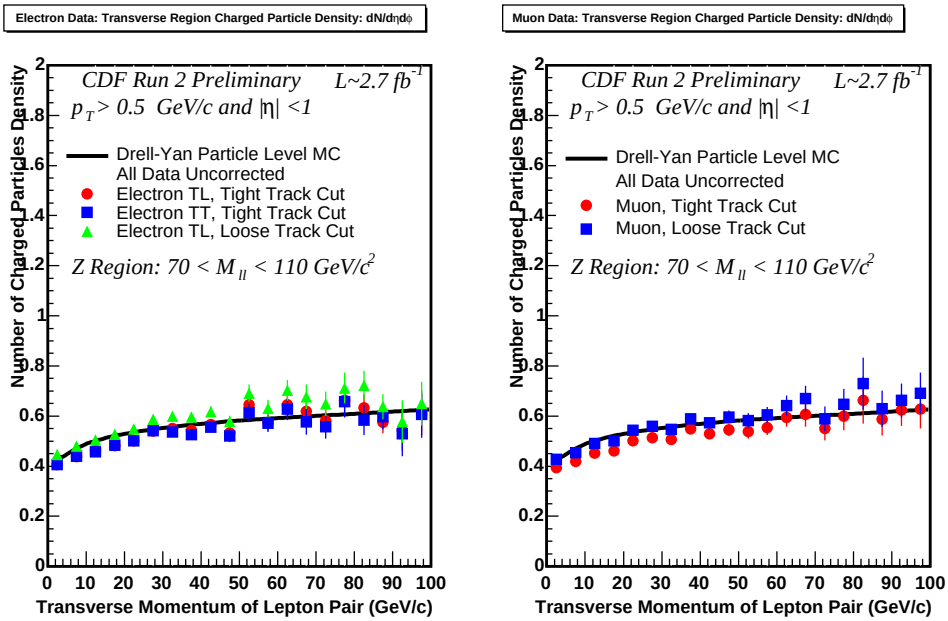

Figure 7-3. Shows the origin of systematic uncertainties in uncorrected data, for transverse region charged particle density, as an example. The left side is for electron data and right side is for muon data.

7.4 Drell-Yan Results

7.4.1 Underlying Event Observables

We present the results on the underlying event observables in the events with the lepton pair invariant mass in the Z-boson region, *i.e.* 70-110 GeV/c^2, with charged particles having $p_T > 0.5$ GeV/c and $|\eta| < 1$. We have combined our electron and muon

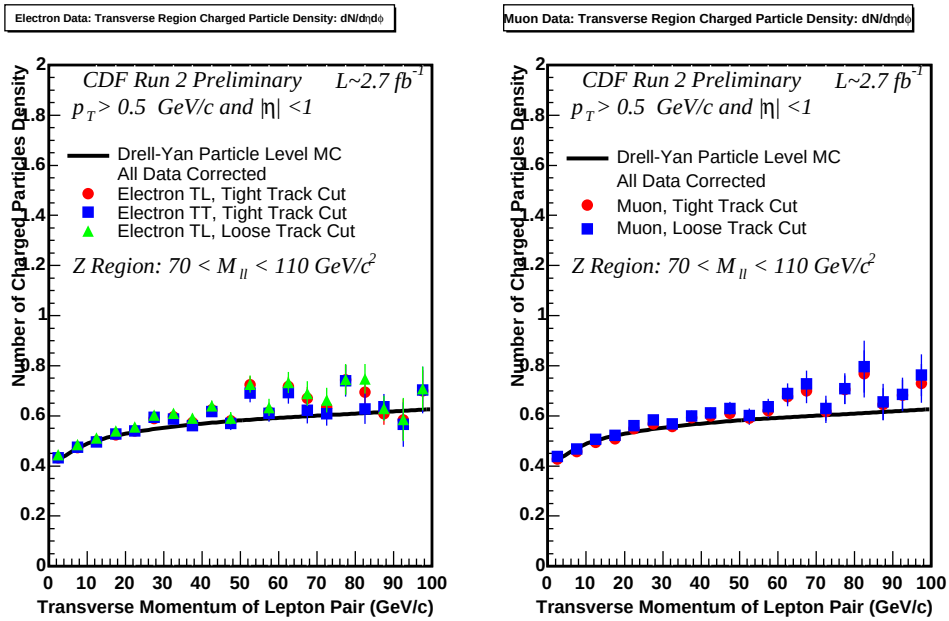

Figure 7-4. Shows the origin of systematic uncertainties in corrected data, for transverse region charged particle density, as an example. The left side is for electron data and right side is for muon data.

results. We present results for lepton pair $p_T < 100$ GeV/c, above which we do not have enough statistics. When filling the histogram, all the events in each bin are averaged over.

Figures 7-5, 7-6 and 7-7 show the data on the density of charged particles for the transverse, toward and the away regions for the Z-boson events, respectively. The densities are plotted as a function of the p_T(Z). The data are corrected to the particle level and compared with PYTHIA tune AW (the solid black line) and HERWIG, without MPI added through JIMMY (the dotted blue line), at the particle level. The toward region corrected data are also compared with HERWIG with MPI added through JIMMY (the dashed green line). In Figures 7-8 we divide the transverse region into transMAX (red) and transMIN (blue). In Figure 7-9, we show the transDIF (*i.e.* transMAX−transMIN) result.

Figures 7-10, 7-11 and 7-12 show the data on the scalar $p_T$sum density for the transverse, toward and the away regions for the Z-boson events, respectively. The densities are plotted as a function of the p_T(Z). The data are corrected to the particle level and

compared with PYTHIA tune AW (the solid black line) and HERWIG, without MPI added through JIMMY (the dotted blue line), at the particle level. The toward region corrected data are also compared with HERWIG with MPI added through JIMMY (the dashed green line). In Figures 7-13 we divide the transverse region into transMAX (red) and transMIN (blue). In Figure 7-14, we show the transDIF (*i.e.* transMAX−transMIN) result.

Figures 7-15, 7-16 and 7-17 show the data on the average charged particle p_T for the transverse, toward and the away regions for the Z-boson events, respectively. The densities are plotted as a function of the p_T(Z). The data are corrected to the particle level and compared with PYTHIA tune AW (the solid black line).

Figures 7-18, 7-19 and 7-20 show the data on the average maximum charged particle p_T for the transverse, toward and the away regions for the Z-boson events, respectively. The densities are plotted as a function of the p_T(Z). The data are corrected to the particle level and compared with PYTHIA tune AW (the solid black line).

Overall, we can see that PYTHIA tune AW does a good job of reproducing the data. HERWIG (without MPI) does not produce enough activity in the transverse region for either process. There is no final-state radiation in Z-boson production so that the lack of MPI becomes more evident. HERWIG (with JIMMY MPI) agrees with tune AW for the scalar $p_T$sum density in the toward and transMIN regions. However, it produces too much charged particle density in these regions. HERWIG (with JIMMY MPI) fits the $p_T$sum density, but it does so by producing too many charged particles (i.e. it has too soft of a p_T spectrum in these regions). This can be seen in Figures 7-16 and 7-19 which shows the data for Z-boson events on the average charged particle p_T and the average maximum charged particle p_T, for the toward region compared with the QCD Monte Carlo models. So the p_T distributions in the transverse region are too soft, resulting in an average p_T and average $p_T$max that are too small. Comparing HERWIG (without MPI) with HERWIG (with JIMMY MPI) clearly shows the importance of MPI in these regions.

7.4.2 Comparing Different Regions

We compare the activity in different regions for the underlying event observables.

Figure 7-21 shows the comparison between the transverse (the solid red line and red data points) and the toward (broken blue line and the blue data points) regions for the density of charged particles. In Figure 7-22 we compare the transMAX (the solid red line and the red data points) and transMIN (the dotted green line and the green data points) regions with the toward (the dashed blue line with the blue data points) region. In Figure 7-23, we compare transverse (the solid red line with the red data points), toward (the dashed blue line with the blue data points) and the away (the dotted black line with the black data points) regions.

Figure 7-24 shows the comparison between transverse (the solid red line and red data points) and the toward (broken blue line and the blue data points) regions for the scalar $p_T$sum density. In Figure 7-25 we compare the transMAX (the solid red line and the red data points) and transMIN (the dotted green line and the green data points) regions with the toward region (the dashed blue line with the blue data points). In Figure 7-26, we compare transverse the solid red line with the red data points), toward the dashed blue line with the blue data points) and the away (the dotted black line with the black data points) regions.

The most sensitive regions to the underlying event in Drell-Yan production are the toward and the transMIN regions. The densities are smaller in the transMIN region than in the toward region and this is described well by PYTHIA tune AW.

Figure 7-27 shows the comparison between the transverse (the solid red line and red data points) and the toward (broken blue line and the blue data points) regions for the average charged particle p_T. In Figure 7-28, we compare transverse (the solid red line with the red data points), toward (the dashed blue line with the blue data points) and the away (the dotted black line with the black data points) regions.

Figure 7-29 shows the comparison between the transverse (the solid red line and red data points) and the toward (broken blue line and the blue data points) regions for the average maximum charged particle p_T. In Figure 7-30, we compare transverse (the solid red line with the red data points), toward (the dashed blue line with the blue data points) and the away (the dotted black line with the black data points) regions.

Finally, in Figure 7-31 and 7-32, we add up the charged particle and the scalar $p_T$sum density for all three regions, and compare with the respective PYTHIA tune AW predictions.

For high transverse momentum Z-boson production, particles from initial-state radiation are more likely to populate the transverse region than the toward region and hence the densities are slightly larger in the transverse region. PYTHIA tune AW describes this very nicely. The away density is large due to the 'away-side' jet. The toward, away, and transverse densities become equal as p_T(Z) goes to zero, but the densities do not vanish at $p_T(\mathrm{Z}) = 0$.

7.4.3 Comparison with the Leading Jet Underlying Event Results

We compared our Drell-Yan underlying event results with the leading jet underlying events results from [70]. Figure 7-33, 7-34, 7-35 and 7-36 show respectively the transverse region charged particle density, scalar $p_T$sum density, average charged particle p_T and the average maximum charged particle p_T for Drell-Yan data (the black data points) and PYTHIA tune AW (the solid black line) predictions compared with the leading jet data (the blue data points)and PYTHIA tune A (the broken blue line) predictions.

For large p_T(jet#1) the transverse densities are similar for leading jet and Z-boson events as one would expect. If the leading jet has no transverse momentum then there are no charged particles, we just get min-bias events. There are a lot of low transverse momentum jets and for $p_T(\mathrm{jet\#1}) < 30$ GeV/c the leading jet is not always the jet resulting from the hard 2-to-2 scattering. This produces is a 'bump' in the transverse density at low p_T.

Figure 7-37 and 7-38 show the transMAX (Red) and transMIN (blue) regions charged particle density and scalar $p_T$sum density for Drell-Yan data (the solid data points) and PYTHIA tune AW (the solid line) predictions compared with the leading jet data (the hollow data points) and PYTHIA tune A (the broken line) predictions.

Figure 7-39 and 7-40 show the transDIF region charged particle density and scalar $p_T$sum density for Drell-Yan data (the black data points) and PYTHIA tune AW (the solid black line) predictions compared with the leading jet data (the blue data points) and PYTHIA tune A (the broken blue line) predictions. The transDIF region is sensitive to the hard initial-state radiation and is predicted to be very similar in the two processes.

Figure 7-41 and 7-42 show the away region charged particle density and scalar $p_T$sum density for Drell-Yan data (the black data points) and PYTHIA tune AW (the solid black line) predictions compared with the leading jet data (the blue data points) and PYTHIA tune A (the broken blue line) predictions.

Here we do not expect the leading jet and Z-boson data to agree and it does not. However, PYTHIA tune A and tune AW describe the data fairly well.

7.4.4 Correlation Between Mean Transverse Momentum and Multiplicity

The correlation between mean p_T and charged multiplicity was first observed by UA1 [72], and then investigated at Tevatron Run 1 [73]. The mean p_T (to be distinguished from the mean event p_T) is obtained by summing the p_T of all charged tracks in an event then dividing by the number of such tracks, as in Table 6-6.

This is an important observable. The rate of change of $\langle p_T \rangle$ versus charged multiplicity is a measure of the amount of hard versus soft processes contributing to collisions and it is sensitive the modeling of the multipleparton interactions [75]. If only the soft beam-beam remnants contributed to min-bias collisions then $\langle p_T \rangle$ would not depend on charged multiplicity. If one has two processes contributing, one soft (beam-beam remnants) and one hard (hard 2-to-2 partonparton scattering), then demanding large multiplicity would preferentially select the hard process and lead to a high $\langle p_T \rangle$. However, we see that with

only these two processes $\langle p_T \rangle$ increases much too rapidly as a function of multiplicity. Multiple-parton interactions provides another mechanism for producing large multiplicities that are harder than the beam-beam remnants, but not as hard as the primary 2-to-2 hard scattering.

Figure 7-43 shows the data corrected to the particle level on the average p_T of charged particles versus the multiplicity for charged particles with $p_T > 0.5$ GeV/c and $|\eta| < 1$ for Z-boson events from this analysis. HERWIG (without MPI) predicts the $\langle p_T \rangle$ to rise too rapidly as the multiplicity increases. For HERWIG (without MPI) large multiplicities come from events with a high p_T Z-boson and hence a large p_T 'away-side' jet. This can be seen clearly in Figure 7-44 which shows the average p_T of the Z-boson versus the charged multiplicity. Without MPI the only way of getting large multiplicity is with high p_T(Z) events. For the models with MPI one can get large multiplicity either from high p_T(Z) events or from MPI and hence $\langle p_T(Z) \rangle$ does not rise as sharply with multiplicity in accord with the data. PYTHIA tune AW describes the data Z-boson fairly well.

Figure 7-45 shows the data corrected to the particle level on the average p_T of charged particles versus the multiplicity for charged particles with $p_T > 0.5$ GeV/c and $|\eta| < 1$ for Z-boson events in which $p_T(Z) < 10$ GeV/c. We see that $\langle p_T \rangle$ still increases as the multiplicity increases although not as fast. If we require $p_T(Z) < 10$ GeV/c, than HERWIG (without MPI) predicts that the $\langle p_T \rangle$ decreases slightly as the multiplicity increases. This is because without MPI and without the high p_T 'away-side' jet which is suppressed by requiring low $p_T(Z)$, large multiplicities come from events with a lot of initial-state radiation and the particles coming from initial-state radiation are 'soft'. PYTHIA tune AW describes the behavior of $\langle p_T \rangle$ versus the multiplicity fairly well even when we select $p_T(Z) < 10$ GeV/c. This strongly suggests that MPI are playing an important role in both these processes.

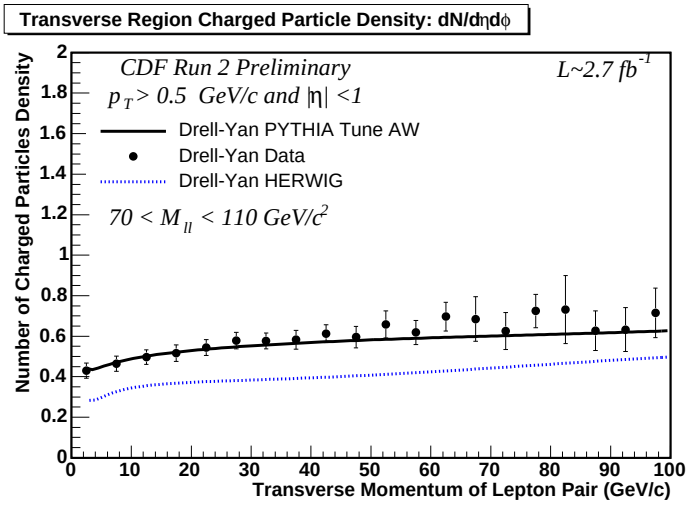

Figure 7-5. Drell-Yan transverse region charged multiplicity density, electron and muon data combined ($p_T > 0.5$ GeV/c and $|\eta| < 1$). Lines represent PYTHIA tune AW and HERWIG predictions and the data are corrected back to particle level (with errors that include both the statistical error and the systematic uncertainty).

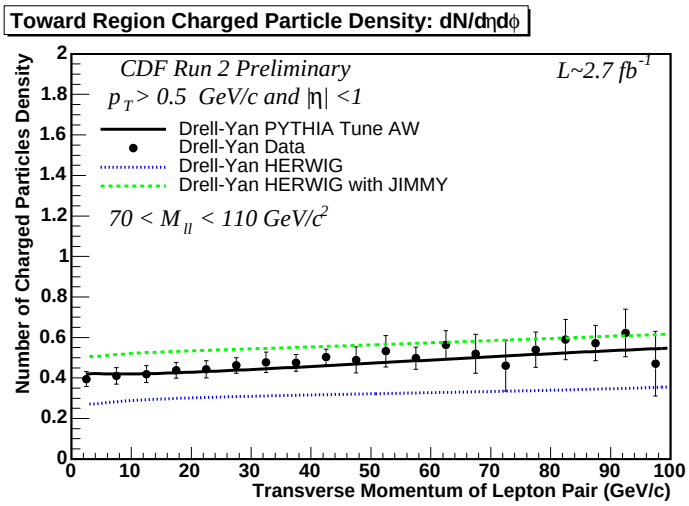

Figure 7-6. Drell-Yan toward region charged multiplicity density, electron and muon data combined ($p_T > 0.5$ GeV/c and $|\eta| < 1$). Lines represents PYTHIA tune AW, HERWIG and HERWIG+JIMMY predictions and the data are corrected back to particle level (with errors that include both the statistical error and the systematic uncertainty).

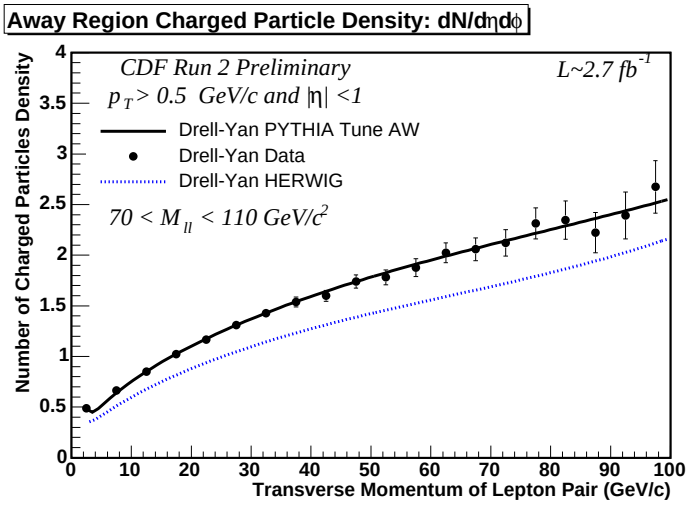

Figure 7-7. Drell-Yan away region charged multiplicity density, electron and muon data combined ($p_T > 0.5$ GeV/c and $|\eta| < 1$). Lines represent PYTHIA tune AW and HERWIG predictions and the data are corrected back to particle level (with errors that include both the statistical error and the systematic uncertainty).

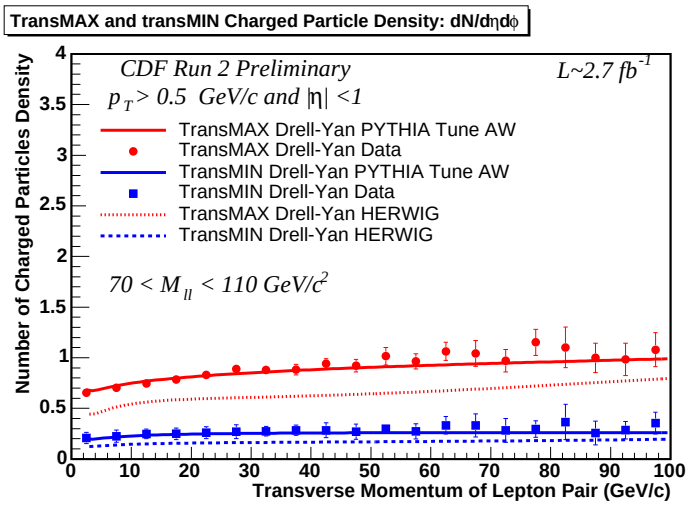

Figure 7-8. Drell-Yan transMAX and transMIN regions charged multiplicity density, electron and muon data combined ($p_T > 0.5$ GeV/c and $|\eta| < 1$). Lines represent PYTHIA tune AW and HERWIG predictions and the data are corrected back to particle level (with errors that include both the statistical error and the systematic uncertainty).

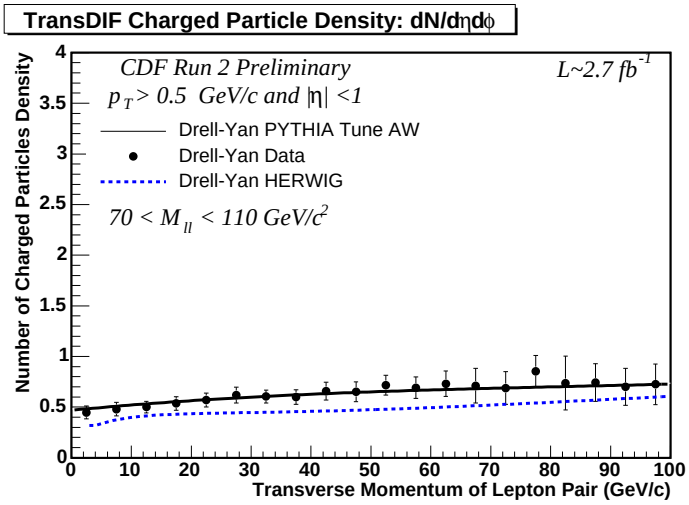

Figure 7-9. Drell-Yan transDIF region charged multiplicity density, electron and muon data combined ($p_T > 0.5$ GeV/c and $|\eta| < 1$). Lines represent PYTHIA tune AW and HERWIG predictions and the data are corrected back to particle level (with errors that include both the statistical error and the systematic uncertainty).

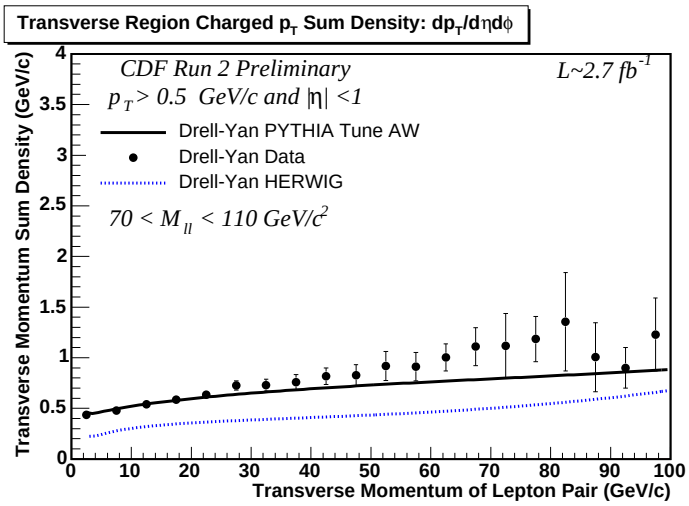

Figure 7-10. Drell-Yan transverse region charged p_T sum density, electron and muon data combined ($p_T > 0.5$ GeV/c and $|\eta| < 1$). Lines represent PYTHIA tune AW and HERWIG predictions and the data are corrected back to particle level (with errors that include both the statistical error and the systematic uncertainty).

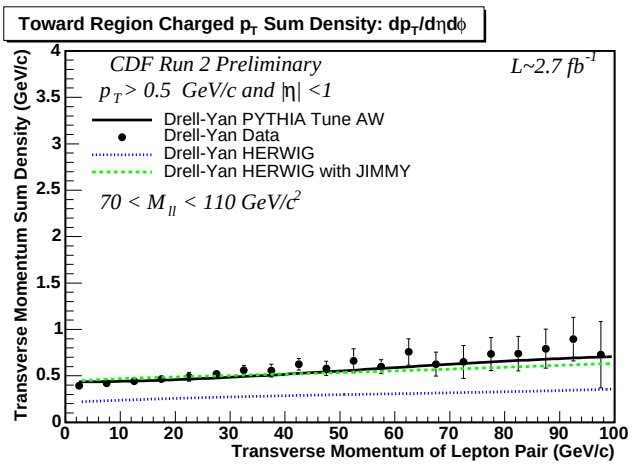

Figure 7-11. Drell-Yan toward region charged p_T sum density, electron and muon data combined ($p_T > 0.5$ GeV/c and $|\eta| < 1$). Lines represent PYTHIA tune AW, HERWIG and HERWIG+JIMMY predictions and the data are corrected back to particle level (with errors that include both the statistical error and the systematic uncertainty).

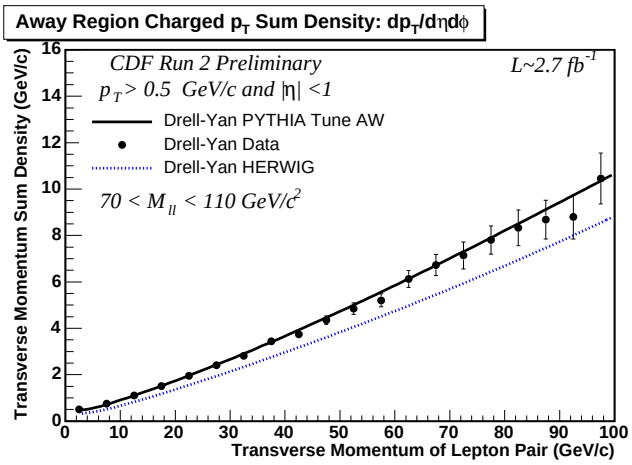

Figure 7-12. Drell-Yan away region charged p_T sum density, electron and muon data combined ($p_T > 0.5$ GeV/c and $|\eta| < 1$). Lines represents PYTHIA tune AW and HERWIG predictions and the data are corrected back to particle level (with errors that include both the statistical error and the systematic uncertainty).

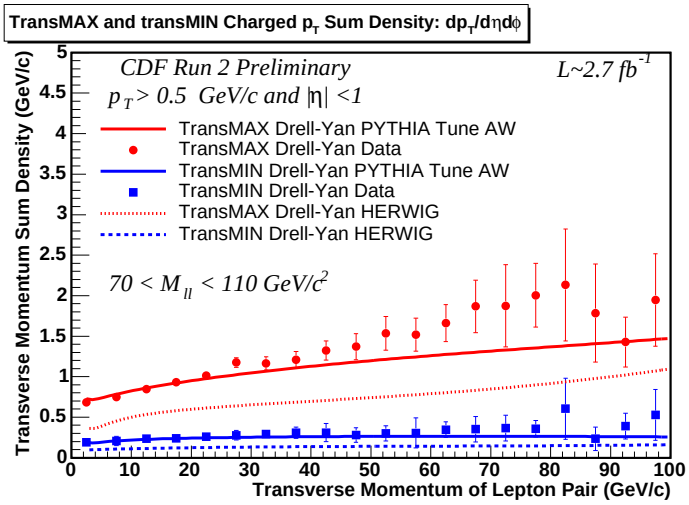

Figure 7-13. Drell-Yan transMAX and transMIN region charged p_T sum density, electron and muon data combined ($p_T > 0.5$ GeV/c and $|\eta| < 1$). Lines represent PYTHIA tune AW and HERWIG predictions and the data are corrected back to particle level (with errors that include both the statistical error and the systematic uncertainty).

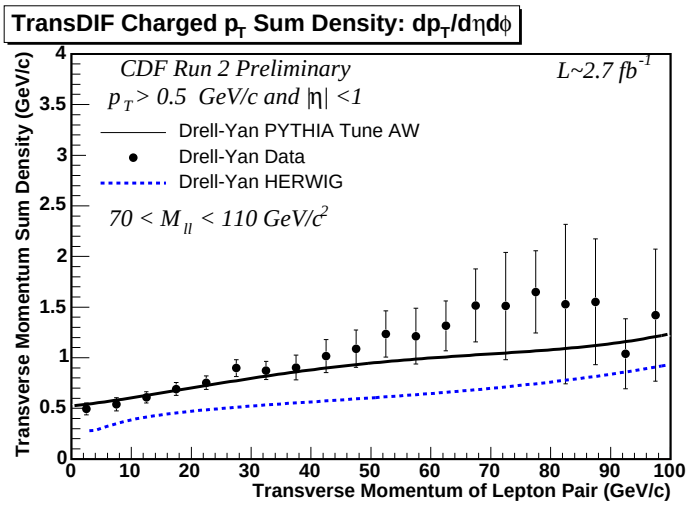

Figure 7-14. Drell-Yan transDIF region charged p_T sum density, electron and muon data combined ($p_T > 0.5$ GeV/c and $|\eta| < 1$). Lines represent PYTHIA tune AW and HERWIG predictions and the data are corrected back to particle level (with errors that include both the statistical error and the systematic uncertainty).

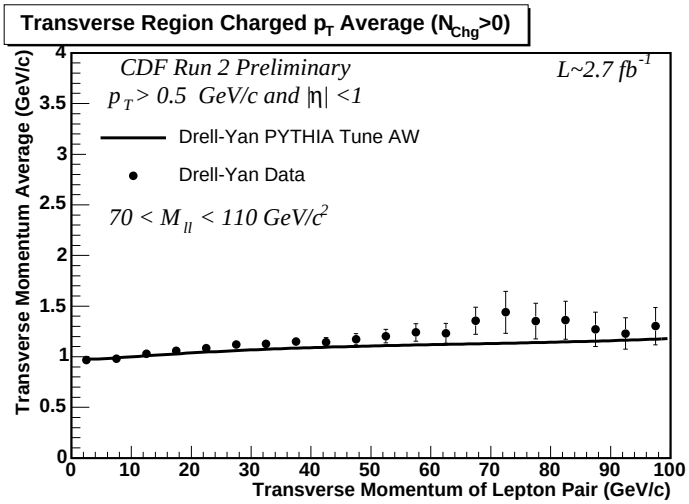

Figure 7-15. Drell-Yan transverse region charged p_T average, electron and muon data combined ($p_T > 0.5$ GeV/c and $|\eta| < 1$). Solid line represents PYTHIA tune AW predictions and the data are corrected back to particle level (with errors that include both the statistical error and the systematic uncertainty).

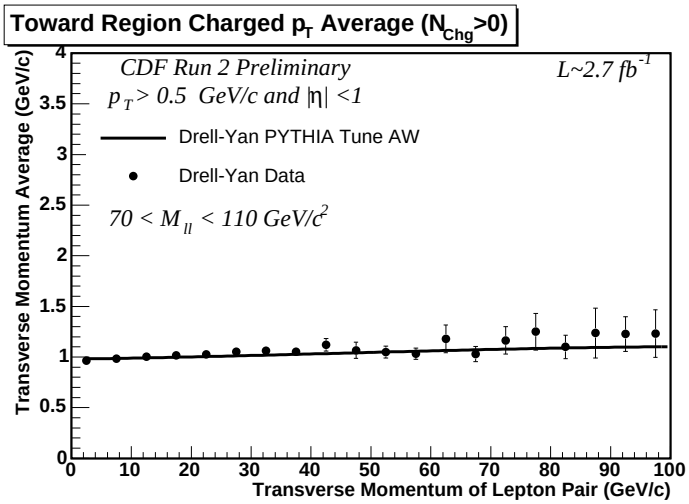

Figure 7-16. Drell-Yan toward region charged p_T average, electron and muon data combined ($p_T > 0.5$ GeV/c and $|\eta| < 1$). Solid line represents PYTHIA tune AW predictions and the data are corrected back to particle level (with errors that include both the statistical error and the systematic uncertainty).

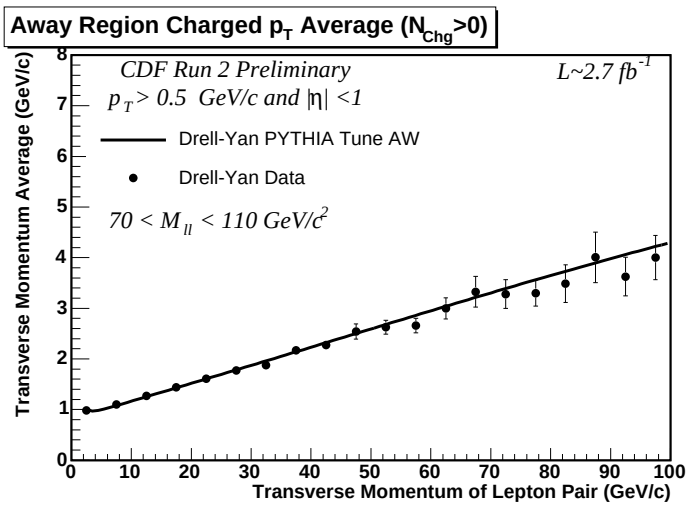

Figure 7-17. Drell-Yan away region charged p_T average, electron and muon data combined ($p_T > 0.5$ GeV/c and $|\eta| < 1$). Solid line represents PYTHIA tune AW predictions and the data are corrected back to particle level (with errors that include both the statistical error and the systematic uncertainty).

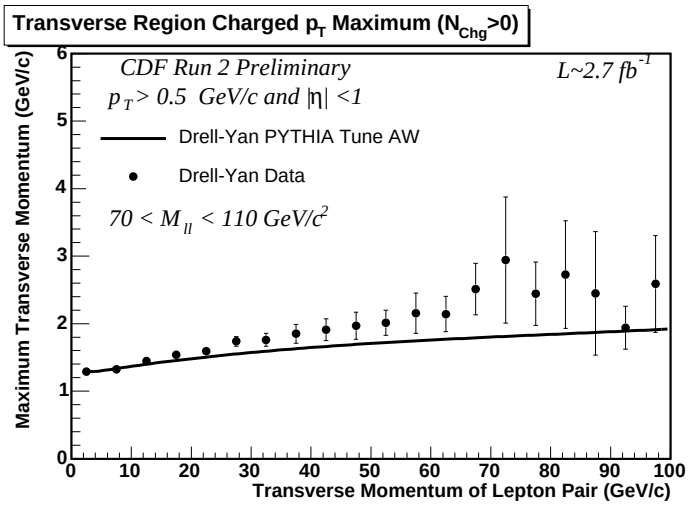

Figure 7-18. Drell-Yan transverse region charged p_T maximum, electron and muon data combined ($p_T > 0.5$ GeV/c and $|\eta| < 1$). Solid line represents PYTHIA tune AW predictions and the data are corrected back to particle level (with errors that include both the statistical error and the systematic uncertainty).

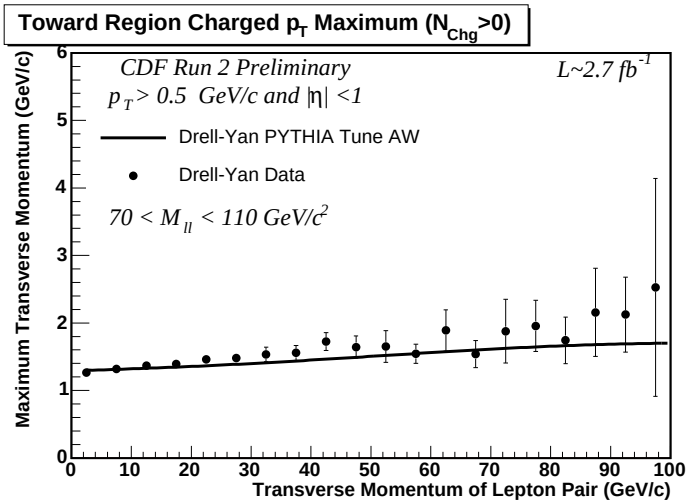

Figure 7-19. Drell-Yan toward region charged p_T maximum, electron and muon data combined ($p_T > 0.5$ GeV/c and $|\eta| < 1$). Solid line represents PYTHIA tune AW predictions and the data are corrected back to particle level (with errors that include both the statistical error and the systematic uncertainty).

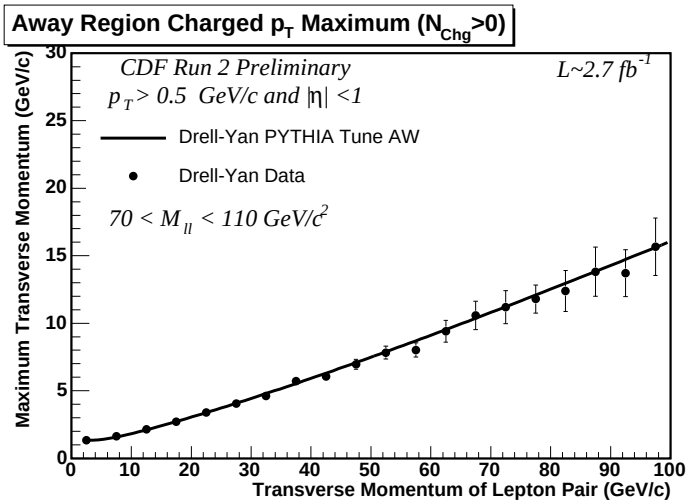

Figure 7-20. Drell-Yan away region charged p_T maximum, electron and muon data combined ($p_T > 0.5$ GeV/c and $|\eta| < 1$). Solid line represents PYTHIA tune AW predictions and the data are corrected back to particle level(with errors that include both the statistical error and the systematic uncertainty)

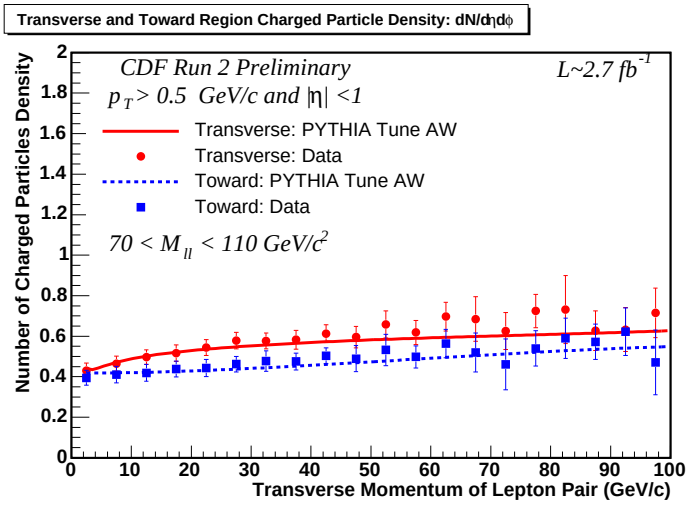

Figure 7-21. Overlaying Drell-Yan transverse and toward regions charged multiplicity density, electron and muon data combined ($p_T > 0.5$ GeV/c and $|\eta| < 1$). Lines represent PYTHIA tune AW predictions and the data are corrected back to particle level (with errors that include both the statistical error and the systematic uncertainty).

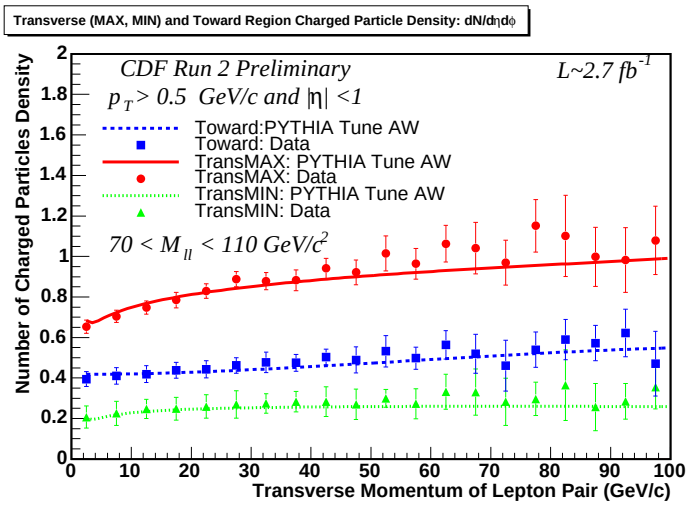

Figure 7-22. Overlaying Drell-Yan transMAX, transMIN and toward regions charged multiplicity density, electron and muon data combined ($p_T > 0.5$ GeV/c and $|\eta| < 1$). Lines represent PYTHIA tune AW predictions and the data are corrected back to particle level (with errors that include both the statistical error and the systematic uncertainty).

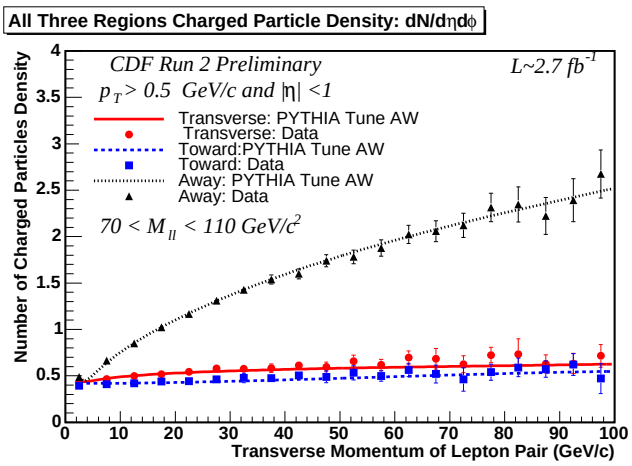

Figure 7-23. Overlaying Drell-Yan all three regions charged multiplicity density, electron and muon data combined ($p_T > 0.5$ GeV/c and $|\eta| < 1$). Lines represent PYTHIA tune AW predictions and the data are corrected back to particle level (with errors that include both the statistical error and the systematic uncertainty).

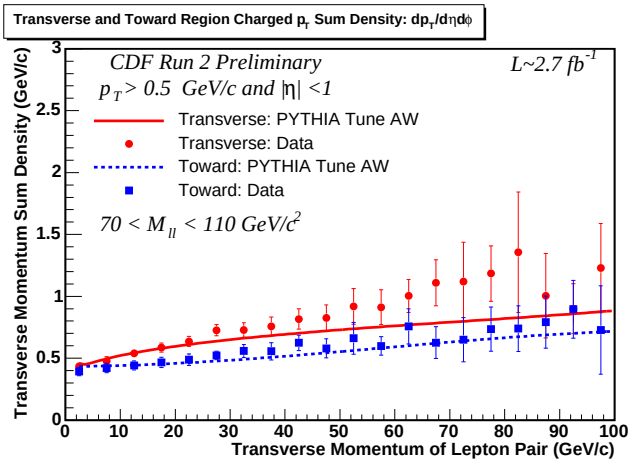

Figure 7-24. Overlaying Drell-Yan transverse and toward regions charged p_T sum density, electron and muon data combined ($p_T > 0.5$ GeV/c and $|\eta| < 1$). Lines represent PYTHIA tune AW predictions and the data are corrected back to particle level (with errors that include both the statistical error and the systematic uncertainty).

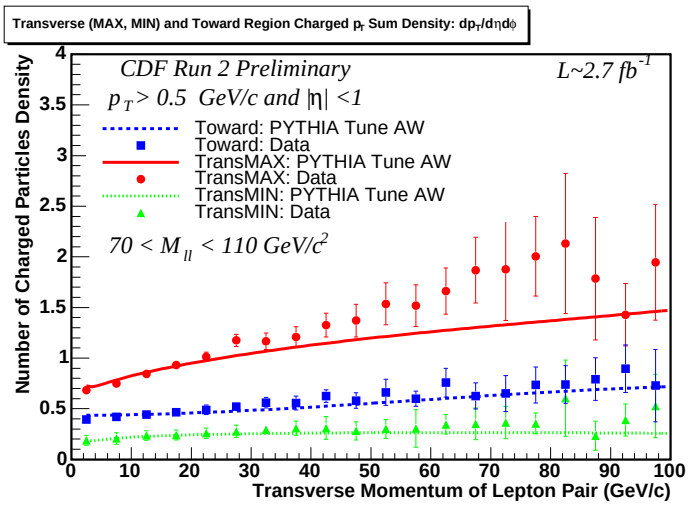

Figure 7-25. Overlaying Drell-Yan transMAX, transMIN and toward regions charged p_T sum density, electron and muon data combined ($p_T > 0.5$ GeV/c and $|\eta| < 1$). Lines represent PYTHIA tune AW predictions and the data are corrected back to particle level (with errors that include both the statistical error and the systematic uncertainty).

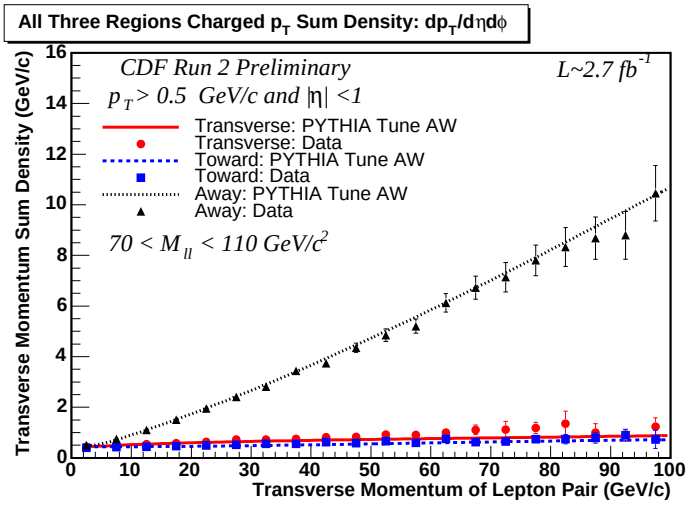

Figure 7-26. Overlaying Drell-Yan all three regions charged p_T sum density, electron and muon data combined ($p_T > 0.5$ GeV/c and $|\eta| < 1$). Lines represent PYTHIA tune AW predictions and the data are corrected back to particle level (with errors that include both the statistical error and the systematic uncertainty).

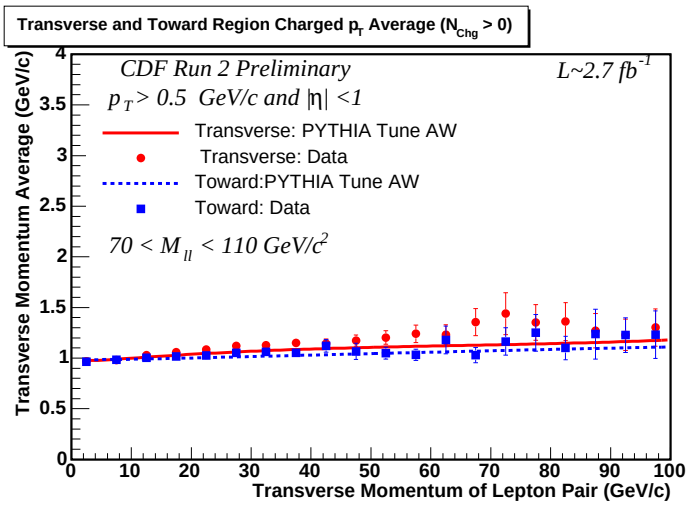

Figure 7-27. Overlaying Drell-Yan transverse and toward regions charged p_T average, electron and muon data combined ($p_T > 0.5$ GeV/c and $|\eta| < 1$). Lines represent PYTHIA tune AW predictions and the data are corrected back to particle level (with errors that include both the statistical error and the systematic uncertainty).

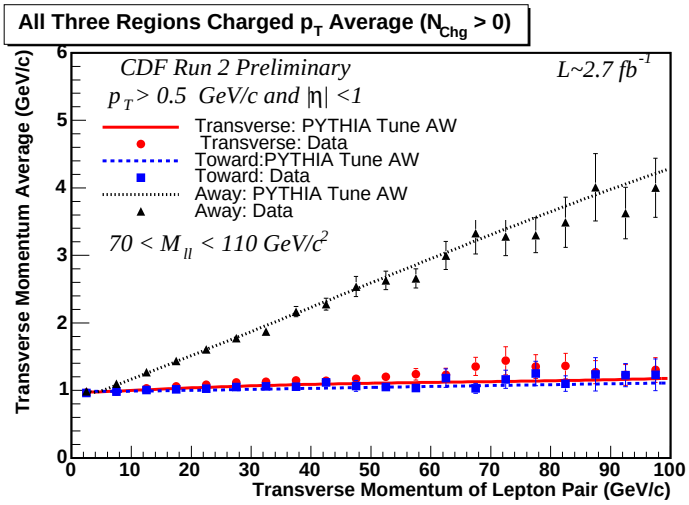

Figure 7-28. Overlaying Drell-Yan all three regions charged p_T average, electron and muon data combined ($p_T > 0.5$ GeV/c and $|\eta| < 1$). Lines represent PYTHIA tune AW predictions and the data are corrected back to particle level (with errors that include both the statistical error and the systematic uncertainty).

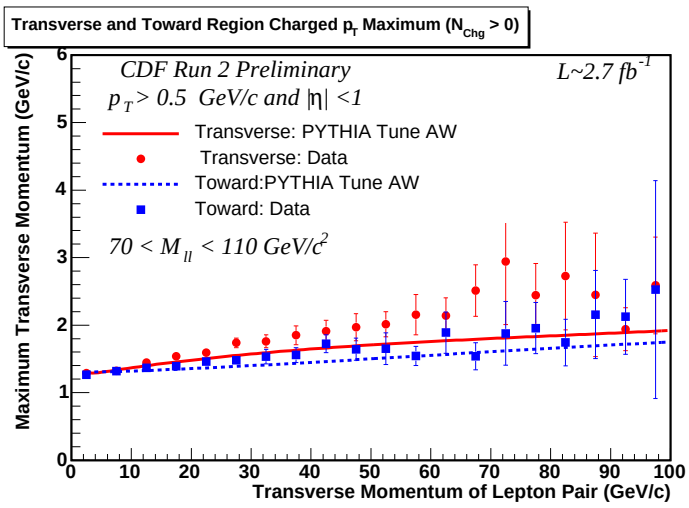

Figure 7-29. Overlaying Drell-Yan transverse and toward regions charged p_T maximum, electron and muon data combined ($p_T > 0.5$ GeV/c and $|\eta| < 1$). Lines represent PYTHIA tune AW predictions and the data are corrected back to particle level (with errors that include both the statistical error and the systematic uncertainty).

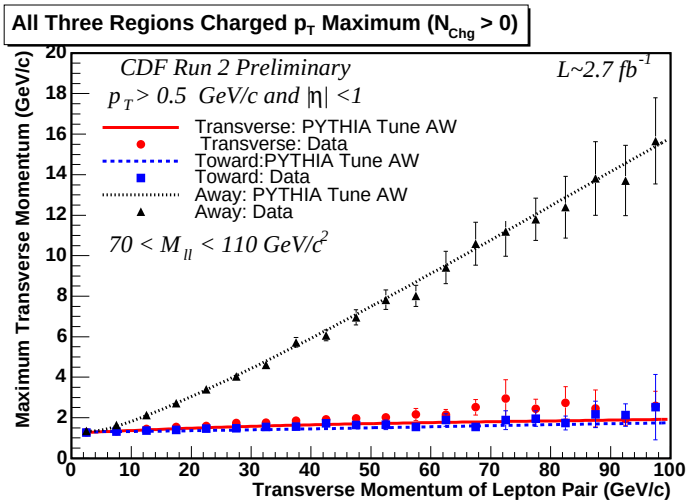

Figure 7-30. Overlaying Drell-Yan all three regions charged p_T maximum, electron and muon data combined ($p_T > 0.5$ GeV/c and $|\eta| < 1$). Lines represent PYTHIA tune AW predictions and the data are corrected back to particle level (with errors that include both the statistical error and the systematic uncertainty).

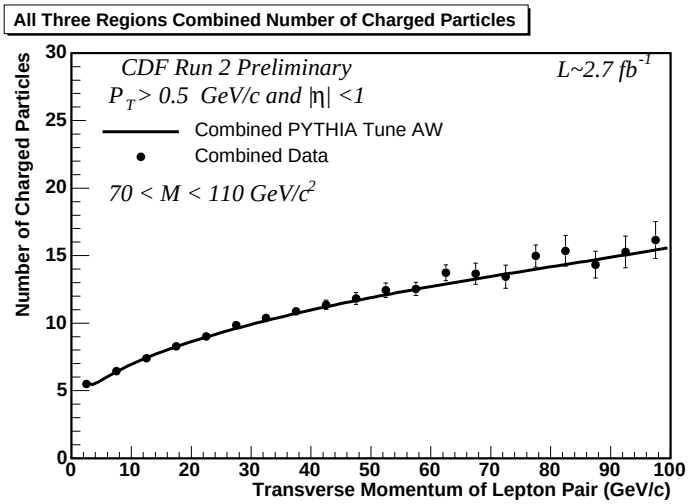

Figure 7-31. Drell-Yan all three regions charged multiplicity density added up, electron and muon data combined ($p_T > 0.5$ GeV/c and $|\eta| < 1$). Lines represent PYTHIA tune AW predictions and the data are corrected back to particle level (with errors that include both the statistical error and the systematic uncertainty).

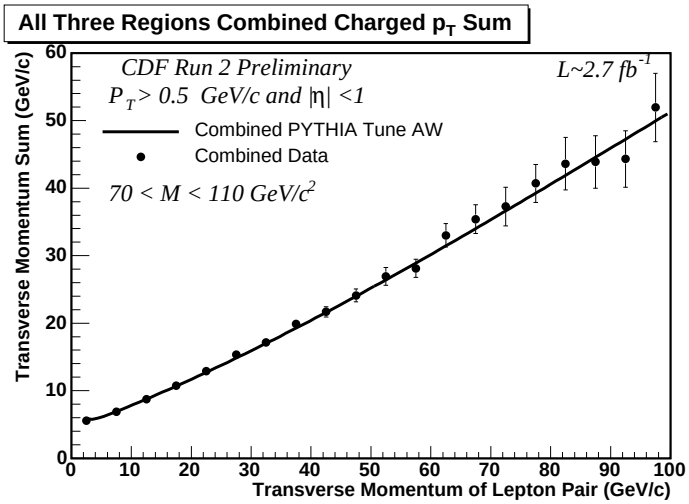

Figure 7-32. Drell-Yan all three regions charged p_T sum density added up, electron and muon data combined ($p_T > 0.5$ GeV/c and $|\eta| < 1$). Lines represent PYTHIA tune AW predictions and the data are corrected back to particle level (with errors that include both the statistical error and the systematic uncertainty).

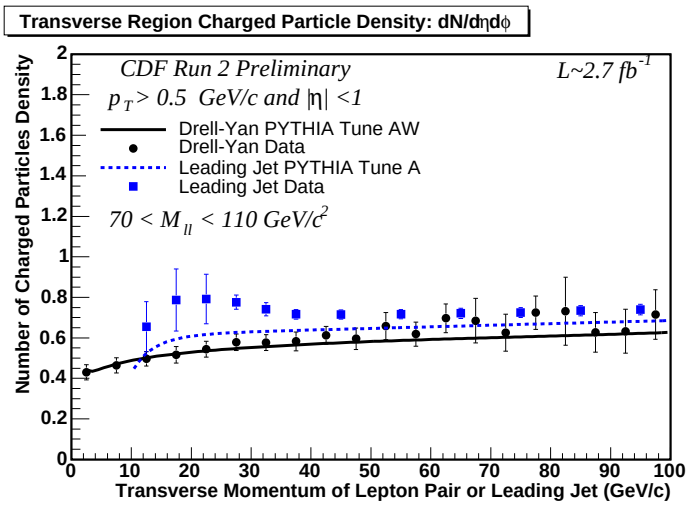

Figure 7-33. Drell-Yan transverse region charged multiplicity density, compared with leading jet result ($p_T > 0.5$ GeV/c and $|\eta| < 1$). Lines represent PYTHIA tune A and tune AW predictions and the data are corrected back to particle level (with errors that include both the statistical error and the systematic uncertainty).

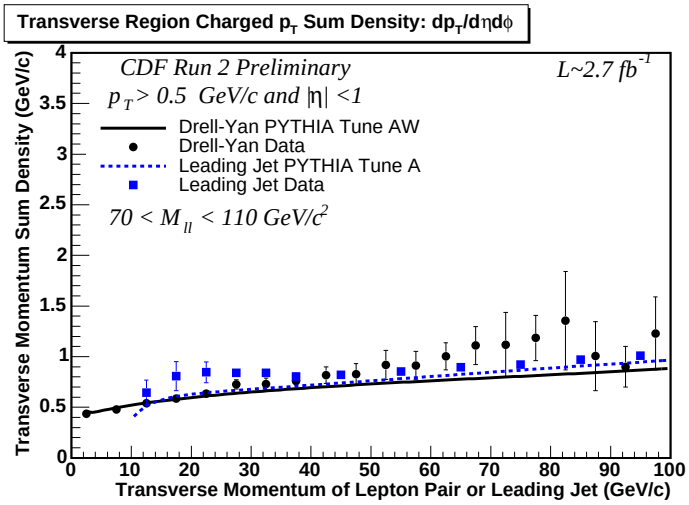

Figure 7-34. Drell-Yan transverse region charged p_T sum density, compared with leading jet result ($p_T > 0.5$ GeV/c and $|\eta| < 1$). Lines represent PYTHIA tune A and tune AW predictions and the data are corrected back to particle level (with errors that include both the statistical error and the systematic uncertainty).

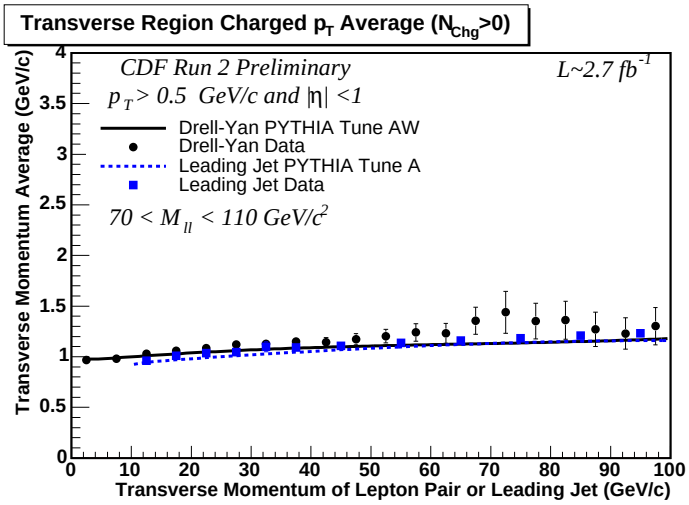

Figure 7-35. Drell-Yan transverse region charged p_T average, compared with leading jet result ($p_T > 0.5$ GeV/c and $|\eta| < 1$). Lines represent PYTHIA tune A and tune AW predictions and the data are corrected back to particle level (with errors that include both the statistical error and the systematic uncertainty).

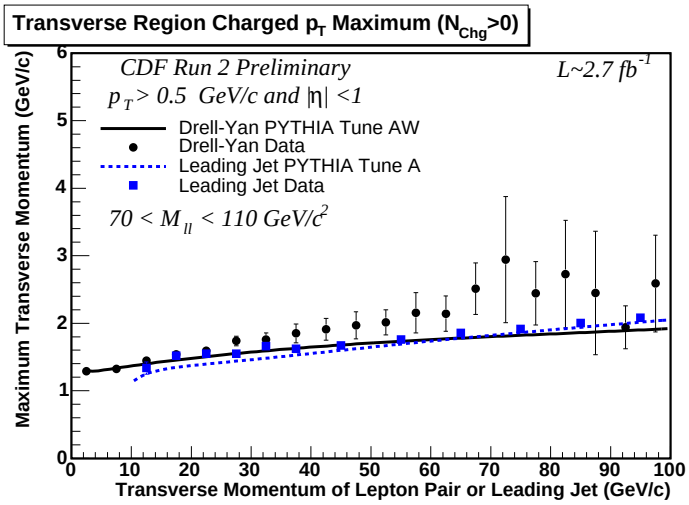

Figure 7-36. Drell-Yan transverse region charged p_T maximum, compared with leading jet result ($p_T > 0.5$ GeV/c and $|\eta| < 1$). Lines represent PYTHIA tune A and tune AW predictions and the data are corrected back to particle level (with errors that include both the statistical error and the systematic uncertainty).

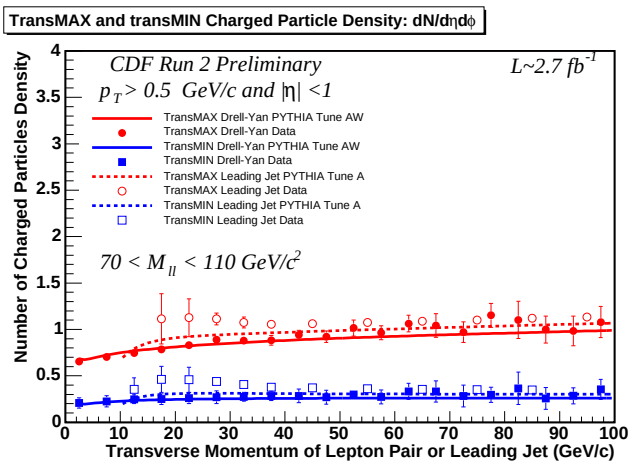

Figure 7-37. Drell-Yan transMAX and transMIN regions charged multiplicity density, compared with leading jet result ($p_T > 0.5$ GeV/c and $|\eta| < 1$). Lines represent PYTHIA tune A and tune AW predictions and the data are corrected back to particle level (with errors that include both the statistical error and the systematic uncertainty).

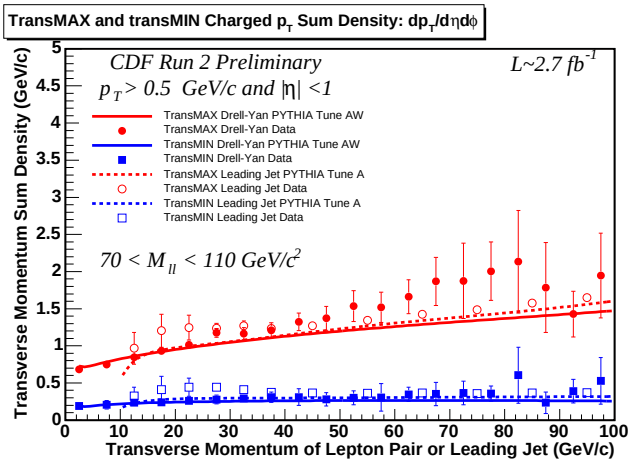

Figure 7-38. Drell-Yan transMAX and transMIN regions charged p_T sum density, compared with leading jet result ($p_T > 0.5$ GeV/c and $|\eta| < 1$). Lines represent PYTHIA tune A and tune AW predictions and the data are corrected back to particle level (with errors that include both the statistical error and the systematic uncertainty).

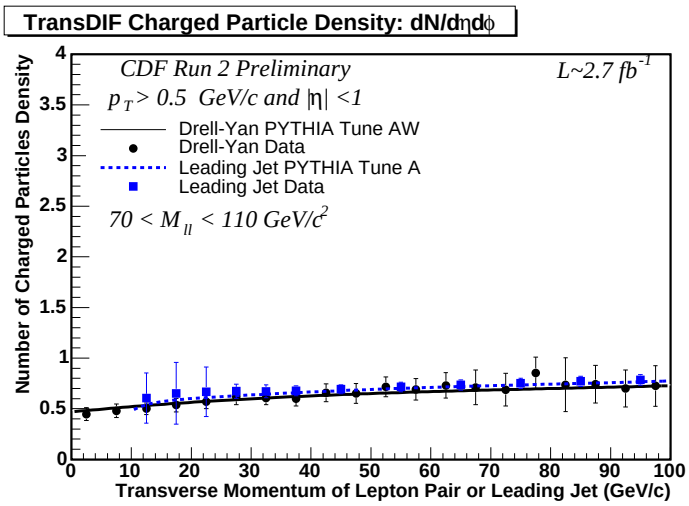

Figure 7-39. Drell-Yan transDIF region charged multiplicity density, compared with leading jet result ($p_T > 0.5$ GeV/c and $|\eta| < 1$). Lines represent PYTHIA tune A and tune AW predictions and the data are corrected back to particle level (with errors that include both the statistical error and the systematic uncertainty).

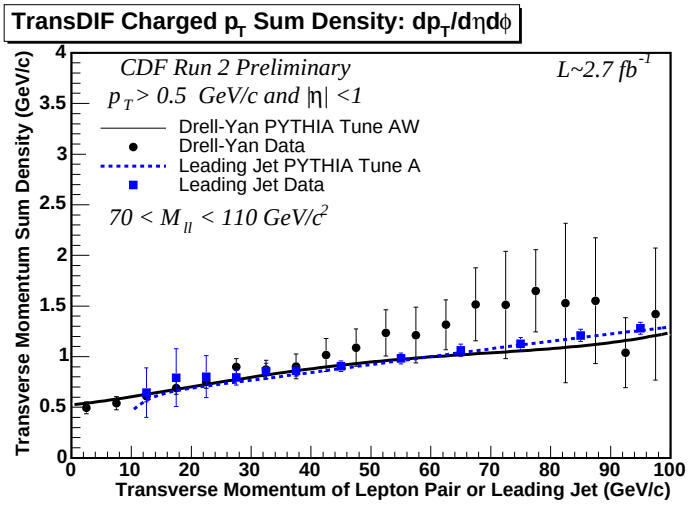

Figure 7-40. Drell-Yan transDIF region charged p_T sum density, compared with leading jet result ($p_T > 0.5$ GeV/c and $|\eta| < 1$). Lines represent PYTHIA tune A and tune AW predictions and the data are corrected back to particle level (with errors that include both the statistical error and the systematic uncertainty).

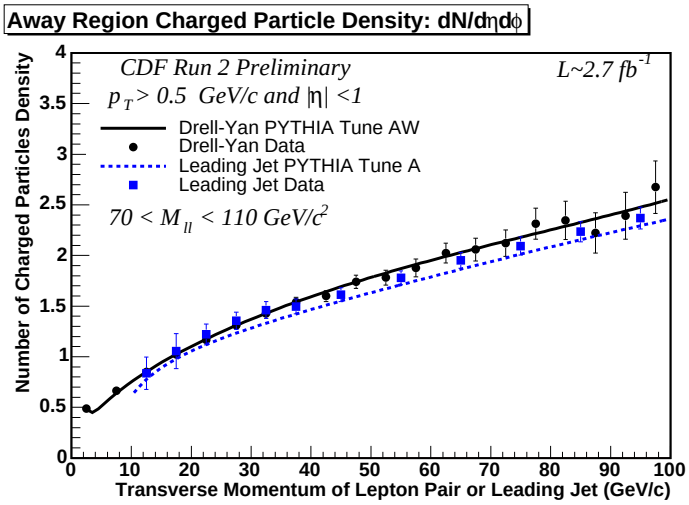

Figure 7-41. Drell-Yan away region charged multiplicity density, compared with leading jet result ($p_T > 0.5$ GeV/c and $|\eta| < 1$). Lines represent PYTHIA tune A and tune AW predictions and the data are corrected back to particle level (with errors that include both the statistical error and the systematic uncertainty).

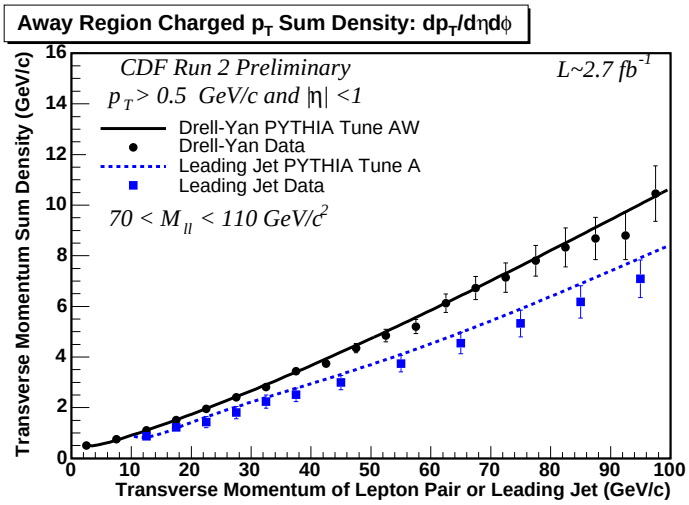

Figure 7-42. Drell-Yan away region charged p_T sum density, compared with leading jet result ($p_T > 0.5$ GeV/c and $|\eta| < 1$). Lines represent PYTHIA tune A and tune AW predictions and the data are corrected back to particle level (with errors that include both the statistical error and the systematic uncertainty).

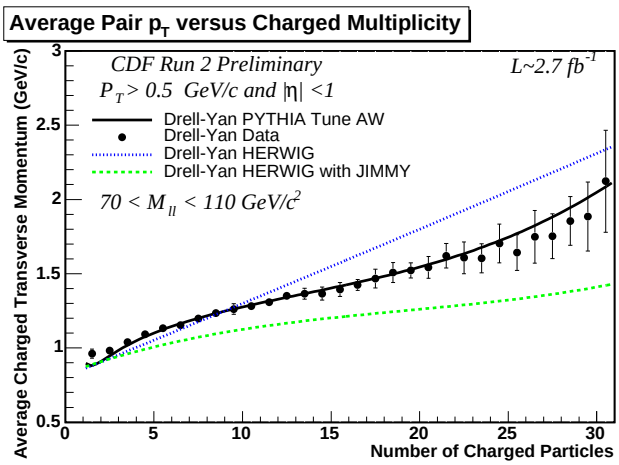

Figure 7-43. Drell-Yan charged p_T average and charged multiplicity correlation, electron and muon data combined ($p_T > 0.5$ GeV/c and $|\eta| < 1$). Lines represent PYTHIA tune AW, HERWIG and HERWIG+JIMMY predictions and the data are corrected back to particle level (with errors that include both the statistical error and the systematic uncertainty).

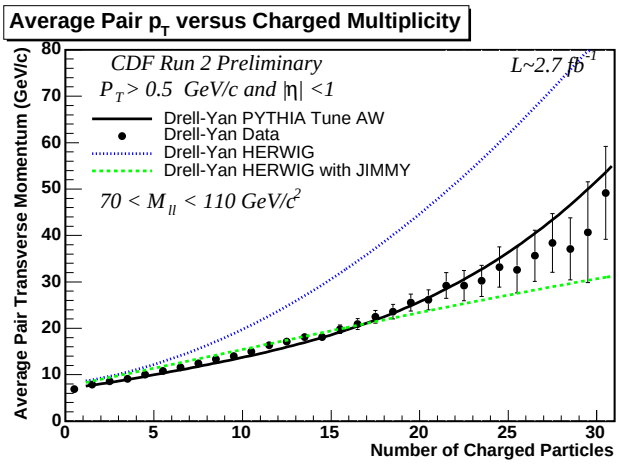

Figure 7-44. Drell-Yan pair p_T average and charged multiplicity correlation, electron and muon data combined ($p_T > 0.5$ GeV/c and $|\eta| < 1$). Lines represent PYTHIA tune A, HERWIG and HERWIG+JIMMY predictions and the data are corrected back to particle level (with errors that include both the statistical error and the systematic uncertainty).

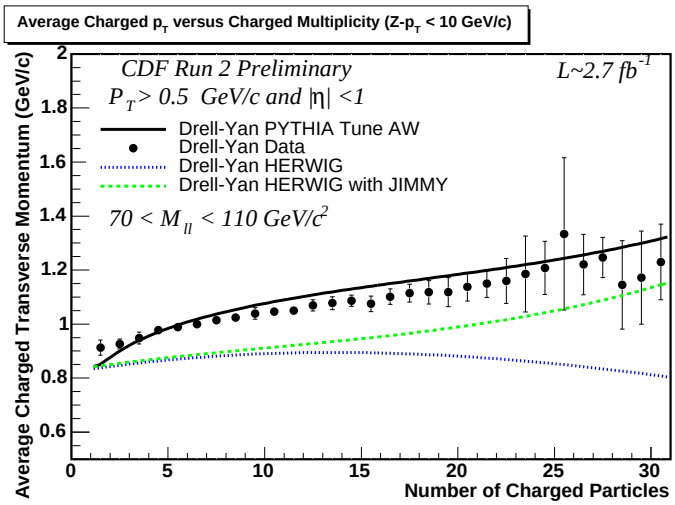

Figure 7-45. Drell-Yan charged p_T average and charged multiplicity correlation, with Z-p_T < 10 GeV/c, electron and muon data combined ($p_T > 0.5$ GeV/c and $|\eta| < 1$). Lines represent PYTHIA tune AW, HERWIG and HERWIG+JIMMY predictions and the data are corrected back to particle level (with errors that include both the statistical error and the systematic uncertainty).

CHAPTER 8
SUMMARY AND CONCLUSION

8.1 Conclusions

Observables that are sensitive to the underlying event in Drell-Yan lepton-pair production in the mass region of the Z-boson have been presented and compared with several QCD Monte Carlo models. The data are corrected to the particle level and compared with the Monte Carlo models at the at the particle level (*i.e.* generator level). The primary goal of this analysis is to produce data that can be used by the theorists to tune and improve the QCD Monte Carlo models of the underlying event that are used to simulate hadron-hadron collisions. The data presented here are very important for improving the QCD Monte-Carlo MPI models.

The underlying event observables are found to be essentially flat with the increasing lepton pair transverse momentum in the transverse and toward regions, but increases in the away region to balance the Z-boson p_T. We observed a slight excess at transverse region compared to toward region, which is caused by transverse regions receiving contributions from initial state radiation. We observed very good agreements with PYTHIA tune AW Monte Carlo predictions, although the agreement between theory and data is not perfect. We also compared them with leading jet underlying event results and observed reasonably close agreement - which may indicate the universality of underlying event modeling. We have to note that dijet and Drell-Yan events have distinctly different topologies. At very low p_T, Z-boson still has a large invariant mass, whereas there can be no leading jet in that region - which explains the apparent differences between dijet and Drell-Yan underlying events in low p_T region. The away-side jet is not constrained to be in the away region in either cases, and their probability distribution for being at a certain η range are different for each case. That explains the difference of leading jet with Drell-Yan underlying event results. The leading jet data show slightly more activity in the underlying event than PYTHIA tune A. All the tunes with MPI agree much better

than HERWIG without MPI. This is especially true for the toward region in Z-boson production. Adding JIMMY MPI to HERWIG greatly improves the agreement with data, but HERWIG with JIMMY MPI produces a charged particle p_T spectra that is considerably 'softer' than the data. The PYTHIA ATLAS tune also produces a charged particle p_T spectra that is considerably 'softer' than the data.

The behavior of the average charged particle p_T versus the charged particle multiplicity is an important observable. The rate of change of $\langle p_T \rangle$ versus charged multiplicity is a measure of the amount of hard versus soft processes contributing and it is sensitive the modeling of the multiple-parton interactions. The general trend is that the tracks in high-multiplicity events are harder on average than in low multiplicity ones. Mean p_T increases at low multiplicity, which suggests that an increasing contribution from hard gluon production, as proposed in [74]. We also see that the tunes roughly agree for low-multiplicity events, however none of the Monte Carlo event generators, including PYTHIA could not reproduce the full final state correlation before, although a great progress has been done since Run 1. The naive expectation from an uncorrelated system of strings decaying to hadrons would be that $\langle p_\perp \rangle$ should be independent of N_{Chg}. To make the average $p_\perp$ rise sufficiently to agree with Tevatron data, tune A incorporate strong color correlations between final-state partons from different interactions, chosen in such a way as to minimize the resulting string length [75].

PYTHIA tune A and tune AW do a good job in describing the data on $\langle p_\perp \rangle$ versus multiplicity for min-bias [77] and Z-boson events, respectively, although again the agreement between theory and data is not perfect. It has been seen that that the behavior of $\langle p_T \rangle$ versus multiplicity is remarkably similar for min-bias events and Z-boson events with $p_T(Z) < 10$ GeV/c suggesting that MPI are playing an important role in both these processes. Measurements of these distributions, both at present and future colliders, would therefore add another highly interesting and complementary piece of information on the physics processes.

8.2 Looking Ahead to the LHC

The 'Large Hadron Collider', situated at the European Organization for Nuclear Research (CERN) in France-Switzerland border, is expected to start colliding proton-proton beams at 7 times more center of mass energy and 100 times more luminosity than the Tevatron soon. We do not know what we will see at the LHC. Clearly the underlying event will be one of the first measurements and we may have to re-tune the QCD Monte Carlo models at that time. Early analyses in LHC would be geared toward tuning the QCD Monte Carlo models. The number of Z-boson events would be order of magnitude larger, resulting in better analysis of Z-boson Drell-Yan events.

The underlying event measurement plan at the LHC benefits from the solid experience of the CDF studies. The predictions on the amount of activity in transverse region at the LHC are based on extrapolations from lower energy data (mostly from the Tevatron). All the underlying event models have to be tested and adjusted at the LHC, in particular we know very little about the energy dependents of MPI in going from the Tevatron to the LHC. A step by step expectation of progress can be as follows,

1. The first pb^{-1} of collected data will be mainly intended to calibrate the different analysis tools, however, even with such a low integrated luminosity, it will be possible to perform the first evaluation of the underlying event activity in jet events.

2. With 10 pb^{-1} and a partially calibrated detector, it will be possible to take under control the systematics on the underlying event observables, keeping them at the level of the statistical errors and achieving a clear discrimination power between the considered underlying event models.

3. Extending the statistics to 100 pb^{-1}, adopting the ratio observables, *i.e.* an original methodology which exploit the homogeneous performances of the track reconstruction for $p_T > 1.5$ GeV/c and $p_T > 0.9$ GeV/c, it will be possible to distinguish between more subtle differences of the investigated models.

The plan will involve two phases. Phase 1 will be to measure min-bias and the underlying event as soon as possible (when the luminosity is low), perhaps during commissioning and then tune the QCD Monte-Carlo models for all the other analyses. As the measurements become more reliable the QCD Monte-Carlo models can be retuned

if necessary. Phase 2 is 'physics' and would include comparing the min-bias and underlying event measurements at the LHC with the measurements we have done at CDF.

Extrapolating CDF underlying event data to LHC energies [76], we can see that the underlying event is much more active at the LHC. As shown in Figure. 8.1, PYTHIA tune DWT predict about a factor of two increase in charged particle density in going from the Tevatron to the LHC in the toward region. For HERWIG (without MPI) the toward region of Z-boson production does not change much in going from the Tevatron to the LHC.

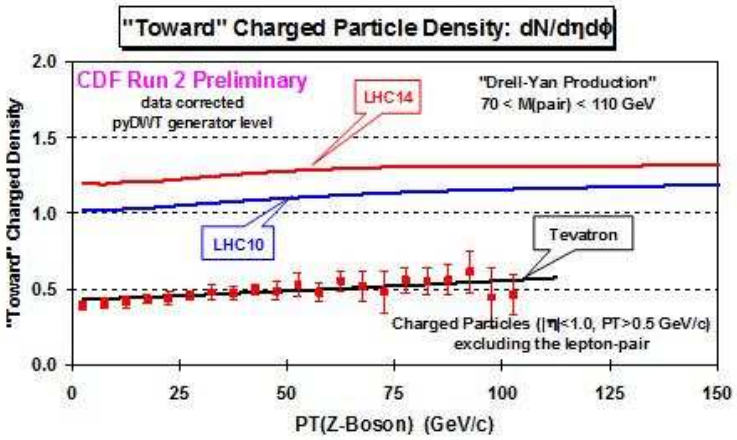

Figure 8-1. Extrapolating charged particle density to LHC energies, 10 TeV and 14 TeV and they are compared with Tevatron data.

However, comparing the underlying event predictions for the LHC generated by models, tuned to the available data, dramatic disagreements in their predictions at LHC energies has been observed [75]. That tells us that improved models for the soft component of hadronic collisions are needed. Future studies should focus on tuning the energy dependence for the event activity in both minimum bias and the underlying event, which at the moment seems to be one of the least understood aspects of all the models.

Going beyond the underlying event studies, an important first step in LHC would be to 'rediscover' the standard model, Drell-Yan process is one of the cleanest signature for that. The procedure followed uses a part of the Drell-Yan mass spectrum where no evidence of new physics is expected to be observed as a control region. This is used

to determine a differential cross section and show it is consistent with the theoretical standard model prediction. Having thus demonstrated that the detector performance and reconstruction procedures are well understood, a search can be made for deviations from the standard model predictions in the new physics search region.

8.3 Final Words

We are making good progress in understanding and modeling the underlying event in jet production and in Drell-Yan. CDF tune A and tune AW describe the data very well, although not perfect. We do not yet have a perfect fit to all the features of the CDF underlying event data. One will learn a lot about the energy dependence of the underlying event (*i.e.* multiple parton interactions) by comparing the Tevatron results with the LHC. It is critical to have sensible underlying event models containing our best physical knowledge and intuition, tuned to all relevant available data.

APPENDIX A
ALL THE NUMBERS

All the PYTHIA tune AW results and corrected data with uncertainities, are shown in Tables 1-12. The uncertainties combine the systematic and statistical errors, as described in Section 7.3. The leftmost column represents the mean value of the lepton pair p_T bin in Tables 1-10, where we plotted observables sensitive to the underlying event as a function of the lepton pair transverse momentum. In Tables 11-12 it shows the mean value of the number of charged particles bin, for the correlation plots. For charged particle multiplicity density and charged transverse momentum sum density, the transDIF region values can be arrived at subtracting the transMIN number from the transMAX number, and adding the errors in quadrature. These numbers would be useful for tuning QCD Monte Carlo models.

Table A-1. Charged multiplicity density, PYTHIA tune AW (against lepton-pair p_T)

Bin	Transverse	Toward	Away
GeV/c			
2.5	0.441190	0.418331	0.479415
7.5	0.470772	0.419169	0.638781
12.5	0.500077	0.421604	0.850426
17.5	0.523195	0.425564	1.025657
22.5	0.533850	0.430954	1.175714
27.5	0.549803	0.432943	1.308171
32.5	0.557136	0.452685	1.431647
37.5	0.553822	0.453690	1.534813
42.5	0.587647	0.457477	1.630054
47.5	0.578597	0.475882	1.753414
52.5	0.576789	0.473830	1.801447
57.5	0.582709	0.482203	1.916967
62.5	0.594417	0.492864	2.012411
67.5	0.607022	0.495092	2.071695
72.5	0.615075	0.507306	2.146753
77.5	0.617776	0.512032	2.250419
82.5	0.597395	0.513534	2.257926
87.5	0.615164	0.548623	2.357177
92.5	0.600291	0.559118	2.438531
97.5	0.634956	0.526936	2.497159

Table A-2. Charged multiplicity density data (against lepton-pair p_T)

Bin	Transverse		Toward		Away	
	Value	Error	Value	Error	Value	Error
GeV/c						
2.5	0.429884	0.038157	0.394497	0.036894	0.486882	0.033712
7.5	0.464533	0.037487	0.410879	0.040925	0.664962	0.030201
12.5	0.496781	0.035923	0.418955	0.041376	0.851113	0.027811
17.5	0.516205	0.041102	0.437691	0.038758	1.022872	0.027655
22.5	0.544145	0.039504	0.443163	0.042726	1.167422	0.033574
27.5	0.578553	0.040471	0.461998	0.038099	1.310917	0.032239
32.5	0.576329	0.039492	0.477200	0.049888	1.427107	0.042026
37.5	0.582738	0.046551	0.474845	0.040970	1.537229	0.048104
42.5	0.611854	0.044120	0.503003	0.039115	1.598780	0.054693
47.5	0.595556	0.053481	0.488912	0.063972	1.739524	0.065100
52.5	0.657754	0.066325	0.531948	0.077630	1.781017	0.074037
57.5	0.618262	0.058964	0.497831	0.054962	1.877647	0.087225
62.5	0.696817	0.071029	0.563499	0.070858	2.022402	0.097893
67.5	0.684587	0.110465	0.519012	0.096435	2.059067	0.112770
72.5	0.625926	0.091369	0.460939	0.126092	2.121736	0.131604
77.5	0.724213	0.082703	0.539187	0.087076	2.313125	0.153275
82.5	0.731066	0.168224	0.589533	0.099774	2.346208	0.188234
87.5	0.627164	0.098195	0.572404	0.087589	2.223688	0.198621
92.5	0.632667	0.108149	0.622034	0.116974	2.391968	0.231219
97.5	0.714989	0.121684	0.470167	0.160005	2.674708	0.259181

Table A-3. Charged p_T sum density, PYTHIA tune AW (against lepton-pair p_T)

Bin	Transverse	Toward	Away
GeV/c	GeV/c	GeV/c	GeV/c
2.5	0.458245	0.435136	0.502786
7.5	0.495159	0.437808	0.716589
12.5	0.542187	0.443978	1.099718
17.5	0.581743	0.453351	1.523039
22.5	0.606412	0.463395	1.962397
27.5	0.647387	0.470380	2.416142
32.5	0.654183	0.502914	2.898896
37.5	0.667357	0.507156	3.418044
42.5	0.728854	0.518889	3.893382
47.5	0.727751	0.555202	4.539055
52.5	0.731746	0.569164	4.977417
57.5	0.753441	0.572198	5.531202
62.5	0.758833	0.600996	6.144451
67.5	0.783532	0.601835	6.754558
72.5	0.824861	0.621673	7.245184
77.5	0.812477	0.644294	8.033557
82.5	0.802204	0.637957	8.430855
87.5	0.827394	0.710648	9.125223
92.5	0.874152	0.733983	9.518611
97.5	0.937036	0.681010	10.551207

Table A-4. Charged p_T sum density data (against lepton-pair p_T)

Bin	Transverse		Toward		Away	
	Value	Error	Value	Error	Value	Error
GeV/c	GeV/c	GeV/c	GeV/c	GeV/c	GeV/c	GeV/c
2.5	0.435353	0.033201	0.393518	0.034510	0.498280	0.032182
7.5	0.476574	0.035259	0.420491	0.037838	0.748463	0.026186
12.5	0.539774	0.032616	0.441382	0.037244	1.106640	0.026554
17.5	0.585860	0.035985	0.466674	0.042250	1.511777	0.029158
22.5	0.635768	0.040039	0.488703	0.046940	1.953986	0.044708
27.5	0.726045	0.044749	0.521995	0.034412	2.410755	0.061629
32.5	0.728270	0.058797	0.558309	0.051983	2.806844	0.086266
37.5	0.758152	0.075726	0.556142	0.069268	3.435244	0.116663
42.5	0.816635	0.081684	0.624332	0.062531	3.736872	0.145178
47.5	0.826132	0.105806	0.579718	0.076768	4.354338	0.184326
52.5	0.918274	0.143548	0.661404	0.128346	4.852975	0.247982
57.5	0.912018	0.141009	0.598869	0.074299	5.204942	0.278039
62.5	1.003324	0.134020	0.757249	0.141355	6.124513	0.365690
67.5	1.109576	0.186670	0.625478	0.128585	6.721900	0.453112
72.5	1.118531	0.318298	0.649719	0.178431	7.137591	0.576299
77.5	1.184121	0.223088	0.734957	0.177753	7.803639	0.604408
82.5	1.355219	0.486744	0.738952	0.185608	8.326511	0.768287
87.5	1.005107	0.340244	0.791880	0.210908	8.683425	0.831823
92.5	0.899535	0.201231	0.895497	0.234016	8.792476	0.948472
97.5	1.228571	0.360561	0.728358	0.356800	10.454969	1.098841

Table A-5. TransMAX and transMIN charged multiplicity density and charged p_T sum density, PYTHIA tune AW (against lepton-pair p_T)

Bin	TransMAX N_{Chg}	TrasMIN N_{Chg}	TrasMAX $p_T$sum	TrasMIN $p_T$sum
GeV/c			GeV/c	GeV/c
2.5	0.681689	0.200692	0.726900	0.189590
7.5	0.723537	0.218008	0.783542	0.206776
12.5	0.766365	0.233788	0.858775	0.225599
17.5	0.802573	0.243817	0.924256	0.239229
22.5	0.822073	0.245627	0.970102	0.242723
27.5	0.845068	0.254538	1.041085	0.253689
32.5	0.858854	0.255417	1.052669	0.255696
37.5	0.854451	0.253194	1.082424	0.252290
42.5	0.912864	0.262431	1.191250	0.266458
47.5	0.897962	0.259232	1.191606	0.263895
52.5	0.903548	0.250030	1.211993	0.251500
57.5	0.912159	0.253260	1.244784	0.262098
62.5	0.930124	0.258710	1.255885	0.261780
67.5	0.955370	0.258673	1.307165	0.259899
72.5	0.958890	0.271261	1.370470	0.279251
77.5	0.974342	0.261209	1.338983	0.285970
82.5	0.935092	0.259698	1.315115	0.289294
87.5	0.977201	0.253127	1.410893	0.243895
92.5	0.948702	0.251880	1.443948	0.304356
97.5	1.002132	0.267780	1.545278	0.328794

Table A-6. TransMAX and transMIN charged multiplicity density and charged p_T sum density, data (against lepton-pair p_T)

Bin	TransMAX N_{Chg}		TransMIN N_{Chg}		TransMAX $p_T$sum		TransMIN $p_T$sum	
	Value	Error	Value	Error	Value	Error	Value	Error
GeV/c					GeV/c	GeV/c	GeV/c	GeV/c
2.5	0.652947	0.032777	0.207180	0.054345	0.682521	0.029262	0.186298	0.039296
7.5	0.704123	0.030430	0.225341	0.059979	0.747338	0.029862	0.206169	0.057880
12.5	0.747106	0.032524	0.247104	0.047265	0.844706	0.031363	0.235472	0.046417
17.5	0.784411	0.037544	0.248306	0.055896	0.931457	0.040469	0.240272	0.048383
22.5	0.829307	0.036130	0.259271	0.057549	1.012554	0.045016	0.259210	0.050868
27.5	0.887771	0.036803	0.269432	0.067802	1.174713	0.059538	0.277196	0.059470
32.5	0.878680	0.042377	0.274294	0.048100	1.165724	0.081922	0.291482	0.038390
37.5	0.882859	0.051289	0.283282	0.051002	1.210065	0.100767	0.307016	0.069879
42.5	0.941064	0.049560	0.282977	0.073549	1.324690	0.117749	0.309257	0.112795
47.5	0.921546	0.060993	0.269981	0.075409	1.370427	0.160439	0.281340	0.090005
52.5	1.015435	0.086519	0.299994	0.043912	1.535381	0.206598	0.301115	0.093833
57.5	0.963857	0.076236	0.272753	0.074410	1.518061	0.204742	0.305107	0.185526
62.5	1.062772	0.090163	0.332060	0.086639	1.660973	0.227768	0.346003	0.095723
67.5	1.040877	0.127219	0.330606	0.113895	1.867771	0.324943	0.351494	0.156356
72.5	0.969563	0.111253	0.282414	0.117114	1.875308	0.505442	0.364041	0.159212
77.5	1.151519	0.129996	0.296909	0.081715	2.005456	0.391962	0.355573	0.101484
82.5	1.101488	0.199906	0.364792	0.175006	2.132673	0.691309	0.604039	0.377265
87.5	0.998426	0.146082	0.256701	0.116415	1.784530	0.604915	0.233006	0.142828
92.5	0.982737	0.159731	0.284172	0.087757	1.427561	0.307590	0.388592	0.158239
97.5	1.079437	0.168153	0.354878	0.107867	1.946477	0.570819	0.526910	0.313929

Table A-7. Charged p_T average, PYTHIA tune AW (against lepton-pair p_T)

Bin	Transverse	Toward	Away
GeV/c	GeV/c	GeV/c	GeV/c
2.5	0.977961	0.983135	0.998049
7.5	0.988433	0.986118	1.076857
12.5	1.009190	0.992081	1.250226
17.5	1.027735	0.996923	1.434610
22.5	1.044285	1.005538	1.605390
27.5	1.067319	1.006092	1.776252
32.5	1.065266	1.020673	1.947544
37.5	1.083514	1.026808	2.144531
42.5	1.092631	1.038639	2.314193
47.5	1.118515	1.040122	2.538778
52.5	1.100632	1.051193	2.695855
57.5	1.126394	1.054374	2.830105
62.5	1.116889	1.066706	3.017819
67.5	1.122719	1.064898	3.253468
72.5	1.147589	1.064943	3.413978
77.5	1.115415	1.082497	3.583574
82.5	1.153103	1.087685	3.776584
87.5	1.159050	1.108540	3.818242
92.5	1.162041	1.123290	3.966906
97.5	1.187338	1.086748	4.365540

Table A-8. Charged p_T average data (against lepton-pair p_T)

Bin	Transverse		Toward		Away	
	Value	Error	Value	Error	Value	Error
GeV/c	GeV/c	GeV/c	GeV/c	GeV/c	GeV/c	GeV/c
2.5	0.968115	0.011853	0.962479	0.009494	0.984619	0.008372
7.5	0.980862	0.007551	0.983285	0.012364	1.097828	0.010841
12.5	1.027762	0.015244	1.003831	0.015091	1.270614	0.016865
17.5	1.057594	0.029479	1.017353	0.023568	1.437161	0.020945
22.5	1.083772	0.020892	1.025372	0.023243	1.606906	0.027743
27.5	1.119088	0.030729	1.050930	0.026503	1.771939	0.036892
32.5	1.127434	0.038913	1.061525	0.042759	1.873190	0.049100
37.5	1.148774	0.042751	1.052937	0.042902	2.166247	0.075460
42.5	1.141964	0.047243	1.119506	0.061264	2.276723	0.088834
47.5	1.172658	0.054550	1.065805	0.079399	2.538655	0.150962
52.5	1.202899	0.066749	1.049046	0.059243	2.627952	0.137523
57.5	1.239558	0.085639	1.033265	0.055307	2.657019	0.141937
62.5	1.230943	0.097713	1.180433	0.136818	2.997993	0.207739
67.5	1.354040	0.133989	1.029608	0.074460	3.326541	0.303504
72.5	1.438946	0.207718	1.163404	0.135485	3.279669	0.285294
77.5	1.352431	0.175030	1.250588	0.180895	3.299840	0.259023
82.5	1.360674	0.188000	1.099546	0.114660	3.489132	0.371706
87.5	1.270004	0.169970	1.237109	0.245494	4.007693	0.498593
92.5	1.229490	0.154037	1.226441	0.171063	3.625865	0.380772
97.5	1.302693	0.183910	1.230726	0.234870	4.001531	0.436877

Table A-9. Charged p_T maximum, PYTHIA tune AW (against lepton-pair p_T)

Bin	Transverse	Toward	Away
GeV/c	GeV/c	GeV/c	GeV/c
2.5	1.297300	1.304026	1.347412
7.5	1.334228	1.312690	1.577113
12.5	1.399653	1.329666	2.100229
17.5	1.452787	1.346580	2.727001
22.5	1.501545	1.364594	3.381393
27.5	1.574993	1.380164	4.062150
32.5	1.568925	1.415379	4.764334
37.5	1.623508	1.437615	5.527891
42.5	1.679240	1.463455	6.278535
47.5	1.722461	1.512675	7.235626
52.5	1.713105	1.560187	7.929144
57.5	1.755433	1.534377	8.541471
62.5	1.724520	1.565038	9.548020
67.5	1.801966	1.582820	10.363932
72.5	1.854602	1.591514	11.350276
77.5	1.780472	1.629370	12.294122
82.5	1.858147	1.611543	13.099581
87.5	1.860280	1.741029	13.482826
92.5	1.891444	1.794630	14.158522
97.5	1.995710	1.674676	16.340929

Table A-10. Charged p_T maximum data (against lepton-pair p_T)

Bin	Transverse		Toward		Away	
	Value	Error	Value	Error	Value	Error
GeV/c	GeV/c	GeV/c	GeV/c	GeV/c	GeV/c	GeV/c
2.5	1.289336	0.016893	1.264720	0.016567	1.339714	0.016762
7.5	1.325593	0.015486	1.321100	0.022684	1.635515	0.019100
12.5	1.445278	0.024467	1.367889	0.026650	2.133847	0.032854
17.5	1.538308	0.058603	1.390166	0.041797	2.712774	0.044442
22.5	1.593405	0.043954	1.458595	0.058912	3.394932	0.080564
27.5	1.737490	0.071508	1.480948	0.052377	4.041536	0.118175
32.5	1.761159	0.097422	1.534991	0.106695	4.602731	0.168460
37.5	1.850037	0.141158	1.556321	0.109647	5.717539	0.235655
42.5	1.911452	0.161787	1.723451	0.132304	6.061238	0.268451
47.5	1.969359	0.199656	1.642915	0.165170	6.956539	0.373587
52.5	2.013126	0.187737	1.652740	0.235660	7.820367	0.480361
57.5	2.155480	0.299941	1.543367	0.142685	8.016521	0.523943
62.5	2.141188	0.260937	1.888659	0.307539	9.412107	0.801335
67.5	2.513503	0.381959	1.538327	0.199495	10.582969	1.059326
72.5	2.942115	0.933515	1.878273	0.470510	11.189622	1.215337
77.5	2.443905	0.470712	1.954935	0.378772	11.800685	1.040150
82.5	2.728654	0.797302	1.743511	0.344723	12.394446	1.518707
87.5	2.450618	0.914335	2.156266	0.653224	13.812913	1.818187
92.5	1.940730	0.317366	2.123585	0.552999	13.709188	1.735494
97.5	2.587987	0.716815	2.528047	1.613327	15.66572	2.132479

Table A-11. Correlation, PYTHIA tune AW (against charged multiplicity)

Bin	Charged p_T average	Z-boson p_T	Charged p_T average(Z-p_T < 10 GeV/c) (Z-boson p_T < 10GeV/c)
	GeV/c	GeV/c	GeV/c
0.5	0.000000	7.281554	0.000000
1.5	0.880256	7.745971	0.851537
2.5	0.949484	8.335976	0.900177
3.5	1.015241	8.892390	0.938501
4.5	1.075084	9.634406	0.972826
5.5	1.121440	10.355534	0.994868
6.5	1.167467	10.967258	1.017383
7.5	1.200338	11.797971	1.038834
8.5	1.236853	12.632196	1.053885
9.5	1.261768	13.264112	1.066997
10.5	1.295990	14.211138	1.085186
11.5	1.310715	14.961679	1.096542
12.5	1.334410	15.843349	1.108661
13.5	1.367908	16.984150	1.118061
14.5	1.389122	17.852399	1.130039
15.5	1.408269	19.134403	1.138610
16.5	1.432441	20.140832	1.151225
17.5	1.479279	21.969024	1.160803
18.5	1.496516	23.057088	1.170455
19.5	1.548315	25.605709	1.173441
20.5	1.558440	26.561321	1.188392
21.5	1.606953	29.325691	1.191551
22.5	1.634185	30.990329	1.205351
23.5	1.684246	32.999405	1.228811
24.5	1.747084	35.949880	1.254064
25.5	1.765078	36.428417	1.281778
26.5	1.803864	39.138041	1.268193
27.5	1.913521	45.027361	1.321352
28.5	1.945321	45.240048	1.271546
29.5	1.954607	48.639820	1.246006
30.5	2.028106	50.896419	1.299919

Table A-12. Correlations, data (against charged multiplicity)

Bin	Charged p_T average		Z-boson p_T		Charged p_T average (Z-boson $p_T < 10$ GeV/c)	
	Value	Error	Value	Error	Value	Error
	GeV/c	GeV/c	GeV/c	GeV/c	GeV/c	GeV/c
0.5	0.000000	0.000000	6.880756	0.176590	0.000000	0.000000
1.5	0.962075	0.030396	7.898231	0.181074	0.912443	0.028004
2.5	0.981561	0.017133	8.583409	0.174970	0.926157	0.018359
3.5	1.038758	0.018983	9.090722	0.178010	0.948536	0.022139
4.5	1.091332	0.019794	10.046453	0.197884	0.977673	0.014655
5.5	1.132328	0.017321	10.825870	0.220835	0.988061	0.011003
6.5	1.153059	0.017643	11.551637	0.259128	0.999313	0.009660
7.5	1.199244	0.020209	12.403667	0.283542	1.014718	0.008465
8.5	1.234035	0.015650	13.369972	0.323761	1.024515	0.015190
9.5	1.261723	0.035583	14.022197	0.362126	1.038935	0.021267
10.5	1.282793	0.020606	14.95841	0.410099	1.046248	0.014807
11.5	1.307791	0.024686	16.37650	0.511125	1.049602	0.011556
12.5	1.351104	0.026124	17.151203	0.593185	1.069046	0.020490
13.5	1.365498	0.036576	18.076207	0.716530	1.077276	0.023259
14.5	1.366173	0.043261	18.091477	0.781606	1.086755	0.020806
15.5	1.393500	0.046936	19.823398	0.912590	1.075179	0.028665
16.5	1.423849	0.036398	20.906292	1.154710	1.101314	0.028657
17.5	1.467522	0.063385	22.493239	1.378022	1.114511	0.032657
18.5	1.507749	0.066635	23.58852	1.575298	1.117973	0.043386
19.5	1.521382	0.051084	25.557341	1.837549	1.118198	0.054123
20.5	1.542902	0.073169	26.128896	2.176544	1.137268	0.051519
21.5	1.620292	0.082402	29.209804	2.786069	1.150230	0.051813
22.5	1.606931	0.107066	29.203141	3.245372	1.159754	0.082760
23.5	1.604221	0.097319	30.205654	3.364320	1.185487	0.140351
24.5	1.703297	0.130266	33.189658	4.340128	1.207592	0.098469
25.5	1.643145	0.119900	32.58106	4.981632	1.334000	0.281803
26.5	1.748688	0.177755	35.622813	5.522897	1.220607	0.111617
27.5	1.753060	0.150570	38.369237	6.323233	1.246973	0.074538
28.5	1.855084	0.163995	37.105194	6.687316	1.145064	0.164292
29.5	1.885025	0.232097	40.692293	10.832211	1.171859	0.172040
30.5	2.123252	0.343358	49.169643	9.993295	1.229951	0.139931

REFERENCES

[1] S. L. Glashow, *Partial Symmetries of Weak Interactions,* Nucl. Phys **22**, 579 (1961); S. Weinberg, *A Model of Leptons*, Phys. Rev. Lett. **19**, 1264 (1967); A. Salam, *Elementary Particle Theory*, Ed. N. Svartholm, Almquist and Wiksell, Stockholm, 367 (1968).

[2] R. D. Field, *Applications of Perturbative QCD* (Redwood City: Addison-Wesley, 1989).

[3] P. Langacker, *Structure of the Standard Model*, arXiv:hep-ph/0304186.

[4] P. W. Higgs, *Broken Symmetries and the Masses of Gauge Bosons*, Phys. Rev. Lett. **13**, 508 (1964).

[5] S. P. Martin, *A Supersymmetry Primer*, arXiv: hep-ph/9709356.

[6] B. Zwiebach, *A First Course in String Theory*, (Cambridge: University Press, 2004).

[7] E. Malamud (2001), *Fermilab's Chain of Accelerators*, Fermilab, Batavia, IL, http://www-bd.fnal.gov/public/index.html (last accessed November, 2008). J. Marriner (2003), *Fermilab Beams Division, Run II Handbook*, Fermilab, Batavia, IL, http://www-bd.fnal.gov/runII/index.html (last accessed November, 2008).

[8] G. Aubrecht, *A Teachers Guide to the Nuclear Science Wall Chart, Contemporary Physics Education Project, 2003.*

[9] C. W. Schmidt, *The Fermilab 400-Me V Linac Upgrade*, Fermilab Report No. FERMILAB-CONF-93-111, 1993.

[10] J. Marriner (2003), *Main Injector at Tevatron Technical Report*, Fermilab, Batavia, IL, http://www-bd.fnal.gov/runII/index.html (last accessed November, 2008).

[11] J. Marriner, *Stochastic Cooling Overview*, Fermilab Report No. FERMILAB-CONF-03-158, 2003.

[12] CDF Collaboration, *A Brief Description of Run II Detector*, Fermilab Report No. FERMILAB-PUB-96/390-E, 1996.

[13] CDF Collaboration, *CDF Run II Silicon Tracking Projects*, Nucl. Instrum. Methods A **447**, 1 (2000); A. Affolder, P. Azzi-Bacchetta, N. Bacchetta, G. Barker, A. Barbaro-Galtieri, A. Basti *et al.*, *Intermediate Silicon Layers Detector for the CDF Experiment*, Nucl. Instrum. Methods A **453**, 84 (2000); C.S. Hill, *Operational Experience and Performance of the CDFII Silicon Detector*, Nucl. Instrum. Methods A **530**, 1 (2000).

[14] T. Affolder, D. Allspach, D. Ambrose, J. Bialek, W. Bokhari, M. Brozovic *et al.*, *CDF Central Outer Tracker*, Nucl. Instrum. Methods A **526**, 249 (2004); CDF Run II Collaboration, *et al.*, Fermilab Report No. FERMILAB-CONF-96-443-E, 1996.

[15] CDF Collaboration, *A Time-of-Flight Detector in CDF-II*, Nucl. Instrum. Methods A **518**, 605 (2004).

[16] L. Balka, K. Coover, R. Diebold, W. Evans, N. Hill, L. Nodulman *et al.*, *The CDF Central Electromagnetic Calorimeter*, Nucl. Instrum. Methods A **267**, 272 (1988); S. Bertolucci, M. Cordelli, B. Esposito, M. Curatolo, P. Giromini, S. Miscetti *et al.*, *The CDF Central and Endwall Hadron Calorimeter*, Nucl. Instrum. Methods A **267**, 301 (1988).

[17] Particle Data Group, *Review of Particle Physics*, Physics Letters B **592** 1 (2004).

[18] C. Group, Ph.D. thesis, University of Florida, 2006.

[19] C. M. Ginsburg, *CDF Run 2 Muon System*, The European Physical Journal C **33**, 1002, (2004).

[20] D. Acosta, S. Klimenko, J. Konigsberg, A. Korytov, G. Mitselmakher, A. Nguyel *et al.*, *The CDF Cherenkov Luminosity Monitor*, Nucl. Instrum. Methods A **461**, 540 (2001).

[21] F. Abe, D. Amidei, G. Apollinari, G. Ascoli, M. Atac, P. Auchincloss *et al.*, *The CDF Detector: An Overview*, Nucl. Instrum. Methods Phys. Methods A **271**, 387 (1988).

[22] CDF Collaboration, *The CDF Run II Detector Technical Design Report*, Fermilab Report No. FERMILAB-Pub-96/390-E, 1996.

[23] R. D. Field, *Min-Bias At The Tevatron*, Fermilab Report No. FERMILAB-CONF-07-465-E, 2007.

[24] CDF Collaboration, *Measurement of the antiproton-proton total cross section at* $\sqrt{s} = 546$ *and 1800 GeV*, Phys. Rev. D **50**, 5550 (1994); E-710 Collaboration, Phys. Lett. B **243**, 158 (1990); CDF Collaboration, Nuovo Cim. A **107**, 2085 (1994).

[25] Heidi Schellman (2005), *Practical Aspects of Collider Physics*, Institute of Advanced Studies, Princeton, NJ. http://www.sns.ias.edu/pitp/index2005.html (last accessed November 2008).

[26] The CTEQ Collaboration, *CTEQ Handbook of Perturbative QCD*, Rev. Mod. Phys. **67**, 157, (1995).

[27] S. Ellis, Z. Kunszt and D. Soper, *One Jet Inclusive Cross Section at Order* α_s^3 *Gluons Only*, Phys. Rev. D. **40** 2188 (1989).

[28] R. D. Field, *Physics at the Tevatron*, CDF Public Note No. 8553, 2006.

[29] CDF Collaboration, *The Underlying Event in Large Transverse Momentum Charged Jet and Z-Boson Production*, Fermilab Report No. FERMILAB-CONF-00/289-E

(2000); CDF Collaboration, *Underlying Event in Hard Interactions at the Fermilab Tevatron $\bar{p}p$ Collider*, Phys. Rev. D **70**, 072002 (2004).

[30] CDF Collaboration, *Charged jet evolution and the underlying event in proton-antiproton collisions at 1.8 TeV*, Phys. Rev. D **65**, 092002 (2002); R. D. Field, *The Underlying Event in Large Transverse Momentum Charged Jet and Z-Boson Production*, Int. J. Mod. Phys. A **16S1A**, 250 (2001); J. Huston, *A Comparison of the Underlying Event in Jet and Minimum Bias Events*, Int. J. Mod. Phys. A **16S1A**, 219 (2001).

[31] G. Marchesini and B. R. Weber, *Associated Transverse Energy in Hadronic Jet Production*, Phys. Rev. D **38**, 3419 (1988).

[32] J. Pumplin, *Hard Underlying Event Correction to Inclusive Jet Cross Sections* Phys. Rev. D **57**, 5787 (1998).

[33] J. H. Christenson, G. S. Hicks, L. M. Lederman, P. J. Limon, B .G. Pope and E. Zavatini, *Observation of Massive Muon Pairs in Hadron Collisions*, Phys. Rev. Lett. **25**, 1523 (1970) and *Observation of Muon Pairs in High-Energy Hadron Collisions*, Phys. Rev. D **8**, 2016 (1973).

[34] J. J. Aubert, U. Becker, P. J. Biggs, J. Burger, M. Chen, G. Everhart *et al.*, *Experimental Observation of a Heavy Particle J*, Phys. Rev. Lett. **33**, 1404 (1974);

[35] S. D. Drell and T. M. Yan, *Massive Lepton-Pair Production in Hadron-Hadron Collisions at High Energies*, Phys. Rev. Lett. **25**, 316 (1970) and Ann. Phys. (N.Y.), **66**, 578 (1971).

[36] J. D. Bjorken and E. A. Paschos, *Inelastic Electron-Proton and γ-Proton Scattering, and the Structure of the Nucleon*, Phys. Rev. **185**, 1975 (1969); R. P. Feynman, *Very High-Energy Collisions of Hadrons*, Phys. Rev. Lett. **23**, 1415 (1969).

[37] T. M. Yan, *Naive Drell-Yan and Its Successor*, Talk given at the Drell Fest, SLAC (1998), arXiv:hep-ph/9810268; I. R. Kenyon, Rep. Prog. Phys., **45**, 1261 (1982).

[38] B. Potter (1997), *Calculational Techniques in Perturbative QCD: The Drell-Yan Process*, DESY, Hamburg, Germany. http://www.desy.de/∼poetter/ps/drell-yan.ps (last accessed November 2008).

[39] R. K. Ellis, W. J. Sterling and B. R. Webber, *QCD and Collider Physics* (Cambridge: University Press, 1996).

[40] E. L. Berger, J. Qiu, X. Zhang, *QCD Factorized Drell-Yan Cross Section at Large Transverse Momentum*, Phys. Rev. D **65**, 034006 (2002).

[41] R. K. Ellis, W. J. Sterling and B. R. Webber (2001), *QCD Figures Available Online*, (Cambridge: University Press), http://theory.fnal.gov/people/ellis/BookFigs/Figs.html (last accessed June, 2008)

[42] CDF Collaboration, *Measurement of the W Boson Mass*, Phys. Rev. Lett. **75**, 11 (1995).

[43] CDF Collaboration, *First Measurements of Inclusive W and Z Cross Sections from Run II of the Fermilab Tevatron Collider*, Phys. Rev. Lett. **94**, 091803 (2005).

[44] U. K. Yang and A. Bodek, *Studies of Higher Twist and Higher Order Effects in NLO and NNLO QCD Analysis of Lepton-Nucleon Scattering Data on F_2 and $R = \sigma_L/\sigma_T$*, Euro. Phys. Jour. C **13**, 241 (2000); W. L. van Neerven and A. Vogt, *NNLO evolution of deep-inelastic structure functions: the non-singlet case*, Nucl. Phys. B **568**, 263 (2000); A. D. Martin, R. G. Roberts, W. J. Stirling and R. S. Thorne, *Estimating the Effect of NNLO Contributions on Global Parton Analyses*, arXiv:hep-ph/0007099.

[45] J. L. Rosner, *Forward-Backward Asymmetries in Hadronically Produced Lepton Pairs*, Phys. Rev. D **54**, 1078 (1996).

[46] K. O. Mikaelian and R. J. Oakes, *Neutral-current effects in Bethe-Heitler pair production*, Phys. Rev. D **16**, 3216 (1977).

[47] F. James, *Monte Carlo theory and practice*. Rep. Prog. Phys. **43**, 3 (1980).

[48] R. Brun, F. Bruyant, M. Maire, A. C. McPherson and P. Zanarini, *GEANT 3, User Guide*, CERN Report No. DD-EE-84-1 (1989).

[49] T. Sjostrand, P. Eden, C. Friberg, L. Lonnblad, G. Miu, S. Mrenna and E. Norrbin, *High-Energy-Physics Event Generation with PYTHIA 6.1* Computer Physics Commun. **135**, 238 (2001). We use PYTHIA version 6.216.

[50] G. Corcella, I. G. Knowles, G. Marchesini, S. Moretti, K. Odagiri, P. Richardson *et al.*, *HERWIG 6: An Event Generator for Hadron Emission Reactions with Interfering Gluons*, JHEP **01**, 10 (2001).

[51] B. Andersson, G. Gustafson and B. Soderberg, *A General Model For Jet Fragmentation* Z. Phys. C **20**, 317 (1983); B. Andersson, *The Lund Model* (Cambridge: University Press, 1998).

[52] G. Marchesini, B. R. Webber, G. Abbiendi, I. G. Knowles, M. H. Seymour and L. Stanco, *HERWIG 5.6 Monte Carlo Program*, Comp. Phys. Commun. **67**, 465 (1992).

[53] T. Sjostrand, L. Lonnblad, S. Mrenna and P. Skands, *PYTHIA 6.3 Physics and Manual*, arXiv: hep-ph/0308153.

[54] R. D. Field and R. C Group, *PYTHIA tune A, HERWIG, and JIMMY in Run 2 at CDF*, arXiv: hep-ph/0510198.

[55] CDF Collaboration, *Measurement of the Z p_T Distribution in Proton-Antiproton Collisions at 1.8 TeV* Phys. Rev. Lett. **67**, 2937 (1991).

[56] R. D. Field, Pub. Proc. TeV4LHC Workshop, Fermilab, Batavia IL, USA (2005).

[57] Andrey Korytov, *Soft QCD phenomena in events with high-E_T jets at tevatron*, Eur. Phys. J. C **33**, s425 (2004).

[58] T. Sjostrand, *A Model for Initial State Parton Showers*, Phys. Lett. **157B**, 321 (1985); M. Bengtsson, T. Sjostrand and M. Van Zijl, *Initial State Radiation Effects on W and Jet Production*, Z. Phys. C **32**, 67 (1986); T. Sjostrand and M. Van Zijl, *A multiple-interaction model for the event structure in hadron collisions*, Phys. Rev. D **36**, 2019 (1987).

[59] DØ Collaboration, *Measurement of Dijet Azimuthal Decorrelations at Central Rapidities in $p\overline{p}$ Collisions at $\sqrt{s} = 1.96$ TeV*, Phys. Rev. Lett. **94**, 221801 (2005).

[60] H. L. Lai, J. Huston, S. Kuhlmann, J. Morfin, F. Olness, J F. Owens, J. Pumplin and W K. Tung, *Global QCD Analysis of Parton Structure of the Nucleon: CTEQ5 Parton Distributions*, Eur. Phys. J. C **12**, 375 (2000).

[61] R. D. Field, *Studying the Underlying Event at CDF*, Proceedings of the XXXIII International Conference on High Energy Physics, Moscow (2006), Edited by A. N. Sissakian and G. A. Kozlov (World Scientific, Singapore, 2007) pp 581-585.

[62] D. Acosta, F. Ambroglini, P. Bartalini, A. De Roeck, L. Fano, R. D. Field and K. Kotov, *The Underlying Event at the LHC*, CMS Note No. 2006-067, 2006.

[63] CDF Run II Collaboration, *Measurements of Inclusive W and Z Cross Sections in p anti-p Collisions at s**(1/2) = 1.96 TeV*, J. Phys. G: Nucl. Part. Phys. 2457 (2007).

[64] T. Spreitzer, C. Mills and J. Incandela, *Electron Identification in Offline Release 6.1.2*, CDF Internal Note 7950, 2006 (unpublished).

[65] U. Grundler, A. Taffard and X. Zhang, *High-P_T muons recommended cuts and efficiencies for Summer 2006*, CDF Internal Note No. 8262, 2006 (unpublished).

[66] CDF Run II Collaboration, *Measurement of the Cross Section for tt Production in p anti-p Collisions Using the Kinematics of Lepton Jets Events*, Phys. Rev. D **72**, 052003 (2005).

[67] T. Pratt, K. Ikado, K. Maeshima and T. Huffman, *Resonance Searches in high mass dimuons*, CDF Internal Note No. 6073, 2003 (unpublished).

[68] CDF Run II Collaboration, *Measurement of Inclusive Jet Cross Sections in Z/gamma*($\rightarrow e^+e^-$)+jets Production in p anti-p Collisions at s**(1/2) = 1.96 TeV*, Phys. Rev. Lett. **100**, 102001 (2008).

[69] G . C. Blazey, J. R. Dittmann, S. D. Ellis, V. D. Elvira, K. Frame, S. Grinstein *et al.*, *QCD and Weak Boson Physics in Run II*, arXiv:hep-ex/0005012.

[70] A. Cruz and R. D. Field, *Using Correlations in the Transverse Region to Study the Underlying Event in Run 2 at the Tevatron*, CDF Public Note No. 6821, 2003.

[71] J. M. Butterworth, J. R. Forshaw and M. H. Seymour, *Multiparton Interactions in Photoproduction at HERA*, Z. Phys. C **72**, 637 (1996).

[72] UA1 Collaboration, *Transverse Momentum Spectra for Charged Particles at the CERN Proton anti-Proton Collider*, Phys. Lett. **118B**, 167 (1982).

[73] CDF Collaboration, *Soft and Hard Interactions in p anti-p Collisions at* $\sqrt{s}$ *=1800 and 630 GeV*, Phys. Rev. D **65**, 072005 (2002).

[74] X. Wang and C. Hwa, *Effect of jet production on the multiplicity dependence of average transverse momentum*, Phys. Rev. D **39**, 187 (1989); F. W. Bopp, P. Aurenche and J. Ranft, *Transverse Momenta in Minimum-Bias Events at Collider Energies*, Phys. Rev. D **33**, 1867 (1986).

[75] P. Skands and D. Wicke, *Non-perturbative QCD effects and the top mass at the Tevatron*, Eur. Phys. J. C **52** 133, (2007).

[76] R. D. Field, *Studying the Underlying Event at CDF*, Fermilab Report No. FERMILAB-CONF-06-409-E, 2005.

[77] N. Moggi, M. Mussini, F. Rimondi, *Measurement of Inelastic pp Inclusive Cross Sections*, CDF Public Note No. 9337, 2008.

BIOGRAPHICAL SKETCH

Deepak Kar was born in Silverspring, MD in 1979. He returned to India with his parents, Nikhilesh and Ramala Kar soon after that, growing up along with his younger sister Nandini in the quiet little town of Siliguri, on the foothills of the Himalayas. After completing high school there, he moved to Calcutta (now known as Kolkata), one of the major Indian metropolises to finish both his three-year B.Sc (in 2001) and two-year M.Sc (in 2003), from Jadavpur University, majoring in Physics. His interest in this branch of science partly grew from his father, a professor of Physics himself and further developed under the excellent teachers at Jadavpur. Beside completing his coursework, Deepak worked at Harishchandra Research Institute (HRI), Allahabad, in 2001, at Saha Institute of Nuclear Physics (SINP), Kolkata, in 2002 and at the Indian Association for the Cultivation of Sciences (IACS) in 2003, as a summer research project student. He was one of the recipients of the highly competitive Summer Research Fellowship of Indian Academy of Sciences in 2001, and in the same year was also awarded a Gold Medal for being placed in the national top five in the National Graduate Physics Examination organized by Indian Association of Physics Teachers.

Deepak joined the University of Florida, Gainesville for his graduate study in the fall of 2003 leading to a doctoral degree. Apart from his research work, he worked as a teaching assistant, where his responsibilities included teaching lab classes in mechanics and electricity-magnetism at the beginning undergraduate level with full responsibility over grades. He was a participant in Prospects in Theoretical Physics Summer School 'The Standard Model and Beyond' held in July 2007 at the Institute of Advanced Studies, Princeton and the second and third CERN-FNAL Hadron Collider Physics Summer School held respectively at Geneva, Switzerland and at Fermilab during the summer of 2007 and 2008. His research was focused on better modeling of the so called underlying events at hadron colliders, which is an unavoidable background to all the collider observables. He presented his research at American Physical Society's (APS) annual meeting at St. Louis,

MO; and at the Phenomenology Symposium at Madison, WI. He was an invited speaker at the International Symposium on Multiparticle Dynamics held in DESY, Hamburg, Germany in September 2008. The highlight of his career at Florida was when he received the prestigious Charles F. Hooper Jr. Memorial Award from the Department of Physics for distinction in research and teaching in December 2007.

Deepak graduated from the University of Florida with a doctorate in the fall of 2008 and is looking forward to join Technische Universität Dresden in Germany as a postdoctoral research fellow in the spring of 2009, working on ATLAS experiment.